

UNIVERSITY OF MILANO – BICOCCA
DEPARTMENT OF MATERIAL SCIENCES



Ph.D. School in Chemical Sciences

Cycle XXVII

Dissertation held on the 19th of March 2015

CZTS(e) thin films grown by chemical methods for PV application

Ph.D. Thesis by

Sara TOMBOLATO

Supervised by Prof. Simona BINETTI

Die Chemie ist der unheimliche Teil der Physik

Table of Contents

| | |
|---|------------|
| Abstract | iii |
| Acknowledgements | v |
| List of abbreviations | vii |
| Chapter 1 Introduction | 1 |
| 1.1 Thin film chalcogenides as absorbers in photovoltaic devices | 1 |
| 1.2 CZTS and CZTSe..... | 6 |
| 1.2.1 Pseudo-ternary phase diagram..... | 7 |
| 1.2.2 Detrimental phases | 10 |
| 1.2.3 $\text{Cu}_2\text{ZnSn}(\text{S}_x\text{Se}_{1-x})_4$ fabrication methods and state of the art of $\text{Cu}_2\text{ZnSn}(\text{S}_x\text{Se}_{1-x})_4$ -based solar cells | 11 |
| Chapter 2 Fabrication and characterization techniques | 19 |
| 2.1 Deposition of precursors | 19 |
| 2.2 Annealings..... | 23 |
| 2.3 Building the device..... | 26 |
| 2.4 Characterization of precursor and absorber layers | 27 |
| 2.5 Electrical measurements..... | 28 |
| Chapter 3 CZTS thin film fabrication | 31 |
| 3.1 Monoethanolamine containing sol-gel | 31 |

| | | |
|---|--|------------|
| 3. 1. 1 | Formulation and deposition of the sol-gel | 31 |
| 3. 1. 2 | Characterization of absorber layers and solar cells..... | 33 |
| 3. 2 | Thiourea containing suspension..... | 43 |
| 3. 2. 1 | Formulation and deposition of the liquid suspension | 43 |
| 3. 2. 2 | Identification of the crystallization temperature | 44 |
| 3. 2. 3 | Crack formation issue and optimization of the method | 47 |
| 3. 2. 4 | Characterization of precursor and absorber layer | 52 |
| 3. 2. 5 | Effect of stoichiometric concentration of thiourea in the suspension..... | 55 |
| 3. 2. 6 | Effects of polyvinyl alcohol on films grown via thiourea complexes plus sulfurization. A preliminary study. | 57 |
| Chapter 4 | CZTSe thin film fabrication: concentrated ink containing formate ions | 61 |
| 4. 1 | Formulation and deposition of the ink..... | 62 |
| 4. 2 | Characterization of the precursor layer..... | 64 |
| 4. 3 | Characterization of sodium free absorber layers and solar cells..... | 67 |
| 4. 4 | Absorber layers grown by RTP | 74 |
| 4. 5 | Characterization of sodium doped absorber layers and solar cells | 77 |
| Chapter 5 | Conclusions and recommendations for further studies . | 87 |
| Bibliography | | 91 |
| Publications & presentations | | 103 |

Abstract

CZTS(e), often referred to as kesterites, are a class of semiconductors with a direct band gap ranging between 1.0 and 1.5 eV and an absorption coefficient in the order of 10^4 cm^{-1} in the visible spectrum, and during the last two decades they have been gaining a lot of attention because of their potential use as a thin film absorbers in photovoltaics.

Another thin film chalcogenide, CIGS, with composition $\text{Cu}_2\text{In}_x\text{Ga}_{(1-x)}\text{Se}_2$ has already reached the commercial production stage, but the constant increase of indium price has driven hunt to alternative materials, like $\text{Cu}_2\text{ZnSn}(\text{S},\text{Se})_4$, which are composed only of abundant (thus relatively cheap) elements. In order to meet the terawatt-scale power generation with photovoltaics, not only the abundancy of the raw materials is a key factor, but also the method chosen for growing these materials need to be carefully considered.

The vacuum-based processes including co-evaporation and sputtering have been largely used for preparing absorber layers on a laboratory scale. However, these methods have drawbacks such as the complexity in process and high production costs. Non-vacuum chemical processes are characterized by simpler fabrication steps compared to vacuum-based methods.

In this thesis, three new non-vacuum deposition techniques have been studied:

- the spin-coating of a sol-gel,
- the drop-casting of a suspension composed of thiourea-metal complexes
- the blade-coating of a metal formates containing concentrated solution.

For all the methods developed in this work, the quality of the resulting absorber layers is evaluated in terms of phase purity, compactness of the film and performance of the solar cells. The CZTS(e) layers were analysed by scanning electron microscopy, energy-dispersive spectroscopy, Raman spectroscopy, optical microscopy and x-ray diffractometry. The devices were characterized with current-voltage measurements under illumination and external quantum efficiency measurements.

A particular focus was set on the feasibility of a deposition method at temperatures lower than the one normally used to growth CZTS (550 °C). The aim is to use flexible substrates like polyimide that cannot sustain temperature higher than 450 °C. Then the focus was shifted on the optimization of the process parameters, namely the solvent composition, the heating and cooling rates during thermal treatments, the concentration of the sulfur source and the use of a polymeric binder, in order to produce compact absorber layers,.

A preliminary study of sodium addition to the liquid formulation showed beneficial effects on the microstructure of the absorber and on the performance of solar cells produced in this work.

Only with absorbers grown via the first and third method we succeed in making working devices. In particular, with a CZTSe thin film (less than 700 nm thick) produced by depositing the ink composed of metal formates and a nitrogen-rich base plus a sodium source, the highest efficiency achieved for a solar cell was 3.1%. The J_{sc} (29.8 mAcm⁻²) extracted from the J-V curve under illumination matches with some much more efficient CZTSe cells reported in the literature, indicating a good quality of the absorber layer. The V_{oc} and the Fill Factor were 260 mV and 41% respectively, showing this low-cost solution process is very promising for further studies.

Acknowledgements

First of all I am grateful to Prof. Simona Binetti for supervising me. Thanks a lot for the patience, especially during these last days. I have to acknowledge the members of MIB Solar group Prof. Maurizio Acciarri, Dr. Alessia Le Donne, Dr. Andrea Scaccabarozzi, and Dr. Raluca Mereu for the fruitful discussions and scientific support in many occasions. I cannot list them all.

I would like to acknowledge Daniel Chrastina for the XRD measurements and Bruno Vodopivec for the SEM images and EDX measurements.

Many thanks to my undergraduate students Andrea Carella and Alexandra Colombo, whose hands substituted mines many times...

Last, but not least, I am extremely grateful to the head of the Laboratory for Energy Materials (LEM) Dr. Phillip Dale who hosted me and gave me confidence as if I was part of his group. I have never learnt so much in such a short period of time...thanks a lot to the members of the LEM and LPV group also: Ulrich Berner, Erika Robert, Alexandre Crossay, Thomas Schuler, Maxime Thevenin, João Malaquias, Dr. Diego Colombara, and Dr. Germain Rey.

Thank you all!

List of abbreviations

| | |
|--------|---|
| BSG | Borosilicate glass |
| CBD | Chemical bath deposition |
| CIGS | $\text{Cu}(\text{In,Ga})\text{Se}_2$ |
| CTS | $\text{Cu}_2\text{SnS}(\text{e})_3$ |
| CZTS | $\text{Cu}_2\text{ZnSnS}_4$ |
| CZTSe | $\text{Cu}_2\text{ZnSnSe}_4$ |
| CZTSSe | $\text{Cu}_2\text{ZnSn}(\text{S,Se})_4$ |
| EDX | Energy-dispersive X-ray spectroscopy |
| EQE | External quantum efficiency |
| FF | Fill factor |
| FWHM | Full width at half maximum |
| JV | Current-voltage characteristics |
| KCN | Potassium cyanide |
| MEA | Monoethanolamine |
| PV | Photovoltaics |
| PVA | Polyvinyl alcohol |
| PVD | Physical vapour deposition |
| RPM | Rotations per minute |
| RTP | Rapid thermal processor |
| SE | Secondary electrons |
| SEM | Scanning electron microscopy |
| SLG | Soda lime glass |
| TMG | 1,1,3,3 - tetramethylguanidine |
| XRD | X-ray diffraction |

Chapter 1

Introduction

1.1 Thin film chalcogenides as absorbers in photovoltaic devices

Solar energy reaching the Earth's surface is a huge resource that has not been harvested to an extent that could yield a strong environmental impact yet. It can be used directly for thermal applications like heating air or water, drying, distillation etc. A second way in which solar energy can be used directly is through the photovoltaic effect, that means converting solar power into electricity. In the literature, many materials able to absorb and convert solar radiation into electricity are studied. In Figure 1. 1 an overview of the variety of materials employed in different solar cells' technologies with respective record power conversion efficiencies is depicted.

In this landscape, silicon is still at the first place: it is abundant on the Earth crust (27% m%), its properties as a semiconductor are well known and silicon fabrication technology is such well developed that even Si-base photovoltaic devices have reached the commercial stage more than 25 years ago [1]. The types of silicon employed for photovoltaic applications are mainly the mono-crystalline and poly-crystalline.

Devices based on these materials are called “first generation photovoltaics”; they are characterized by bulk semiconductors doped in a manner that the single-junction structure is formed. Since silicon has an indirect energy gap, some hundred microns of material are necessary to absorb sufficient energy from sunlight to reach record efficiencies. Some solar cells based on polycrystalline Si films thinner than 100 μm are under investigation [2,3]. Moreover, devices containing Si as absorber usually require an anti-reflective coating or a particular texturing job to prevent sunlight to be reflected by the surface of the absorber. Last but not least, silicon wafers are obtained by sawing “solar grade” silicon ingots, which are produced by means of energy intensive processes such as Siemens purification, the Czochralski or Bridgman solidification processes [4].

To achieve the terawatt-scale power generation with photovoltaics, a sustainable PV technology must fulfil at least the following requirements: high and durable power conversion efficiency, availability of the raw materials and easy scalable manufacturing. In this research, inorganic chalcogenides have recently gained much attention because they have an energy gap very similar to that of silicon, but since they have a direct energy gap, only few micron thick films are necessary to absorb all the light that theoretically permits the same efficiencies reached by Si solar cells. Thin film technologies are also referred to as “second generation photovoltaics”. The semiconductors Cadmium telluride (CdTe), Cu_2InSe , Cu_2GaSe and $\text{CuIn}_x\text{Ga}_{(1-x)}\text{Se}_2$ belong to this category and some of them, namely CdTe and CIGS, have reached the same efficiency (around 20% on laboratory scale) and their production is at the commercial stage.

Polycrystalline CdTe (band gap=1.45 eV) films are grown by a variety of vacuum and non-vacuum deposition methods, but the highest quality is obtained by closed-space sublimation, optimized by the National Renewable Energy Laboratory (NREL) [5], and the solar cells are produced according to the “superstrate configuration”. During the last two years, the progress in the research of new post-deposition processes, such as annealing in CdCl_2 vapors at 400 $^\circ\text{C}$, plus the employment of higher temperatures (above 600 $^\circ\text{C}$) during growth, together with the use of a better quality glass (more transparent and with a higher strain point) led to the notable efficiency of 21.0% for laboratory solar cells [6]. First Solar is the leader company in CdTe technology with its 10 GW installed worldwide starting from 2007 [7]. CdTe modules developed by First Solar are now 17% efficient.

Thin films made of $\text{CuIn}_x\text{Ga}_{(1-x)}\text{Se}_2$ (CIGS) have been studied since the end of the 70's, as CdTe. Copper indium gallium diselenide is a solid

solution of copper indium selenide (CIS) and copper gallium selenide (CGS), with chemical formula $\text{CuIn}_x\text{Ga}_{(1-x)}\text{Se}_2$. The band gap of the material can be tuned by varying the relative quantities of indium and gallium incorporated in the material. Solar cells fabricated with the absorber $\text{CuIn}_x\text{Ga}_{(1-x)}\text{Se}_2$ where $x=0.30-0.35$ and $\text{Cu}/(\text{In}+\text{Ga})=0.80-0.92$, corresponding to a band gap of around 1.1 eV, can exhibit efficiencies up to 20% [8]. CIGS absorber layer is formed mainly by the co-evaporation of the elements or the deposition of the metallic precursor layers by sputtering followed by selenization. Co-evaporation yields devices with the highest performances, while the latter deposition process is preferred for large-scale production since it allows to obtain better compositional uniformity over a large area.

Several companies deposit on soda-lime glass (SLG) a multistack of elemental layers of Cu, In and Cu-Ga alloys by DC sputtering, with a subsequent selenization at 520-550 °C in an atmosphere containing Se or H_2Se [9]. The path towards high quality CIGS regards mainly the real-time control of stoichiometry during its growth: it has been demonstrated that the best crystallinity is reached when CIGS growth process undergoes a “Cu-rich” step, so that the formation of a Cu_xSe liquid phase occurs [10].

SLG is the most common substrate, but research is looking for lighter and flexible alternatives, such as plastics or metal foils, to develop devices that can be installed on different surfaces than roofs or flat architectures.

The presence of sodium atoms in the absorbers is essential, whether coming from the glass or introduced by different processes during fabrication. Currently, the material with best features is produced at ZSW, with record efficiency 21.7% [6]. Many firms are involved in the production of CIGS solar cells, both on rigid and flexible substrates, and modules currently available on the market are rated for around 15% efficiency [11-13].

The need for further reduction of fabrication cost led to a widespread variety of deposition methods based on solutions that can be coated easily without the use of high vacuum. Among the most successful, blade coating of an ethylcellulose paste containing Cu nitrate, In chloride, Ga nitrate and methanol plus selenization in a two zone oven with Se vapors adopted by Kaelin et al. [14] seems the most promising, whereas nanoparticle routes still look too much laborious and too few efficient [15, 16] to be up-scaled at an industrial level.

Despite the large development of these two chalcogenides, their composition comprises elements which are either not abundant on the Earth's crust such as Te, that is a byproduct of Cu mining, characterized by a complex recovery process, or very expensive such as In, a rare element of considerable industrial importance.

Another class of chalcogenides is the kesterites family, which comprises all the quaternary alloys with the minimum formula $\text{Cu}_2(\text{Fe,Zn})(\text{Sn,Ge})(\text{S,Se})_4$.

Kesterites share many properties with the chalcopyrite CIGS [17], but the constituent elements are of higher Earth abundance. To have an idea, in Figure 1. 2, an overview of the abundances in the Earth's crust and updated prices of the metals and chalcogenides composing the aforementioned semiconductors is presented. Among the possible cross-substitutions to obtain quaternary materials with the formula $\text{I}_2\text{-II-IV-VI}_4$, the compounds $\text{Cu}_2\text{ZnSnS}_4$ and $\text{Cu}_2\text{ZnSnSe}_4$ have shown to represent a good compromise between material cost and availability and possess the right features for photovoltaic application, thus, they are the most studied and encountered in the literature.

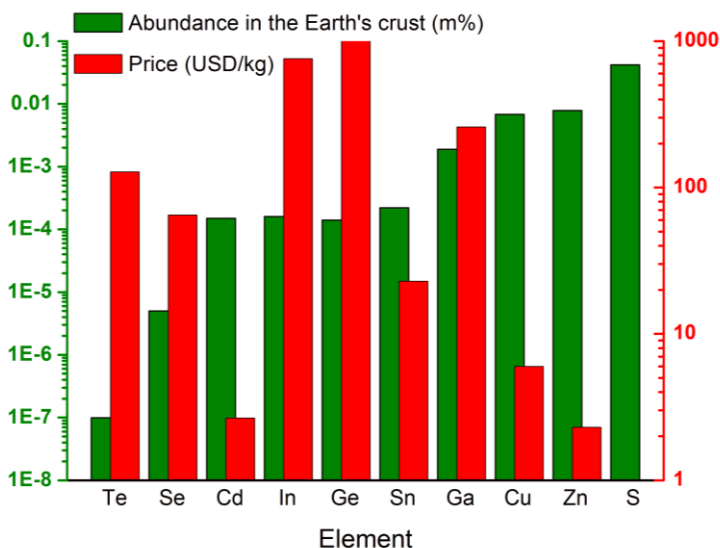


Figure 1. 2 Abundance in the Earth's crust (m%) and average price (USD/kg) of the main raw materials (as at least 99.0% pure sources) employed for the fabrication of thin film chalcogenides [18,19].

1.2 CZTS and CZTSe

The compounds $\text{Cu}_2\text{ZnSnS}_4$ and $\text{Cu}_2\text{ZnSnSe}_4$ have been reported to be p-type semiconductors, where doping is due to Cu_{Zn} antisites [20], with an absorption coefficient in the order of 10^4 cm^{-1} in the visible spectrum. Their band gap, determined experimentally, ranges from 0.9 eV for the pure selenide [21] and 1.5 eV for the pure sulfide [22] and it was found to strongly depend on the annealing conditions [23], stoichiometry of the absorber [24] and of course, temperature [25]. In CZTSSe it is tunable according to the content of sulfur over selenium [26]. It has to be kept in mind that the values reported in the literature come from an estimation that is always affected by the characterization technique chosen, that could be photoluminescence spectroscopy (PL), transmission spectroscopy in the UV-VIS of the absorbers or external quantum efficiency measurements (EQE) of the devices [27].

CZTS and CZTSe adopt the kesterite structure that can be obtained from the CuInSe_2 chalcopyrite by substituting half of the indium atoms with zinc and the other half with tin. The kesterite type structure is tetragonal (with $\bar{1}\bar{4}$ symmetry) and consists of alternating cation layers of CuSn, CuZn, CuSn and CuZn at $z = 0, \frac{1}{4}, \frac{1}{2}$ and $\frac{3}{4}$, respectively, as drawn in Figure 1.3. A detailed analysis of the crystal structures of CZTS and CZTSe is given by Schorr on the basis of experimental results [28].

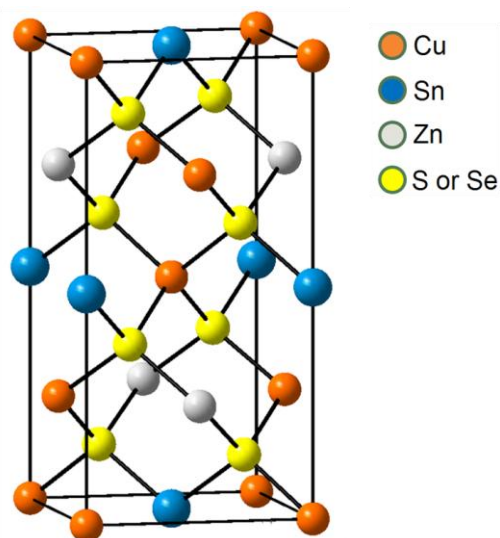


Figure 1.3 Unit cell representation of the kesterite structure.

Ab-initio calculations predict also other crystal structures for CZTS, such as the stannite and other tetragonal and monoclinic modifications, but the kesterite is the most stable [29, 30]. The lattice parameters, along with the differences in energy and bandgaps calculated for kesterite and other four low energy modifications are reported in Table 1. 1.

| | kesterite | stannite | modification | | |
|-----------------|------------|--------------|--------------|----------------|--------|
| | $\bar{I}4$ | $\bar{I}42m$ | $P\bar{4}2c$ | $P\bar{4}2_1m$ | $P2$ |
| <i>a</i> (nm) | 0.5448 | 0.5438 | 0.5446 | 0.5464 | 0.5443 |
| <i>c</i> (nm) | 1.0889 | 1.0941 | 1.0885 | 1.0857 | 1.0892 |
| ΔE (eV) | 0.0 | 0.054 | 0.012 | 0.390 | 0.272 |
| E_g (eV) | 1.487 | 1.295 | 1.458 | 1.206 | 1.073 |

Tab. 1. 1 Cell parameters and difference in energy and band gap of kesterite, stannite and other three modifications according to [31], [32] and [33].

1. 2. 1 Pseudo-ternary phase diagram

The concepts contained in this paragraph and the following are well studied and experimentally supported for the sulfur alloy, but can be transposed for the selenized as well. The formation of CZTS can be thought as a solid state reaction among the three chalcogenides Cu_2S , ZnS and SnS_2 . The formation of the polycrystalline CZTS suitable for PV application involves high temperatures at which some reaction of formation of secondary and ternary crystalline phases are thermodynamically favoured.

Assuming that the right amount of chalcogen is always introduced in the system and by using data from the phase equilibria in Cu_2S - ZnS - SnS_2 system given by Olekseyuk et al. [34], Scragg had proposed a detailed pseudo-ternary phase diagram (TPD) to summarize the crystalline phases that form depending on the elemental composition of the film [35]. Cu_2ZnSnS_4 as a single phase is present only within a narrow compositional window in the TPDs, which is indicated with an asterisk beside the centre of the plot of Figure 1. 4. In all other regions of the phase diagram there are one or two secondary/ternary phases that form alongside CZTS. In literature, it is common habit to name the film composition or growth conditions according to the classification reported in Figure 1. 5.

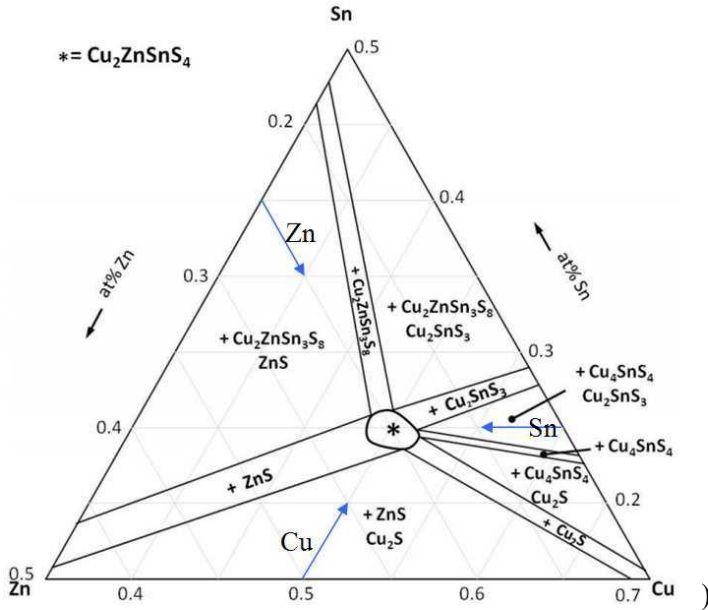


Figure 1.4 Ternary phase diagrams from [35], showing the expected secondary phases at 400°C.

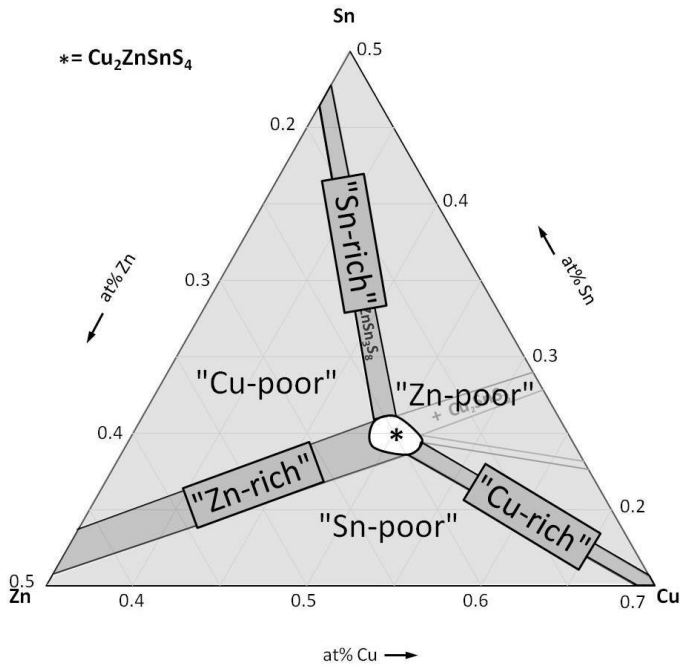


Figure 1.5 Ternary phase diagram from [35], showing the classification of film composition under off-stoichiometry conditions (asterisk indicates where single phase CZTS is formed).

Washio et al. studied the dependence of solar cells efficiencies on the metal amount in the films (see Figure 1. 6) and found that the best cells were built under Zn-rich (where $\frac{Zn}{Sn} > 1$), and Cu-poor (where $Cu/(Zn+Sn) < 1$) conditions [36]; the intersection of the corresponding areas is the most investigated compositional region of the, even though this leads unavoidably to the formation of the secondary phase ZnS.

The main concern behind the formation of crystalline phases other than CZTS is due to their detrimental effects on solar cells performances. In the next paragraph, the most detrimental secondary and ternary phases that may have formed in this work are briefly described.

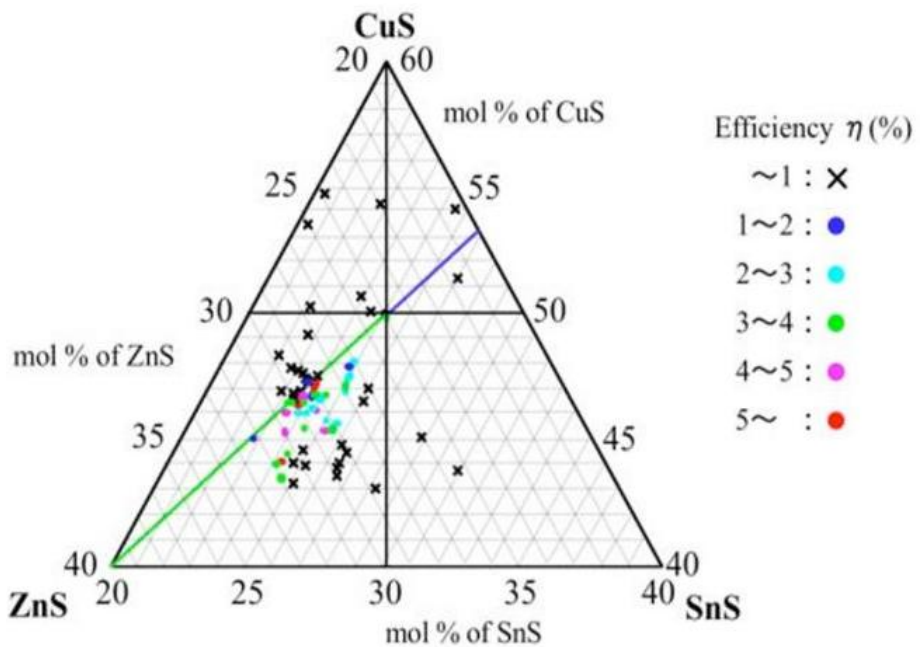


Figure 1. 6 Efficiency map of CZTS thin film solar cells in the CuS–ZnS–SnS pseudo-ternary phase diagram from [36].

1. 2. 2 Detrimental phases

- **Cu₂S** phases appear in Cu-rich or Sn-poor conditions. They are heavily doped low bandgap semiconductors, thus they have a metallic behaviour, meaning that they can shunt the solar cells if their grains are big or in such a quantity that connect the front to the back electrode in the device [37,38].

Small Cu₂S crystals act as traps for electrons and holes and enhance recombination. Since at usual growth temperatures (500 °C or higher) CuS, CuSe and Cu₂Se are liquid, a Cu-rich step during CZTS(e) fabrication would promote grain growth as already demonstrated for CIGS [10].

If the Cu-rich step is chosen and the undesired phase is present only on the top of the absorber, it can be successfully removed by an etching in KCN solution. In this case, the formation of inclusions or pin holes in the absorber could represent an additional problem. However, the presence of copper sulfides and selenides can be easily detected by Raman spectroscopy or X-ray diffraction [39,40].

- **ZnS** can form in the Sn and Cu-poor as well as in the Zn-rich areas of the TPD. According to the two possible crystal structures it has a bandgap ranging from 3.5 to 3.7 eV [41], wide enough to be considered as an insulator. Therefore the effects of its presence are both the reduction of the active area of the solar cell and blocking the current conduction.

ZnS is easily etched with HCl solutions [42], while for ZnSe an oxidative route is much more effective [43]. They are both detectable if present on the surface of the absorber by near-resonant Raman scattering [44,45].

- **Cu₂SnS(e)₃**, the ternary phases abbreviated CTS, have metallic properties as the copper secondary phases, thus they can enhance recombination or shunt the cell according to their amount and grain dimensions [46]. They are likely to form in Zn-poor conditions.

Both Zn secondary phases and CTS(e) share the structural motif with the respective kesterite, thus their certain detection by XRD is not possible.

Eventually, the best way to avoid the presence of the ternary phases is to grow kesterites in a compositional regime far from where the formation of the secondary and ternary phases is favoured.

1. 2. 3 $\text{Cu}_2\text{ZnSn}(\text{S}_x,\text{Se}_{1-x})_4$ fabrication methods and state of the art of $\text{Cu}_2\text{ZnSn}(\text{S}_x,\text{Se}_{1-x})_4$ -based solar cells

The fabrication techniques of CZTS(e) can be splitted into two categories: ‘single-stage’ and ‘two-stage’ processes.

A single-stage process permits the fabrication of the complete, crystalline film in one step. Some examples of one step processes are the spray-pyrolysis of solutions containing the metal salts and molecules containing the desired chalcogen (such as thioacetamide [47] or thiourea [48]) or co-evaporation of the elemental sources on a heated substrate [49].

The second type of fabrication methods consists of the deposition of the precursor layer which is defined as a layer containing the elements Cu, Zn and Sn in the metal form or in an unreacted form. In the second stage, the chalcogen is added by heating the precursor, usually in an atmosphere containing a source of S or Se. This step is usually referred to as sulfurisation or selenisation and leads to the crystallization of the kesterite phase and densification of the film. The first step can be carried out in many different ways, examples from the literature include electrodeposition [50], electron beam evaporation [51], sputtering [52], chemical vapor deposition [36], pulsed laser deposition [53], nanoparticle route [54] and many solution-based methods, also referred to as “ink-based methods” or “wet methods”. The latter are gaining much attention because they are relatively easy processes that don’t require any high-vacuum. Moreover, they often involve solutions or suspensions which contain all the metal constituents; this condition should favour their homogenous alloying during the formation of the precursor layer, because their intermixing happens at a molecular level.

Since solvents and anionic counterparts and, sometimes, “sacrificial” ligands are mandatory in the formulation of the liquid that has to be deposited, the resulting absorber layers are usually characterized by contaminations, even though the high temperatures usually involved in the fabrication of the absorbers should ensure solvent evaporation and thermolysis of organic residues. Halides, nitrogen, oxides and, of course carbon are the main species that can be found in a kesterite thin film grown by direct solution deposition. The role of these contaminants has not been investigated sufficiently yet, thus it is very difficult to assess if their presence is always a drawback for the solar cell operation.

One advantage of studying CZTS(e) is that much of the knowledge regarding CIGS can be somehow used also for the kesterites. Besides similar preparation of the precursor layers, annealing conditions and characterization techniques, also the structure of the solar cells adopted is the same for CIGS (as depicted in Figure 1. 7). It consists of a substrate that acts as a support for the electrode layer, which is a few hundred nm thick molybdenum film, usually deposited on the substrate by sputtering. On top of it, the p-type absorber layer is deposited. It is usually 1 to 2 μm thick.

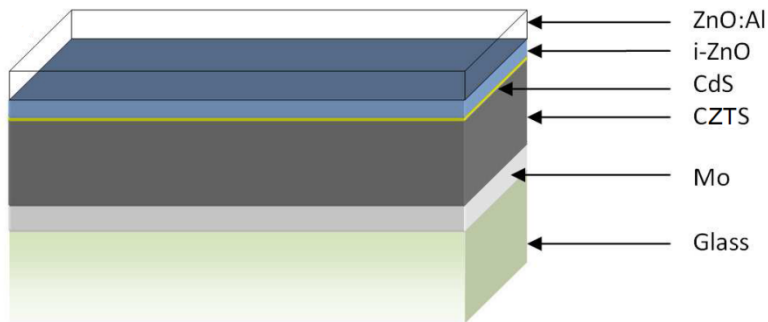


Figure 1. 7 Architecture of a typical thin film CZTS solar cell.

After a chemical bath deposition in a Cd and S containing solution, a 50 to 70 nm thick CdS film is formed. CdS is the n-type semiconductor in the p-n junction and it is usually referred to as “buffer layer”. The finalization of the cell proceeds then with the sputtering of a bilayer of ZnO-based transparent conducting oxides (TCOs): intrinsic zinc oxide (i-ZnO)

and aluminium doped ZnO (ZnO:Al) are the most common. A grid of metallic contacts (usually structured as aluminum strips and pads) is then evaporated on top of the conducting window layer.

For what concerns the best kesterite based solar cell efficiencies, the record for CZTS is held by Shin et al. [55]. The 8.4% power conversion efficiency was achieved by evaporating the metal sources at low temperature (150 °C) plus a the sulfurization step on a hot plate at 540 °C using a commercially available valve cracker. A cross-section and the device characteristics of the best solar cells are merged in Figure 1. 8. Interestingly, the annealing times to obtain such a homogenous material were in the order of few minutes, and, despite the reduced thickness of the absorber, a reasonably good short-circuit current was measured.

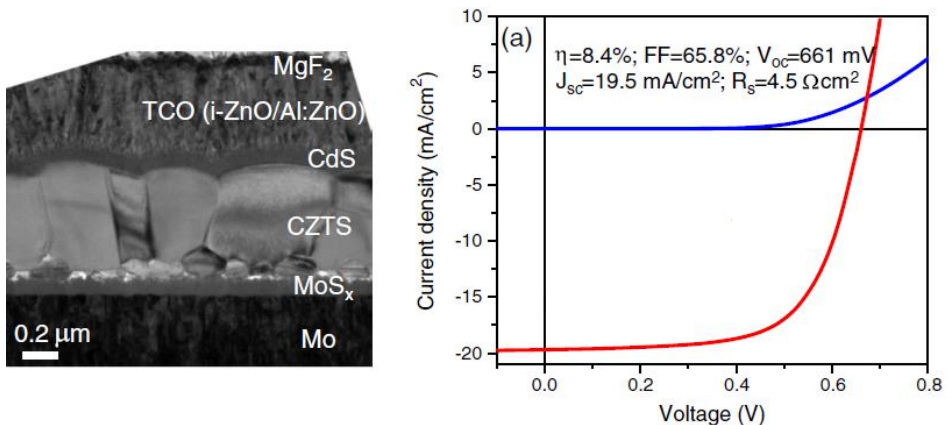


Figure 1. 8 Bright field TEM image and the device characteristics of the 8.4% Cu₂ZnSnS₄ (CZTS) champion solar cell from [55].

The best CZTSe solar cells are produced by Imec and Solliance, by means of an industry relevant technology composed of sputtering of Cu, Zn and Sn metal layers followed by selenization in H₂Se/N₂ environment for 15 minutes at a temperature of 460°C [56] which led to a PCE of 9.7% in 2013. Figure 1. 9.

Another successful example of CZTSe solar cells is produced by Repins et al. by means of a four sources thermal co-evaporation process which led to a PCE of 9.15% in 2012 [57]. Equipment and procedures used to make the kesterite films are nearly identical to those previously described related to CIGS processing at NREL. They also demonstrated that heating

the absorber at low temperature prior to CdS deposition improves the FF factor by 5% absolute. The SEM cross section of the absorber before finalization and the characteristics of the best solar cell are presented in Figure 1. 10.

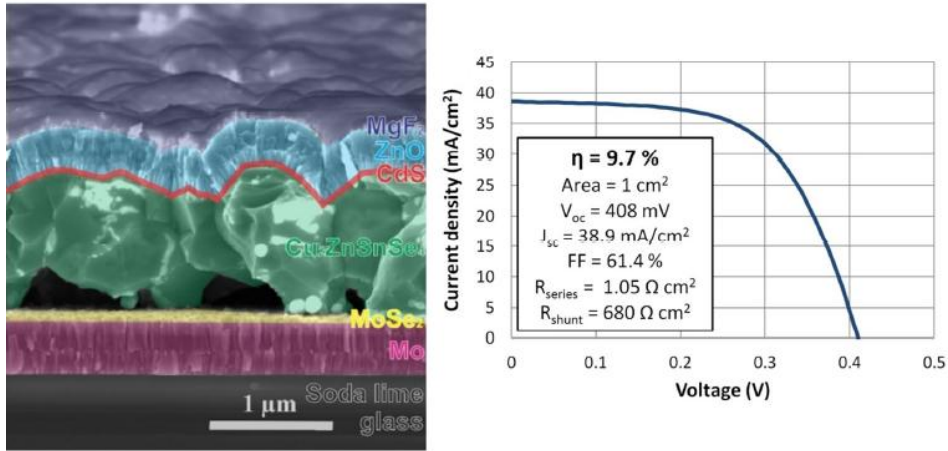


Figure 1. 9 Cross-section SEM image of the world record CZTSe solar cell and J-V characteristic of the best 1.0 cm² solar cell under illumination from [56].

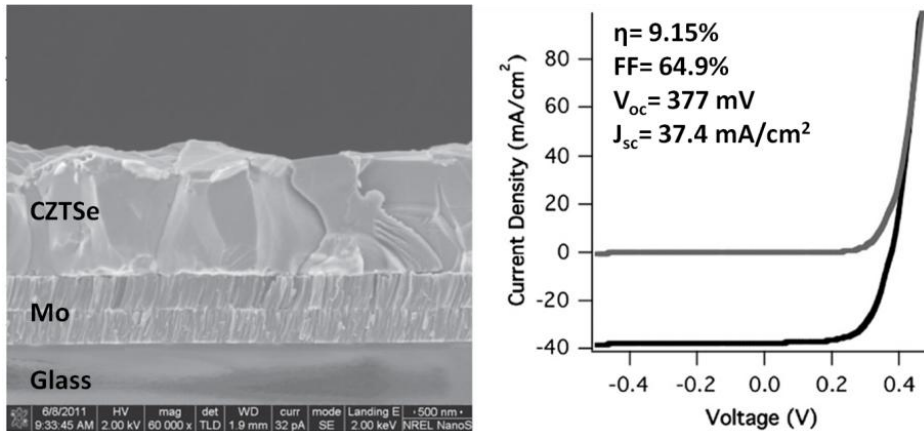


Figure 1. 10 SEM cross-section of the most efficient Cu₂ZnSnSe₄ absorber and characteristics of the champion device from [57].

It is worth noticing that all these champion devices are built with absorbers obtained by vacuum methods. Evaporation and sputtering are extensively used for the production of multinary inorganic films, and in most cases the procedures derive from pre-existing CIGS fabrication processes.

The advantages these vacuum-based methods are: high control of stoichiometry, the minimization of impurities in the inorganic films and a relatively high reproducibility.

In the perspective of a mass production of large areas absorber layers, fabrication methods based on solution processing are much more convenient.

Liquid formulations can adapt to different deposition techniques (spin-, dip-, curtain-, blade-coating) that might be implemented in a roll-to-roll industrial process. Therefore, despite the incomplete knowledge about methods for the detection of contaminants and thus their influence on solar cells operation, wet processes are intensively under study and in the literature new chemical strategies are proposed frequently. In this regard it is worth mentioning that CZTSSe device efficiency record of 12.7% is held by the IBM laboratories [58], with the absorber produced by a non-vacuum solution approach that involves hydrazine [59]. The cross-section of the absorber and the characteristics of the best device (comprising an additional In_2S_3 emitting layer on top of the CdS) are depicted in Figure 1. 11. Hydrazine (N_2H_4) is a powerful reducing agent that, in presence of excess chalcogen (S, Se, Te), can solvate different metal chalcogenides as hydrazinium-based complexes at room temperature. Its controlled degradation produces N_2 and H_2 only, which are gaseous products that are released during thermal treatment and thus should not leave any contaminant in the CZTSSe film [60]. Because of its high toxicity and flammability, finding alternatives with a high solvating power, reducing capability and “clean” products upon degradation is highly desirable.

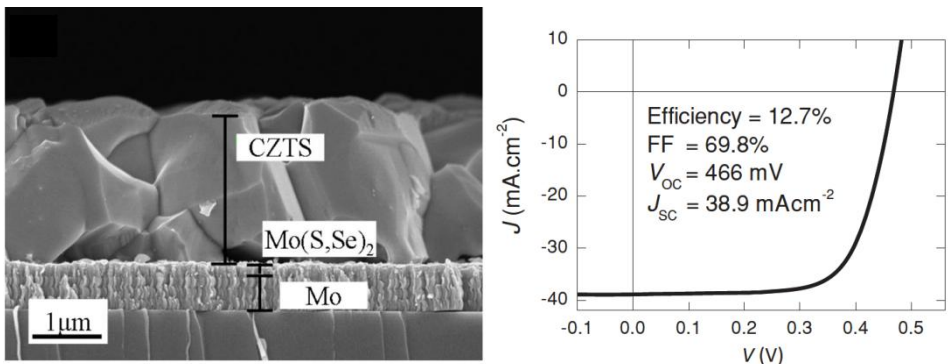


Figure 1. 11 SEM cross-section of the most efficient $\text{Cu}_2\text{ZnSn}(\text{S,Se})_4$ absorber from reference 58 and characteristics of the champion device from [59].

The champion kesterite-based solar cells mentioned in the previous paragraph were built on soda-lime glass (SLG) substrates with the absorber processed at temperature higher than 450 °C. At these temperatures the diffusion of Na atoms from the glass to the absorber is unavoidable. In fact, it has already demonstrated that Na doping have beneficial effects on CIGS: its further addition improves the microstructure of the absorber, decreases resistivity, and increases Voc and efficiency of solar cells [61]; it is also speculated to create defects that can act as acceptors, improving the p-type conductivity. For CIGS it has been observed a preferential location for sodium at the surface and grain boundaries. The same effects have been proven for CZTS(e). An exhaustive examination of the relationships between grain boundaries, sodium content at these boundaries, non-radiative recombination, and surfactant effects that produce large microstructural changes in CZTS has been recently given by Gershon et al. [62].

The addition of sodium (but also other alkali, such as potassium [63,64]) is mandatory if the absorber is deposited on a Na-deficient substrate, such as borosilicate glass (BSG) [65], whose softening point occurs at higher temperature compared to SLG; plastic or steel foil, which might be chosen for their flexibility and thus their possible application in the design of Building Integrated Photovoltaics (BiPV), that is a hot topic nowadays [66].

In any case, sodium out-diffusing from a Na containing substrate (such as SLG) at high temperatures during evaporation or sintering of the absorber is not sufficient for good device properties, thus many strategies for the incorporation of Na in the absorber are under investigation. For instance, it can be evaporated as NaF capping layer on the absorber and annealed to trigger the diffusion inside the film. It has been proposed that in CZTSSe the Na₂Se liquid phase supplies for reactive selenium and promote grain growth even at low temperatures. Sutter-Fella has demonstrated that there's a Na concentration limit where CZTSSe gets benefits from doping in terms of crystal growth, but once this limit is surpassed, the formation of a Na-based secondary phases doesn't contribute positively to the absorber [67]. The NaF layer can be also evaporated on top of the back contact instead of on the top of the absorber [68]. Oo et al. demonstrated that sodium is successfully incorporated in CZTS layers sputtered on BSG by dipping them in a Na₂S containing solution before an annealing at 600 °C [69].

In wet processes another strategy to add sodium to the absorber consists of using a Na containing reagent incorporated in the solution or suspension of the metal sources [70]. Once again, this choice may be

considered more convenient in terms of feasibility because it doesn't add any additional step to the process and in principle favours the intermixing of sodium atoms with the constituents of the absorber.

Chapter 2

Fabrication and characterization techniques

In this chapter a framework of the deposition methods and brief descriptions of the equipment used to characterize thin films and devices produced in this work are given.

2.1 Deposition of precursors

Substrate preparation

The substrates for the deposition of the samples were 2 mm thick soda-lime glasses on which a 700 nm thick layer of molybdenum was sputtered. Before the deposition of the Mo layer, the glass slides were cut

into 1x1 inch pieces, cleaned in ultrasonic bath with 5% Alconox® solutions and washed three times in bi-distilled water.

Spin-coating

The spin-coating process can be divided into four steps as depicted in Figure 2.1. The deposition step involves pouring an excessive amount of liquid onto a stationary or slowly rotating substrate. In the spin up stage, the substrate is accelerated to a final spin speed. The spin off step is the stage where the excess solvent is flung off the substrate surface as it rotates at high speeds (usually more than 1000 RPM). The fluid is being thinned mostly by centrifugal forces until enough solvent has been removed to increase viscosity to a level where flow ceases. After this stage, evaporation becomes the primary cause of film thinning. Indicatively, the thickness of a layer deposited by spin-coating is inversely proportional to the speed of rotation and directly proportional to the viscosity of the liquid. An exhaustive one-dimensional model of the process is given by Bornside et al. [20].

The machine used in this work for the spin-coating routine is a G3P-8 from Specialty Coating System.

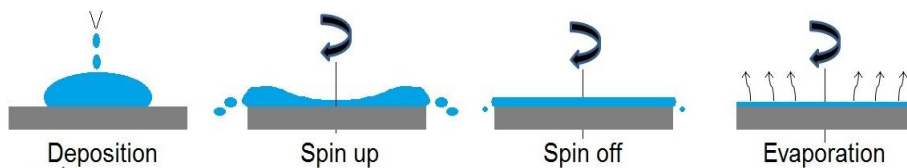


Figure 2. 1 The four stages of spin coating.

Dip-coating

As for spin coating, this process can be broken into four steps, as resumed in Figure 2. 2. First the substrate is immersed into a solution of the coating material, preferably at constant speed. The substrate is kept in the liquid for some seconds and as soon as it is pulled out of the solution the deposition step takes place. Readily most of the solvent has been drained off the substrate and evaporation begins. A report regarding the recent progresses in the preparation of thin films by this technique and how to control each of the (chemical and mechanical) parameters is given by Grosso [21].

Some samples presented in this thesis were produced using the customized dip-coater pictured in Figure 2. 3.

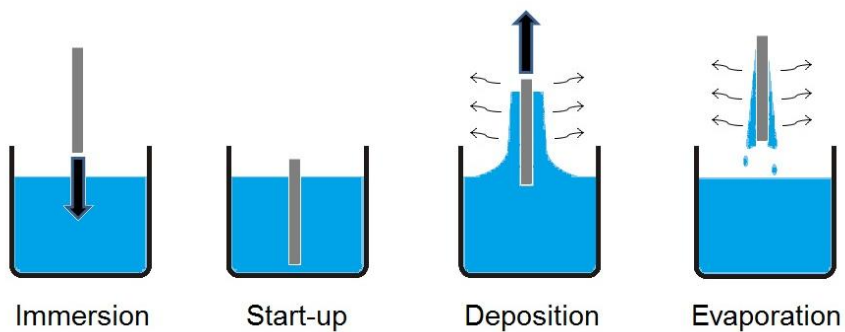


Figure 2. 2 The main stages of dip-coating.



Figure 2. 3 Picture of the home built equipment used in this work for dip coating.

Drop casting

Drop casting is perhaps the easiest way to deposit a liquid on a substrate. Samples presented in section 3.2.3 are produced by means of this simple technique.

In our laboratory we developed a method to control the amount of liquid deposited by confining it with a frame made of polydimethylsiloxane (PDMS) cured directly on molybdenum coated substrates (see Figure 2. 4). After the evaporation of solvents, the frame can be easily peeled off.

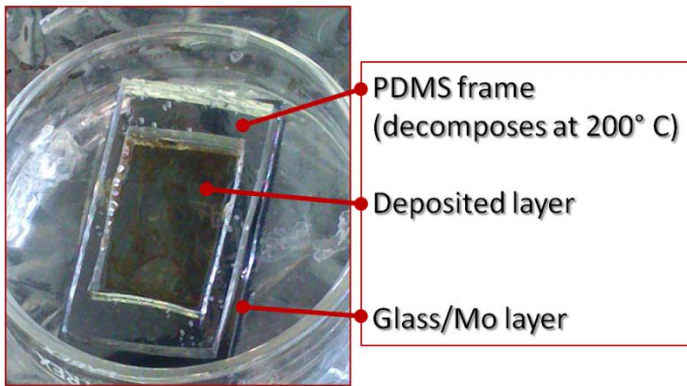


Figure 2. 4 Picture of a sample deposited by drop casting a solution inside a polydimethylsiloxane frame directly cured on molybdenum layers.

Blade-coating

Also known as knife-coating or doctor-blading, it uses a very precise spacer under which the coating liquid is deposited. The latter is then spread over the substrate by moving the blade at a constant rate. As for spin coating, to assure the complete coverage of the sample area, an excess of coating solution is needed. A simple sketch of how knife coating works is depicted in Figure 2. 5.

All the samples presented in Chapter 4 are prepared using a Zenthner ZAA 2300 automatic film applicator and a ZUA 2000 universal applicator with a gap above the substrate of 350 μm .

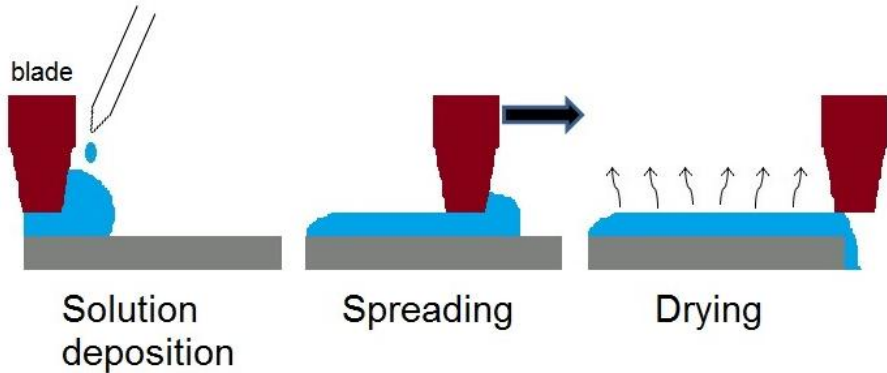


Figure 2. 5 The main stages of blade-coating.

2. 2 Annealings

CZTS

The thermal treatments carried out in order to obtain CZTS samples described in section 3. 1 and 3. 2 were performed in a tube furnace, which had a PXR4 Microcontroller (Fujielectric) for temperature programming. The samples were placed into a quartz boat inside a sealed quartz tube. The treatments were carried out in argon flux (30-40 ml/min) after purging for 30 min with a 100 ml/min flux. The exhaust gases were lead through hydrogen peroxide and sodium hydroxide containing scrubbers. As can be seen in Figure 2. 6, the sulfur source is heated at a lower temperature than the temperature at which samples have been annealed. This configuration was chosen in order to avoid a rapid escape of sulfur vapours and favour their reaction with the precursor layer.

Details about temperature ramps and their effects on the precursor and absorber layers' compactness are given in the description of the methods in Chapter 3.

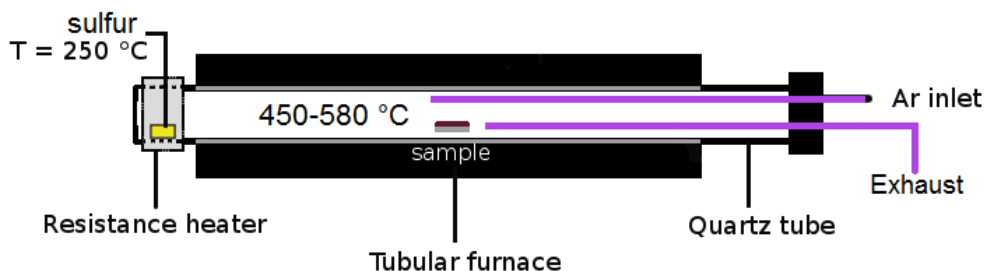


Figure 2. 6 Schematization of the sulfurization setup used to produce samples presented in Chapter 3.

CZTSe

All samples in Chapter 4 were annealed in a tube furnace (Elite Thermal System Limited – Type “TSH 12/38/250-2416”) with a home-built low vacuum/gas chamber that allows to choose among different background gases. The samples were placed inside a graphite box together with ca. 100 mg of selenium and 15 mg SnSe powders. After a 30 min treatment at $100\text{ }^{\circ}\text{C}$ under vacuum, the graphite box was conditioned with 10 mbar of forming gas (90 vol% N_2 and 10 vol% H_2) and heated up to $550\text{ }^{\circ}\text{C}$ for other 30 min. After the annealing, the system was left to cool naturally and samples were removed from the oven at room temperature to avoid the formation of metal oxides. The exhaust of the annealing was lead through a Zn acetate containing scrubber in order to neutralize the contingent H_2Se that could have formed and not reacted with the precursor film. A representation of the annealing setup is sketched in Figure 2. 7 and the temperature profile of a typical annealing run is depicted in Figure 2. 8.

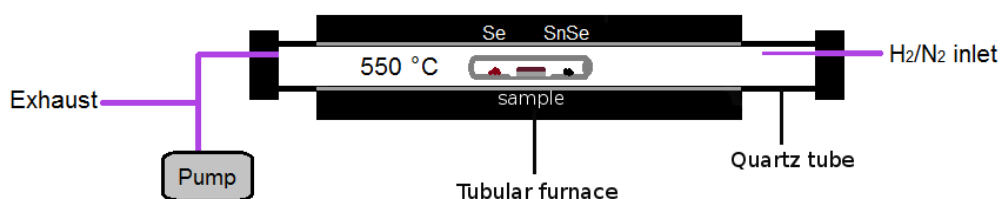


Figure 2. 7 Schematization of the selenization setup used to produce the samples presented in Chapter 4.

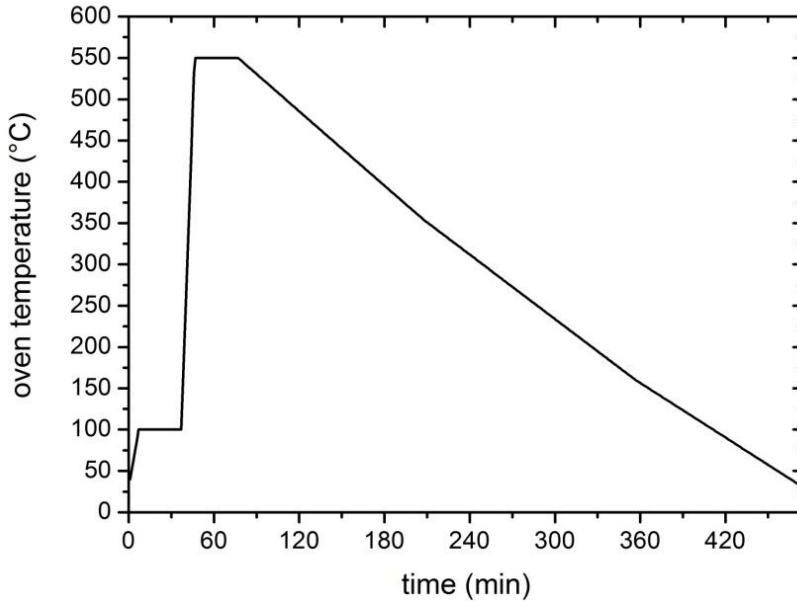


Figure 2. 8 Typical temperature profile of the annealing for producing CZTSe samples presented in Chapter 4.

Rapid thermal processing

Some precursor layers presented in chapter 4 were treated in a rapid thermal processor (RTP) which consists of a infrared heated furnace (AS-One100, Annealsys) and allows heating rates of a few seconds and rapid cooling rates as well. The schematic of RTP annealing setup used in this work is depicted in Figure 2. 9. To ensure the uniformity of heat transfer during rapid heating and cooling precursor layers were placed in a graphite box covered with a lid. A K-type thermocouple (TC) inserted to the graphite box close to the sample assured the monitoring of the temperature. The RTP system used here had a rotary pump to allow a vacuum of around 10^{-2} mbar and a N_2 purge line to flush the system. The treatments were carried out under pressure of forming gas (100 mbar of 10% H_2/N_2) and the temperature ramps were set in order to have a constant heating rate of $20\text{ }^\circ\text{C/s}$ and an average cooling rate of $15\text{ }^\circ\text{C/min}$.

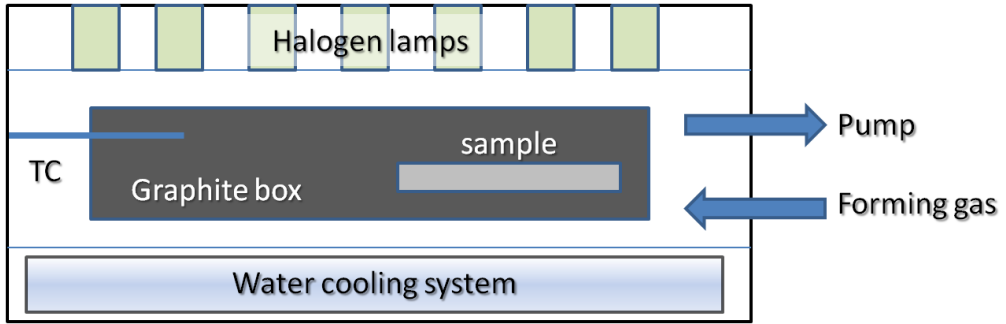


Figure 2. 9 Main components and geometry of the RTP system used in Chapter 4

2. 3 Building the device

The CZTS and CZTSe layers were grown on 700 nm thick layers of molybdenum sputtered on common SLG. Some devices were built in the MIB-Solar laboratories (Milano Bicocca University), while some others in the LEM laboratories (University of Luxembourg). The first process will be referred to as “MIB finalization” and the latter as “LEM finalization”.

MIB finalization: on top of the absorber layers CdS (50-70 nm thick) was deposited by chemical bath deposition (CBD), intrinsic ZnO (80-100 nm) and Al doped ZnO (150 nm) were deposited by RF and pulsed DC sputtering, respectively. Aluminum strips were deposited by thermal evaporation. Multiple solar cells with total areas varying from 0.15 cm² to 0.5 cm² were scribed mechanically using beryllium-copper masks.

LEM finalization: the absorber layers were etched in a 5 wt% KCN aqueous solution for 30 seconds and put in the chemical bath to deposit CdS on their top. ZnO and Al doped ZnO were deposited via magnetron sputtering followed by e-beam evaporation of Ni-Al grids.

Solar cells with a total area of 0.5 cm² were scribed mechanically. None of the two finalization procedures used an antireflection coating, thus the schematic of the devices can be sketched as SLG/Mo/CZTSe/CdS/i-ZnO/ZnO:Al/(Ni-)Al. The products of these two processing can be seen in Figure 2. 10.

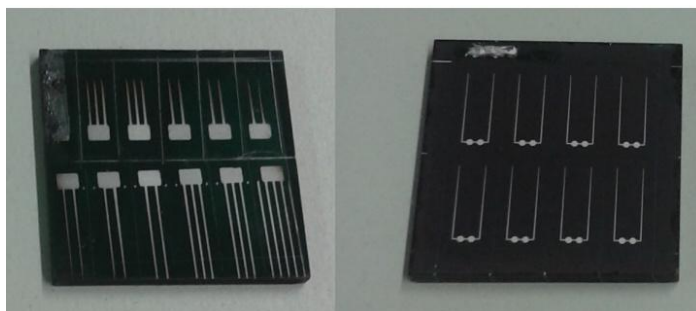


Figure 2. 10 Solar cells produced at (left) MIB Solar and (right) LEM laboratories.

2.4 Characterization of precursor and absorber layers

Scanning electron microscopy and energy dispersive X-ray spectroscopy (SEM-EDX)

In this thesis SEM is the technique used to analyse the microstructure of the thin films produced. By looking at a SEM micrograph, one can have an idea of the compactness of the material, average grain size (unless it is in the order of a few nanometers) and sometimes the presence of undesired species embedded in the film or leaning on its surface. By EDX analyses, the atomic composition of the precursor layers and annealed film were investigated. The images and elemental analyses presented in sections 3.1 and 3.2 and part of 3.3 were taken with the following equipment: Tescan VEGA TS5136XM scanning electron microscope with operating voltage of 20 kV, equipped with EDAX Genesis 4000 XMS Imaging 60 under the same operating voltage, working distance of 23 mm and calibration with 53 Minerals Standard Mount MINM25-53.

Some of the SEM measurements presented in section 3.3 were performed on a Hitachi SU-70 with an acceleration voltage of 7 keV and at the high current mode and a working distance of 5 mm to ensure an optimal resolution. The EDX analyses were collected at 20 keV if not differently specified.

Profilometry

The thickness of the films was measured with a Veeco Dektak 8 profilometer, equipped with a stylus with radius of 12 μm .

Raman spectroscopy

The Raman spectra were collected at room temperature with a Jasco Ventuno micro-Raman in backscattering configuration using a helium-neon laser with a power of around 7 mW (spot diameter $\approx 4 \mu\text{m}$). The resulting power density and exposure times are chosen in order to avoid local warming, which causes either the Raman shift to temporarily move towards lower wavenumbers or induces chemical changes in the film.

X-ray diffraction

The crystalline phases in the as-deposited and annealed samples presented in Chapter 4 were analysed by x-ray diffraction in ω - 2θ configuration using a PANalytical X'Pert PRO MRD high-resolution diffractometer with a Cu- $K\alpha$ radiation source at 45 kV and 40 mA. All the other XRD measurements were collected by a Bruker D8 Advance diffractometer (Cu- $K\alpha$ radiation, 40 kV, 30 mA) with θ - 2θ geometry and secondary curved beam monochromator. The scan steps were 0.02° for both the machines.

2. 5 Electrical measurements

The CZTS(e)-based solar cells were inspected both by external quantum efficiency and current–voltage (I–V) measurements. EQE measurements were obtained with a SpeQuest quantum efficiency system. The PV devices were illuminated by a chopped light beam with a diameter around 5 mm. The photogenerated current from the cell passed through an I–V converter and the corresponding voltage produced at each wavelength of the monochromatic light was measured by a lock-in amplifier monitored via PC. The spectral response curves of the PV device were taken from 350 nm to 1100 nm with a 10 nm wavelength increment. The EQE spectrum was then calculated as the ratio between the spectral response data and the incident

light spectrum, obtained with a reference photodiode (ThorLabs S120VC). I–V measurements were taken under Air Mass 1.5 conditions (simulating terrestrial applications) with a Thermo Oriel Solar simulator with a constant incident power density of 1 sun (100 mW/cm²) and a Keithley 2400 SourceMeter. Solar cells presented in Chapter 4 were either examined by means of the forementioned equipment or a home-built I – V setup equipped with an AM1.5 intensity equivalent calibrated halogen lamp (100 mW/cm²) to measure I–V characteristics in the dark and under illumination, and another home-built setup calibrated with a Si and an InGaAs photodiode for EQE measurements. The photocurrent was measured by using chopped monochromatic illumination from xenon and tungsten lamps and a lock-in amplifier was used to measure the photocurrent from 350 nm to 1600 nm with a 10 nm wavelength step.

Chapter 3

CZTS thin film fabrication

In this chapter, the depositions of $\text{Cu}_2\text{ZnSnS}_4$ by means of two wet processes developed in this work are described.

3. 1 Monoethanolamine containing sol-gel

3. 1. 1 Formulation and deposition of the sol-gel

$\text{Cu}(\text{NO}_3)_2 \cdot 3\text{H}_2\text{O}$, $\text{Zn}(\text{NO}_3)_2 \cdot 6\text{H}_2\text{O}$, and $\text{SnCl}_4 \cdot 5\text{H}_2\text{O}$ were dissolved in 2-methoxyethanol (anhydrous) in the same flask at room temperature. To avoid their precipitation, anhydrous monoethanolamine (MEA) was added. The addition of this stabilizer was followed by a change of the colour of the solution from light blue to dark blue, a heating and densification of the solution and solubilisation of previously insoluble particles. The solution was kept under vigorous stirring on a hot plate at 50 °C until the desired

rheology was obtained (typically after 40 min the sol-gel is ready to be deposited). Since the basicity of the salts and MEA could corrode the Mo layer ($pK_{a_{MEA}}=9.5$), two sol-gels were formulated: one concentrated and one diluted; in the latter deionized water was used in place of MEA. The composition of the two sol-gels are resumed in Table 3. 1. The sol-gel were used immediately after being prepared.

| | Conc sol-gel | Dil sol-gel |
|--------------------------|-----------------|-------------|
| | Composition (g) | |
| $Cu(NO_3)_2 \cdot 3H_2O$ | 4.945 | 0.983 |
| $Zn(NO_3)_2 \cdot 6H_2O$ | 3.743 | 0.744 |
| $SnCl_4 \cdot 5H_2O$ | 3.836 | 0.763 |
| MEA | 7.50 | - |
| 2-OCH ₃ EtOH | 17.50 | 17.50 |
| H ₂ O | - | 7.50 |

Table 3. 1 Composition of the two liquid formulations: in the concentrated sol-gel the total amount of salts is 1.75 M and in the diluted it is 0.35 M

To obtain precursor layers of suitable thickness, ten depositions in total were done using the diluted sol-gel first and the concentrated one afterwards, five times each. All the depositions were carried out with a final speed of 3000 rpm on molybdenum covered SLG substrates or bare SLG. The liquid was poured onto the substrate before the stage started to move. The sequence of steps adopted is depicted in Figure 3. 1.

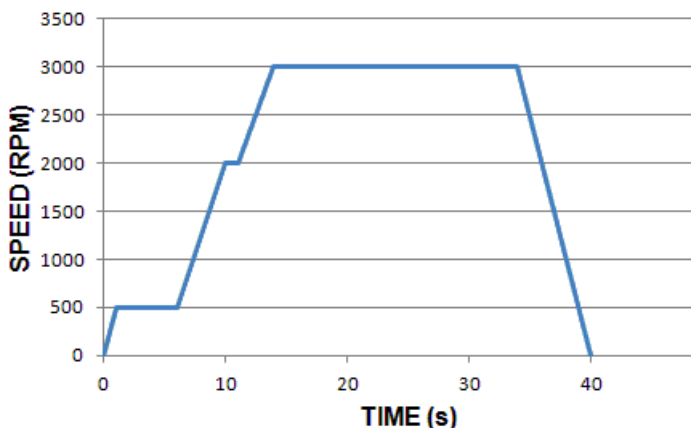


Figure 3. 1 Speed profile of a typical spin-coating run used in this work (RPM=rotations per minute).

After each spin-coating run, the samples were treated in air at 100 °C on a hot plate for at least 1 minute and at 200 °C in a stove for 3 minutes. The precursor layers formed were annealed with elemental sulfur (around 50 mg for each sample, for a maximum of four inch by inch samples in the same sulfurization run) at 500-580 °C in Ar flow for 1 h using the setup described in Chapter 2.

3. 1. 2 Characterization of absorber layers and solar cells

The SEM top-view of the precursor layer is shown in Figure 3. 2 and cross sectional views at different magnification are shown in Figure 3. 3. The roughness of the surface of the precursor layer can be inferred to the evaporation of the liquid component of the sol-gel (b.p._{MEA}= 170 °C, b.p._{2-OCH₃EtOH}= 124 °C) after each deposition. Macroscopic bubbles are visible also at low magnification. A reliable quantification of each atomic specie was not feasible because the sample was burnt in any attempt of collecting a EDX spectrum indicating a predominant amount of organic residuals at this stage. The thickness of the layer is around 3 μm.

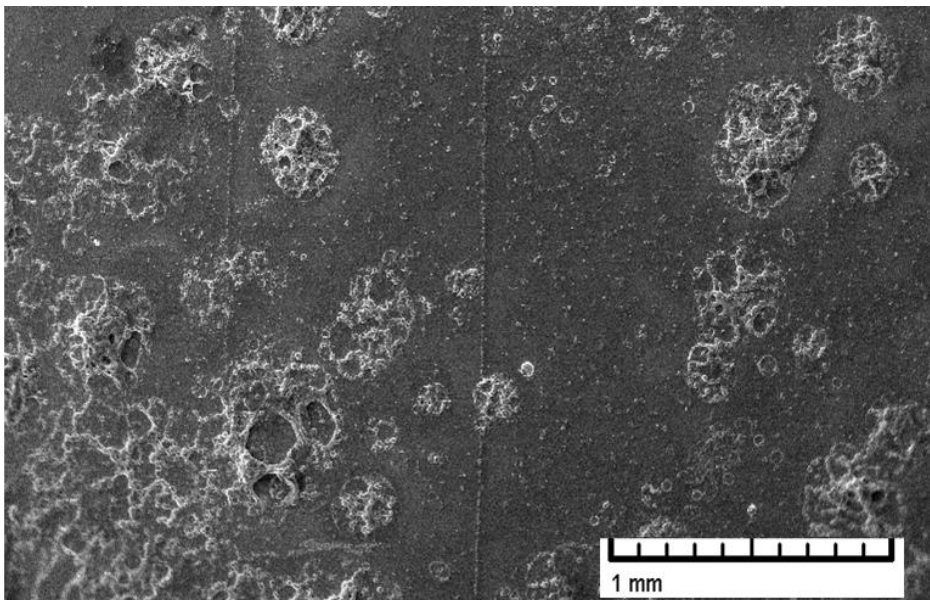


Figure 3. 2 SEM top-view of the precursor layer.

In Table 3. 2, the compositions of the sol-gel and the average composition of the absorber layers grown at 500 °C measured by EDX are listed (sol-gel 1 and CZTS 1). Since Zn has a high vapour pressure (the highest among the three metals), it is very likely that the Zn depletion observed is due to its evaporation during the annealing. To reach at least the stoichiometric Zn content, a Zn-richer sol-gel was formulated (sol-gel 2). Its composition and the composition of the resulting absorber layer grown at 500 °C are listed in the same table.

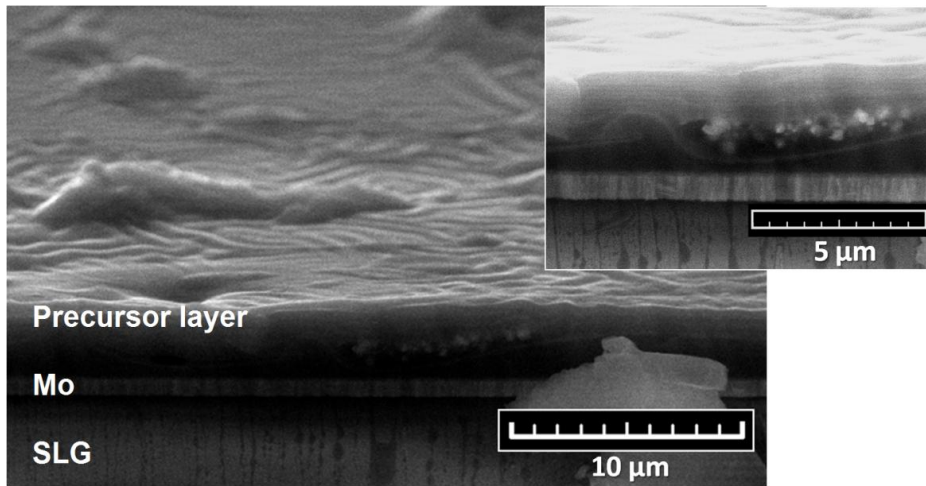


Figure 3. 3 SEM cross section view of the precursor layer.

| | Elemental composition expressed as ratios of atomic percentages. | | | |
|---|--|-------------|-------------|-------------|
| | Sol-gel 1 | CZTS 1 | Sol-gel 2 | CZTS 2 |
| $\frac{\text{Cu}}{\text{Zn} + \text{Sn}}$ | 0.87 ± 0.04 | 0.84 ± 0.07 | 0.87 ± 0.04 | 0.95 ± 0.07 |
| $\frac{\text{Zn}}{\text{Sn}}$ | 1.16 ± 0.02 | 0.88 ± 0.04 | 1.35 ± 0.02 | 1.03 ± 0.04 |

Table 3. 2 Compositions of sol-gels and resulting absorber layers (from EDX, 20 kV, 50x50 μm windows).

The layer sulfurized at 500 °C appears composed of sub-micron angular shaped crystals (see Figure 3. 4), with some agglomerates leaning on the surface of the film. By looking at the cross-section (Figure 3. 5) a high roughness is observable, and the film looks much less dense if compared with the precursor layer. The thickness ranges from 1 to 1.8 μm , that implies a big loss of the organic components at high temperatures.

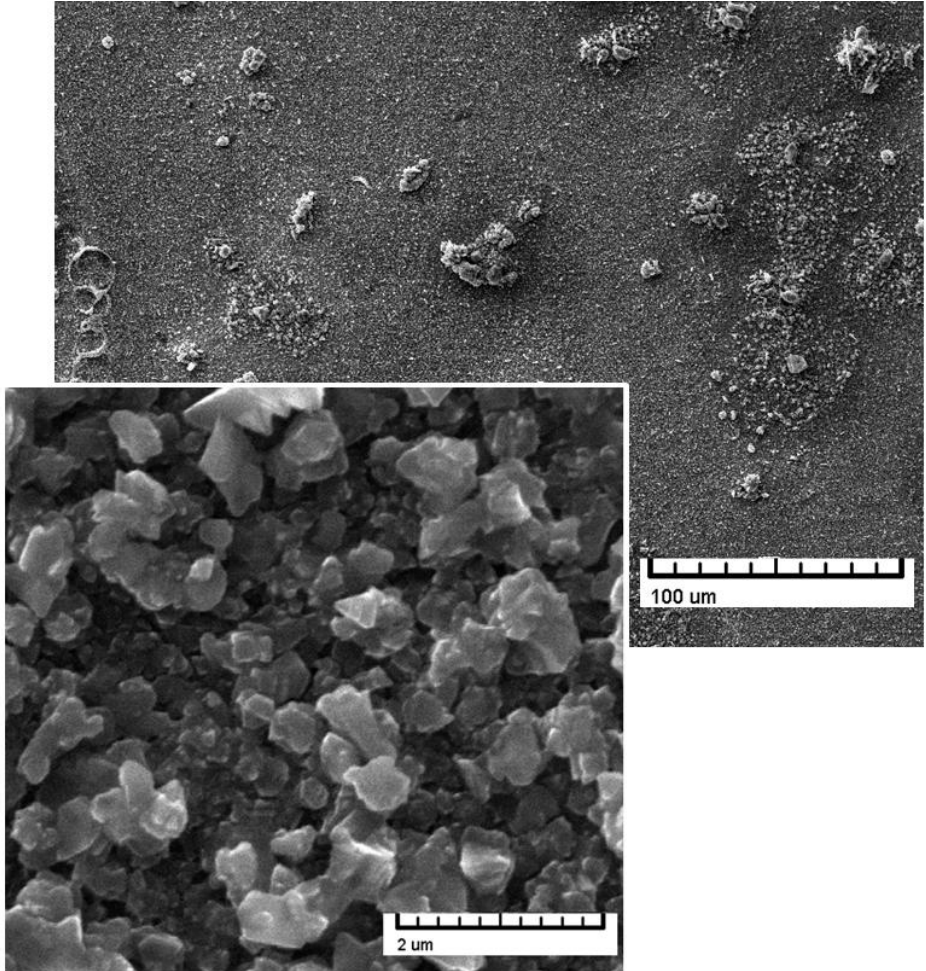


Figure 3. 4 SEM top views of the CZTS layer sulfurized at 500 °C.

Moreover, all the samples grown at this temperature (but also higher) in many regions investigated at the SEM are composed of CZTS “islands” separated by cracks with dimensions in the order of tens of microns and much wider “valleys” as shown in Figure 3. 6. In

correspondence of discontinuities it has been detected an appreciable quantity of chlorine atoms by EDX measurements. Chlorine hasn't been detected in other parts of the film.

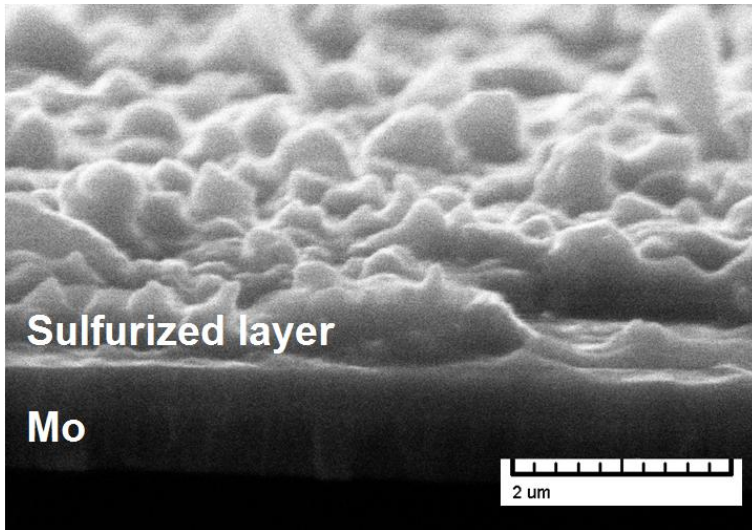


Figure 3. 5 SEM cross-section of the layer sulfurized at 500 °C.

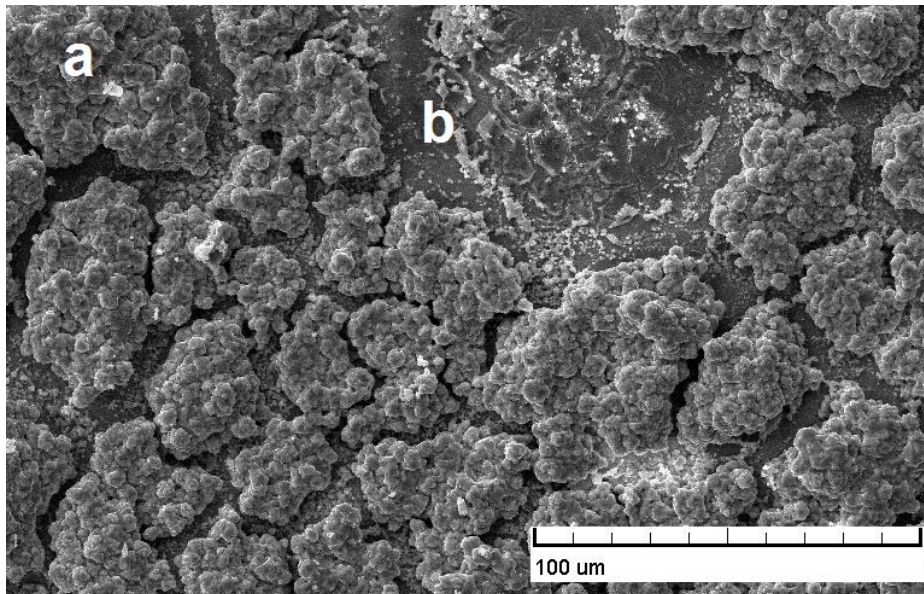


Figure 3. 6 SEM micrograph of a CZTS sample grown at 580 °C. (a) is an area referred to as “CZTS island” which is chlorine free according to EDX measurement, whereas (b) is an area where the presence of chlorine atoms was detected.

In Figure 3. 7 the SEM micrographs of samples annealed at different temperatures are shown. As expected, the material grown at the highest temperature shows the biggest grains. A similar study was carried out already, starting from a similar liquid formulation, using Cu and Zn acetates and Sn (II) chloride in place of our nitrates and Sn (IV) chloride, but bigger dimensions were detected in that case [73].

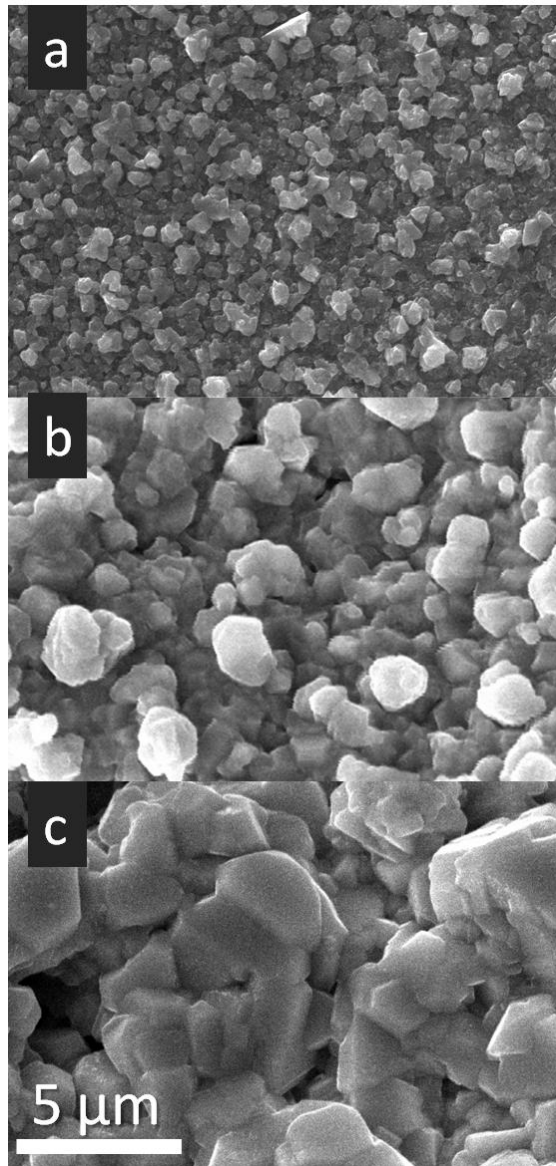


Figure 3. 7 CZTS grown at three temperatures: (a) 500 °C, (b) 550 °C and (c) 580 °C.

Raman spectra collected on the “CZTS islands” have shown that CZTS is the predominant phase in the film (Figure 3. 8) [74].

By sampling random areas of the layers, spectra such as the one in Figure 3. 9 were collected. Beside the CZTS peaks, they showed intense signals (highlighted with the question marks) that could not be assigned to the CZTS phase nor any of the secondary or ternary phases studied in the literature, thus, we supposed that they could be related to something underneath the absorber layer , for instance, molybdenum sulfide.

To verify that hypothesis, a Mo thin film was sulfurized using the same setup as the one adopted to grow CZTS at 500 °C. In Figure 3. 10 the Raman spectrum of the resulting MoS_x layer is shown, and confirms the hypothesis reported above.

Thus, quick Raman experiments on random areas of the absorbers can give information about the presence of microscopic fractures in the sulfurized film, without analysing the film with any additional microscopy technique.

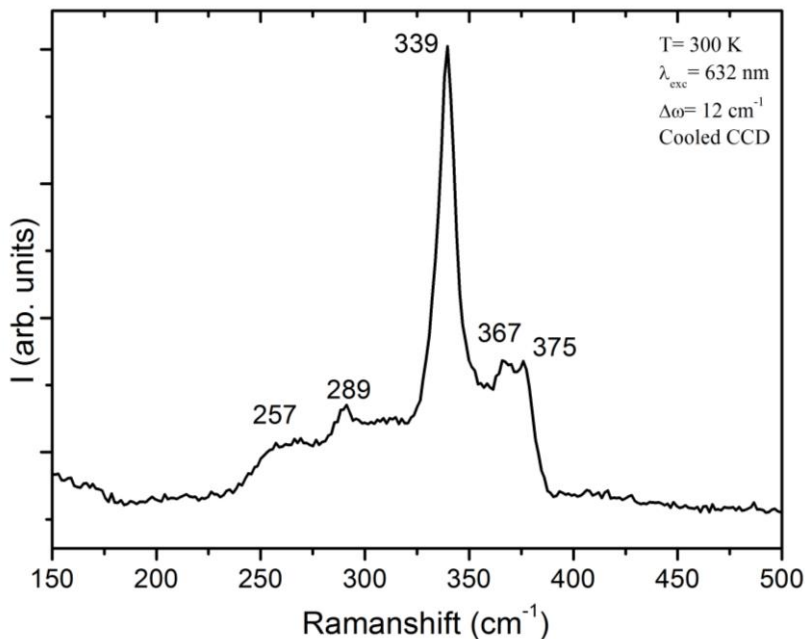


Figure 3. 8 Raman spectrum of a typical “CZTS island”. Only the CZTS signals are present.

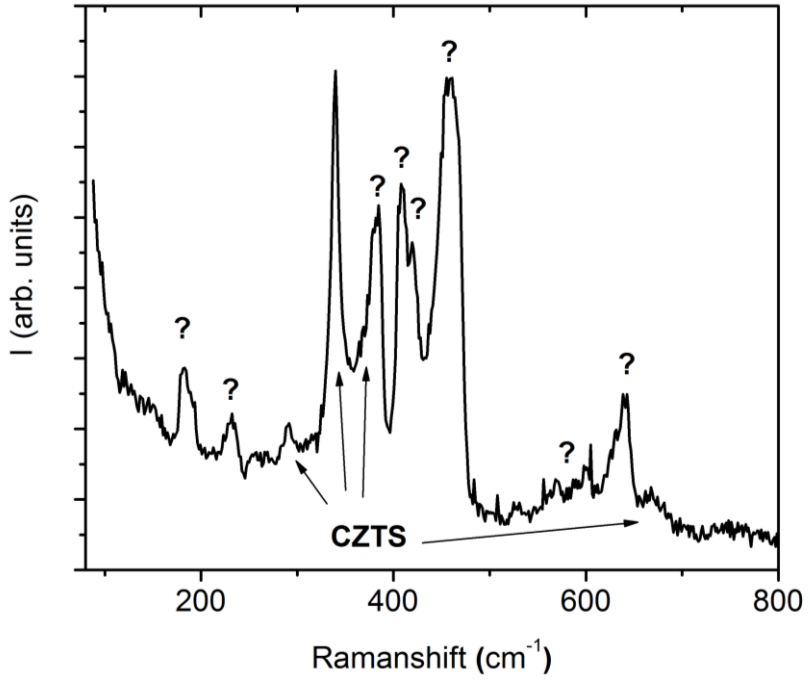


Figure 3. 9 Raman spectrum of a random spot of a CZTS layer.

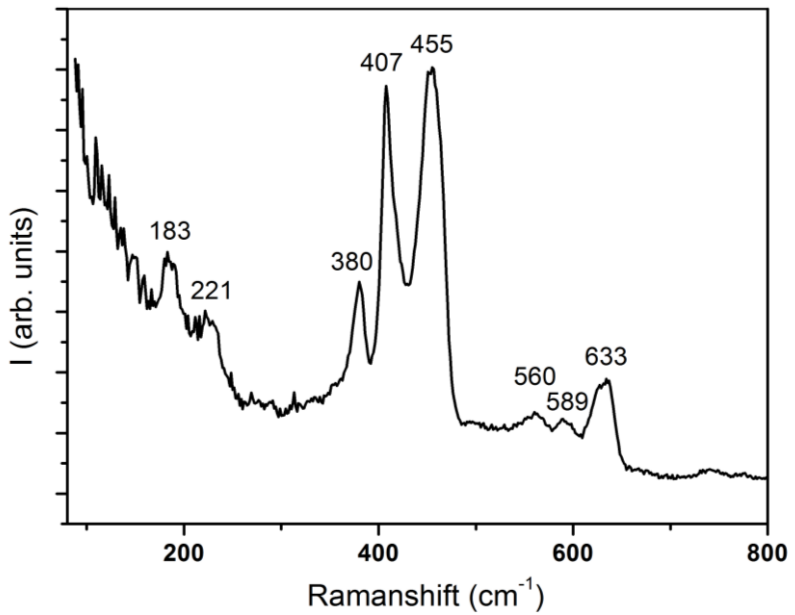


Figure 3. 10 Raman spectrum of a molybdenum layer sulfurized at 500 °C.

Another piece of information that can be obtained from Raman spectra is the presence of amorphous carbon. In some spots of the samples analyzed, the Raman spectra showed a wide band at least as intense as the main mode of CZTS (located at 337-339 cm^{-1}) in the spectral range between 1000 and 1800 cm^{-1} as shown in Figure 3. 11. The group of Professor Wan [75] reported a similar spectrum and they demonstrated that the carbon can be completely eliminated by means of a particular in vacuum etching we didn't have access to [76]. In the attempt of getting rid of carbon by carrying out different annealings on the samples in air, the molybdenum layer underneath the absorber resulted totally delaminated, probably because of the formation of HCl which etches the metal quite efficiently.

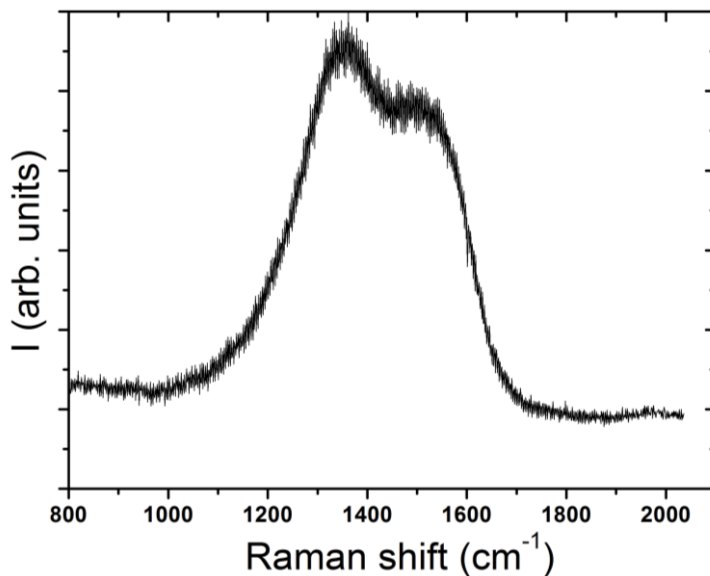


Figure 3. 11 Raman spectrum of a CZTS layer in the region between 800-2100 cm^{-1} . No CZTS signals are expected in this region, but the double band can be inferred to the presence of amorphous carbon.

Many of the features that characterize samples grown with this method, such as cracks in the film, presence of carbon and chlorine heavily affect the quality of the CZTS layer, not to mention the very low reproducibility; thus none of the samples shown were good candidates for the building of functioning devices. As a matter of fact, the best solar cell (obtained by means of “MIB Solar finalization” procedure – see Chapter 2) gave an efficiency of 0.17%. The J-V curve and the EQE are depicted in Figure 3. 12 and 3. 13 respectively. However, by means of the latter

measurement it was possible to extract the bandgap of the material, which was 1.52 eV in agreement with the composition of the absorber layer.

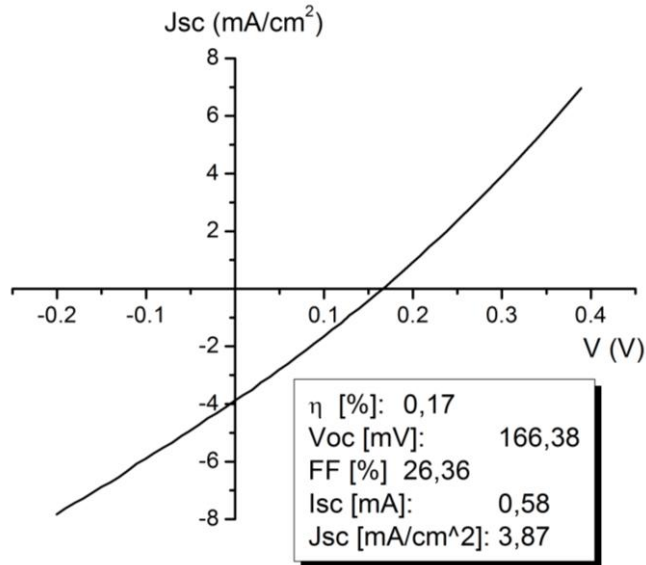


Figure 3. 12 J-V characteristic of the best solar cell produced by the sol-gel method.

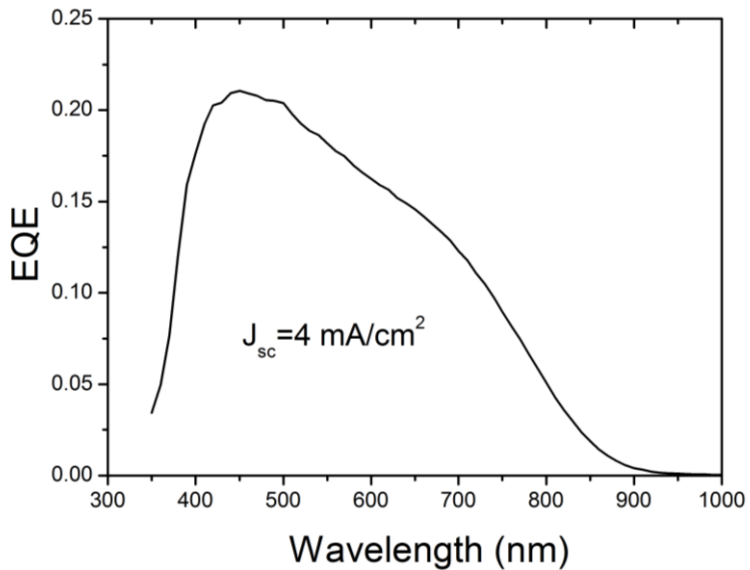


Figure 3. 13 EQE of the best solar cell produced by the sol-gel method. The short circuit current density was obtained from the integration of the curve.

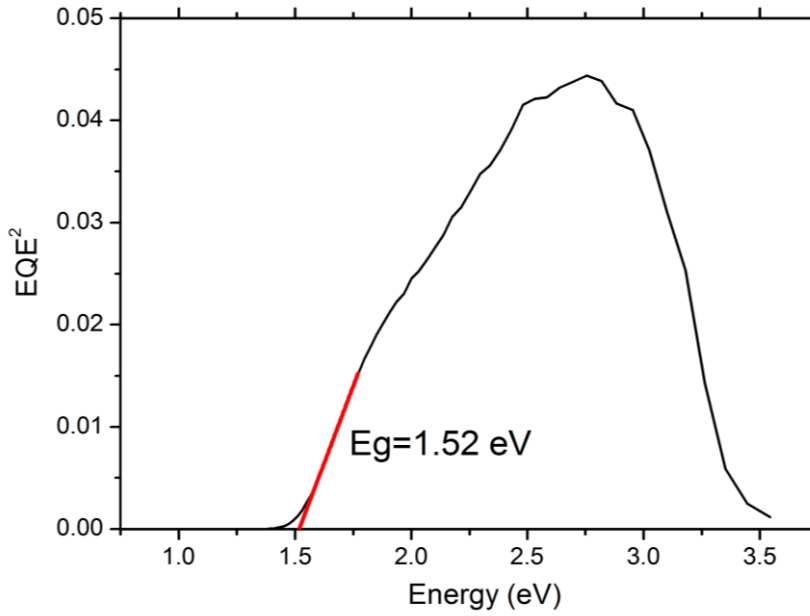


Figure 3. 14 Band gap estimation obtained from the EQE curve of the best device.

3. 2 Thiourea containing suspension

The aim of this study is manifold:

- evaluate the possibility of growing CZTS at low temperatures;
- develop a “one pot” fabrication route for CZTS, that is based on a single liquid formulation which contains all the elemental sources.

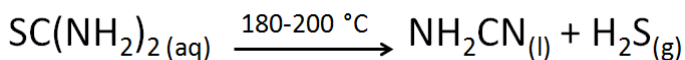
3. 2. 1 Formulation and deposition of the liquid suspension

The initial suspension is obtained by preparing first a solution of zinc acetate, copper (II) acetate and tin (II) chloride dissolved in methanol at room temperature in air. When everything is dissolved, the solution is colourless. CH₃OH is periodically added to the solution in order to compensate for its evaporation. When thiourea is added, the colourless solution turns into a white suspension ready to be deposited. To avoid any precipitations the suspension must be kept under vigorous stirring. The concentrations of reagents are listed in Table 3. 3. The molar ratios of metals Cu, Zn and Sn is kept 2:1:1, while thiourea is in excess (five times Cu moles). Thiourea acts as a complexing agent, stabilizing the (I) oxidation state for Cu in solution [77] and supplies S atoms.

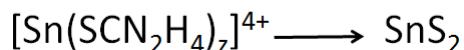
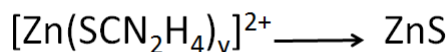
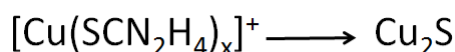
| | Concentration (mol/l) |
|---|--------------------------|
| (CH ₃ COO) ₂ Cu · H ₂ O | 0.05 |
| (CH ₃ COO) ₂ Zn · 2H ₂ O | 0.025 |
| SnCl ₂ · 2H ₂ O | 0.025 |
| H ₂ NCSNH ₂ | 0.25 |

Table 3. 3 Composition of the suspension used to produce CZTS. Solvent: CH₃OH.

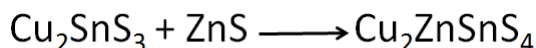
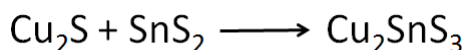
The suspension is deposited at room temperature on Mo-coated SLG either by dip-coating or drop-casting, according to the specifications given in Chapter 2. After the deposition, the layers undergo a drying on a hot plate at 60 °C and a soft pre-annealing in air at 200 °C. At this stage thiourea decomposes [78], according to the reaction:



and the film brownishes. Herein, hydrogen sulfide acts as sulfur source, thus the conversion of methanolic thiourea-metal complexes into the corresponding sulfides upon heating is expected:



At higher temperatures, the following solid state reactions are promoted [79]:



The identification of the temperature at which the solid state reaction between the ternary phase Cu_2SnS_3 (CTS) and ZnS occurs is the objective of the analysis presented in the next paragraph.

3. 2. 2 Identification of the crystallization temperature

Some examples of formation of CZTS at relatively low temperatures such as 200 °C or 300 °C are reported [80, 81, 82], but none of the featured films were tested in a solar cell. Moreover, in many cases, the formation of the desired phase is allegedly confirmed by XRD, which is not a reliable characterization technique for kesterite, since unreacted CTS and ZnS have the same structural motif of CZTS (see Figure 3. 15).

Herein, Raman spectroscopy is a useful tool to understand whether the CZTS phase is fully formed, that is when its main vibrational modes are clearly visible. Thus we used this technique has been used to monitor the phase formation.

In Figure 3. 16 stacked Raman spectra of samples deposited by dip-coating (10 layers) treated at different temperatures for 4 hours in a tubular oven under Ar flux are presented.

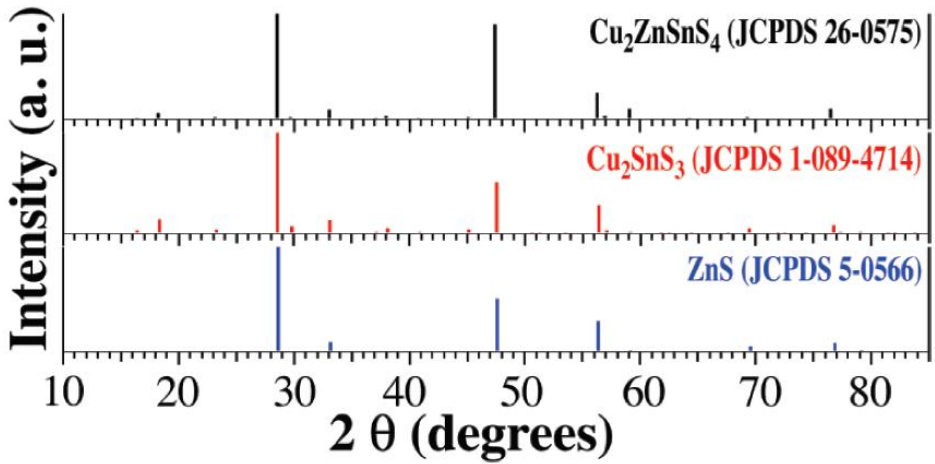


Figure 3. 15 Simulated XRD powder patterns of CZTS, CTS and ZnS according to The International Centre for Diffraction Data (www.icdd.com).

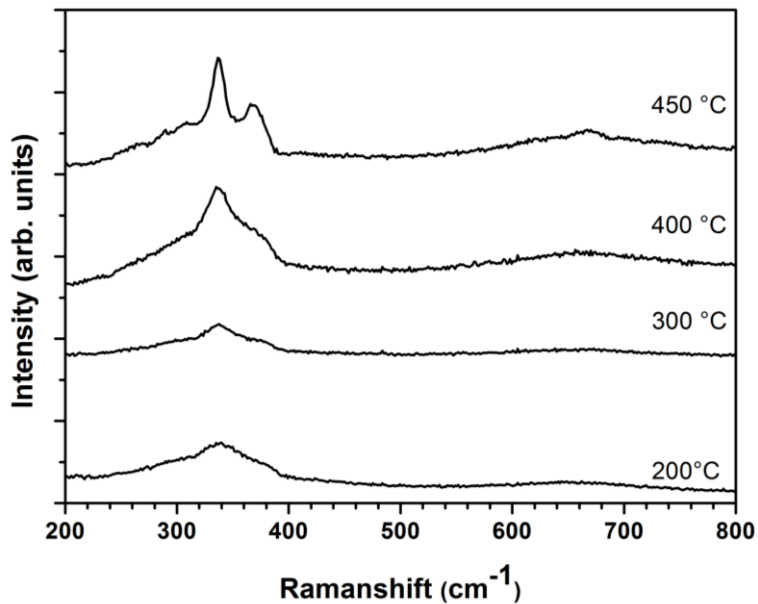


Figure 3. 16 Raman spectra of the films grown at 200 °C, 300 °C, 400 °C and 450 °C for 4h hours. Intensities have been normalised over layer thicknesses.

It is quite apparent that 200 °C is not sufficient for the CZTS crystalline phase to form, at least with this growth method. At higher temperatures the vibrational spectra are more defined but we can assert that at temperatures below 450 °C the film is composed of sulfides, either

amorphous or nanocrystalline. In Figure 3. 17, a zoomed view of the Raman spectrum of the sample grown at 450 °C shows all the main vibrational modes of CZTS at 267, 288, 338 and 368 cm^{-1} . Thus this is the minimum temperature at which the phase forms. The Raman spectrum also shows a peak which is usually assigned to the cubic Cu_2SnS_3 phase [74, 83]. Recently, a thorough Raman study of device grade polycrystalline CZTS by Dimitrievska et al. reported that the signal could pertain a third A-symmetry mode from the CZTS kesterite phase, that is highlighted with the excitation wavelength used in this work [84]. This vibrational feature is supported by theoretical calculations as well [85].

To conclude, according to Raman measurements, at 450 °C CZTS is the main phase composing the film, but the presence of the ternary CTS cannot be excluded, if only one excitation wavelength is available to analyze the film.

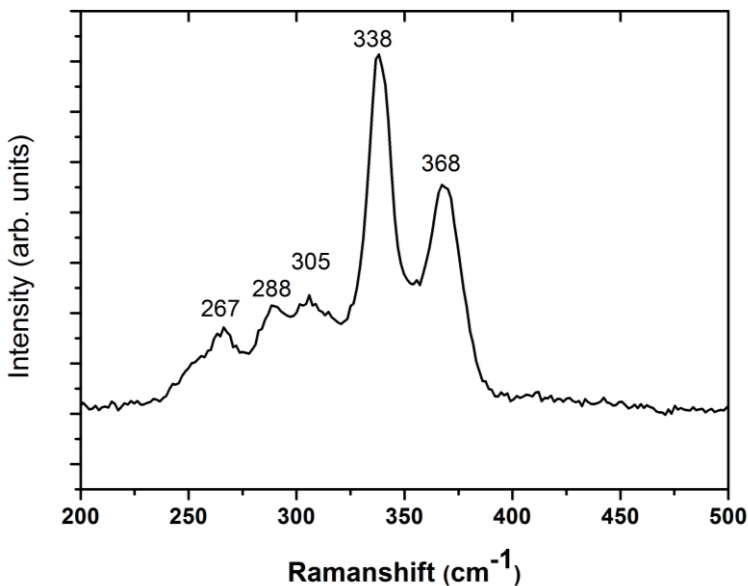


Figure 3. 17 Zoomed Raman spectrum of the sample grown at 450 °C for 4 h in Ar atmosphere. Peaks highlighted belong to the CZTS crystalline phase.

3. 2. 3 Crack formation issue and optimization of the method

One problem usually encountered during the design of a new chemical method is the presence of cracks in the film, which hamper their utilization as absorbers in solar cells, because they contact the front and back electrodes, namely the TCO and the Mo layers. Samples produced by the method described in the previous paragraph were characterized by the presence of crack-free areas but also many damaged regions as can be seen in Figure 3. 18.

This paragraph concerns the optimization of some of the parameter of the growth process in order to minimize the dimension of cracks in the film. Sacrificial samples made to test the effectiveness of the modified parameters were deposited by drop-casting, which is the least laborious deposition method available. The volume of suspension deposited was dispensed by a micropipette upon an area of around 2 cm². The appearance of typical CZTS samples grown by this method is pictured in Figure 3. 19.

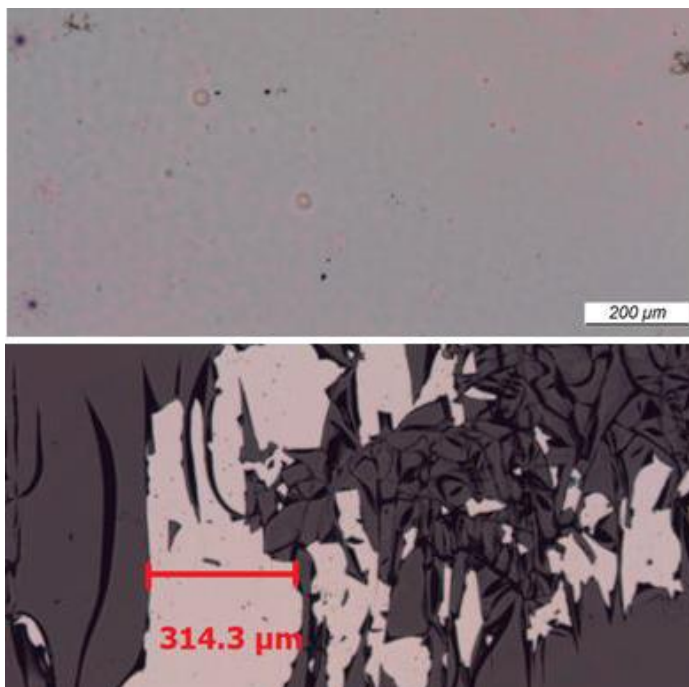


Figure 3. 18 Images of CZTS layers collected with the optical microscope: (up) well covered region, (bottom) damaged region.



Figure 3. 19 Pictures of samples deposited on glass (left) and on Mo-coated glass (right) by dip-coating. The deposited area is 1.5x2 mm.

Solvent mix

Since methanol is extremely volatile (b.p. = 65 °C), its fast evaporation can lead to an uneven coverage of the surface that has to be coated with the suspension. In order to improve the coating of the molybdenum, another solvent option needs to be formulated.

Ethylene glycol is the solvent tested for this work: it has a high boiling point (197 °C), a relative polarity similar to CH₃OH (thus assuring the dissolution of the reagents composing our formulation) and a high viscosity (16.1 cP); these features make this solvent a suitable candidate for this liquid-based deposition.

A preliminary study was done by using pure HOCH₂CH₂OH in place of CH₃OH. The CZTS produced by annealing the precursor layers at 450 °C detached from the molybdenum, thus we decided to add different amounts of HOCH₂CH₂OH to CH₃OH (10%, 20% and 30% v/v%) in order to define the solvent mixture which gave a better coverage of the molybdenum layer. For each sample, the most homogenous areas investigated by optical microscopy are shown in Figure 3. 20. The layer produced with 30% HOCH₂CH₂OH have many 10-20 μm wide cracks (shining parts of the picture c), while the layer produced with 20% HOCH₂CH₂OH has no uncovered areas, but it's characterized by narrow cracks affecting the entire sample (dark lines in picture b). It can be easily deduced that the best solvent mix among the three is the one containing 10% HOCH₂CH₂OH and 90% CH₃OH. Thus, the new liquid formulation comprehends the addition of HOCH₂CH₂OH.

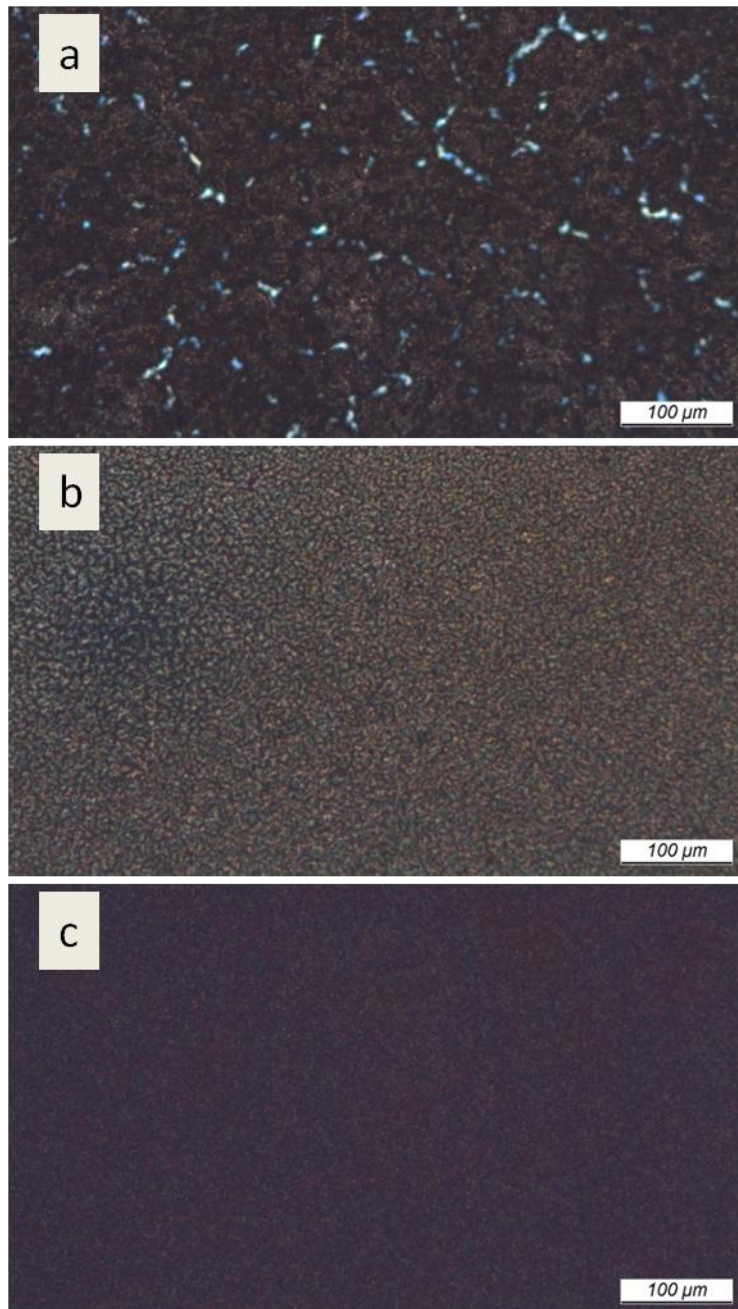


Figure 3. 20 Images collected with the optical microscope of layers annealed at 450 °C produced from a suspension containing: (a) 30%, (b) 20%, (c) 10% v/v % of ethylene glycol.

Identification of the critical temperature of cracks formation

Beside on the rheology of the liquid formulation, thermal treatments play a crucial role in the macrostructure of the absorber layer. Temperature accelerates evaporation of volatile matter, promotes thermolysis and condensation reactions that might stress the film while it is forming. Therefore, it is important to define the temperature at which the film starts to crack.

We hypothesize that cracks that are visible in the absorber layer might be generated during thermal treatment at low temperatures in air.

In order to identify the temperature at which cracks start to form, some samples were placed on a hot plate immediately after the deposition and heated from room temperature up to different temperatures for 10 minutes. The resulting layers were observed at the optical microscope. The most relevant steps are pictured in Figure 3. 21. At 45 °C, as methanol quickly evaporates, some precipitates emerge from the film. There is no particular change of morphology up to 100 °C, where a flattening of the surface is observed. At 140 °C some rounded holes can be seen in random areas of the surface. It looks like at 170 °C the cracks arise from the same holes observed in the previous stage. At 450 °C the film results completely damaged, featuring very little crack-free areas.

Thus, the critical range of temperatures at which the film starts to crack is around 140 °C. At these temperatures the dehydration of the acetates is expected [86], before the thermolysis of thiourea.

As a consequence of this study, a new programmed annealing routine has been designed, in order to favour the decomposition reactions that convert the liquid suspension into a film with the least number of fractures. A slow ramp has been thought during the heating up of the sample up to 200 °C, and slow cooling was adopted as well.

For what concerns the annealing at high temperature under Ar flux, no differences in compactness or morphology was observed between samples heated up at different rates, thus the fastest way allowed by our equipment was chosen. After the annealing samples were left to cool down naturally in the oven. The resulting temperature ramps used to produce CZTS from now on is depicted in Figure 3. 22.

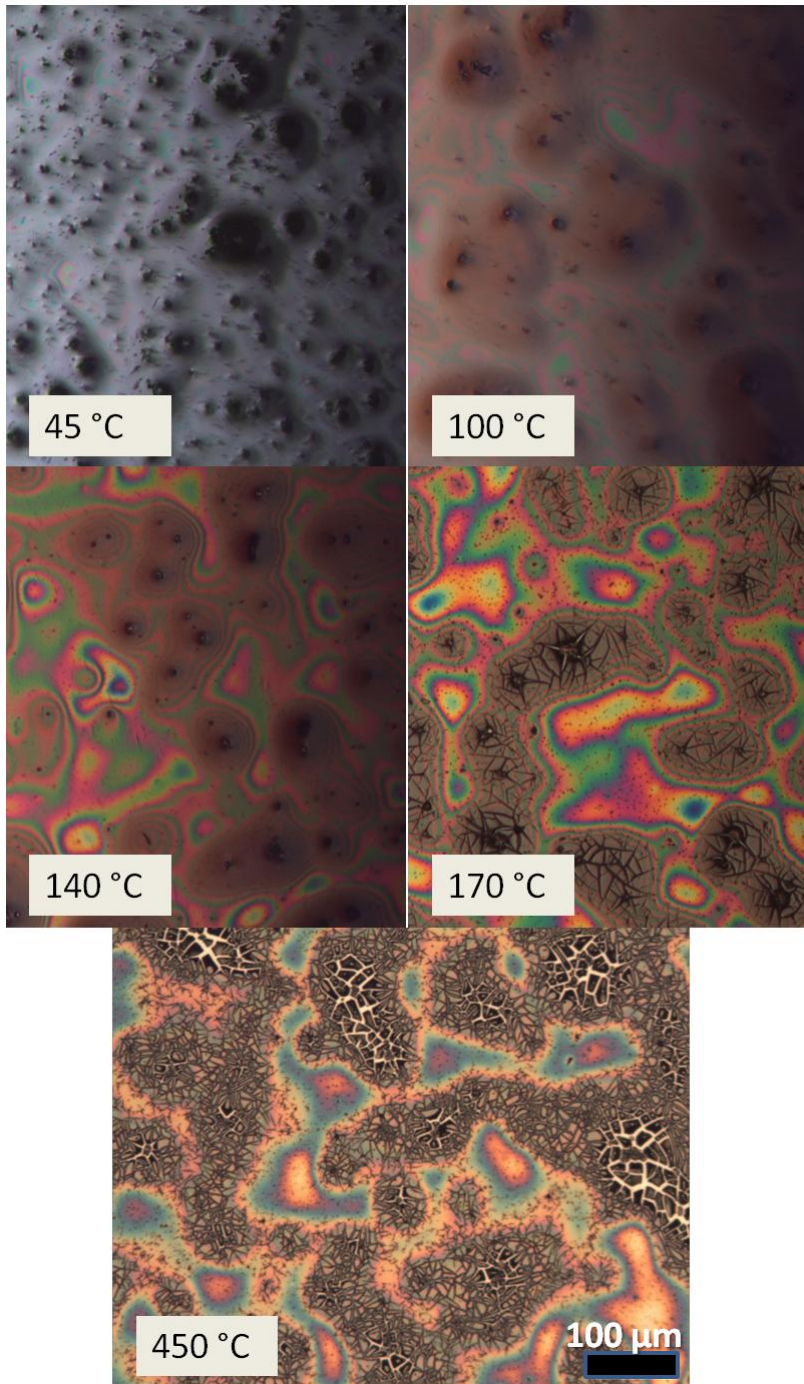


Figure 3. 21 Images collected with the optical microscope. Surfaces of precursor layers treated in air at different temperatures and (bottom) layer after the annealing at 450 °C under inert conditions.

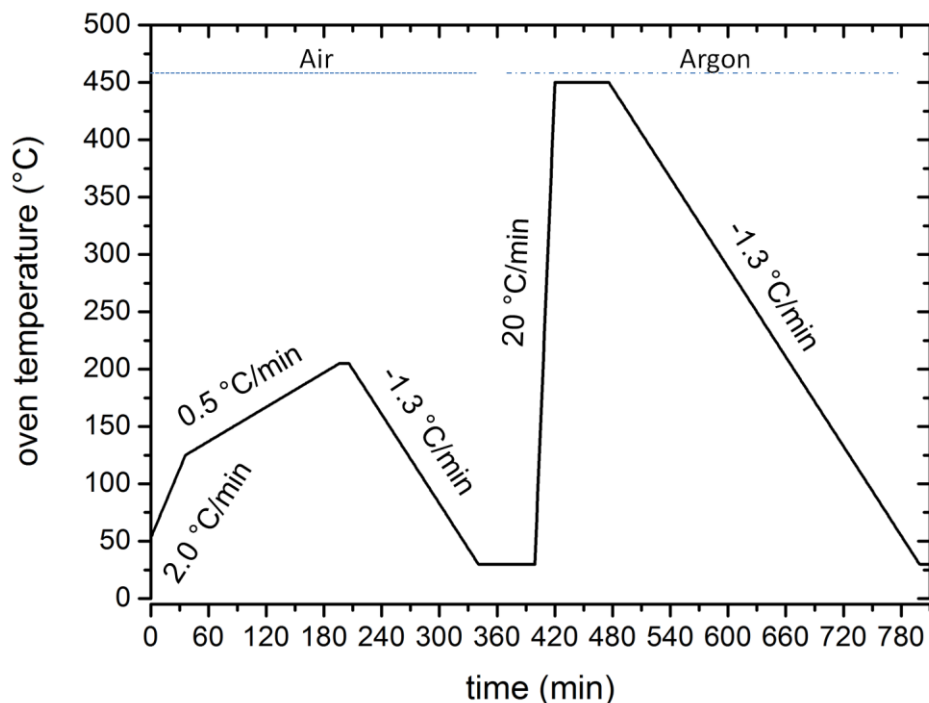
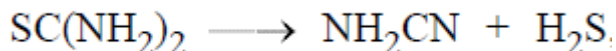
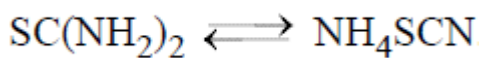


Figure 3. 22 Temperature profile of the optimized annealing routine.

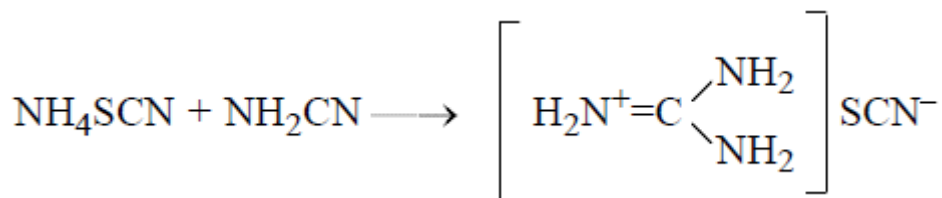
3. 2. 4 Characterization of precursor and absorber layer

After the slow annealing in air at 200 °C, the precursor layer is a dense film, as can be seen from the cross section SEM image in Figure 3. 23. No crystallites can be observed and the presence of organic species is still predominant at this stage.

The reflectance IR spectra of the precursor layer after the thermal treatment at 200 °C in air and after the annealing in inert atmosphere at 450 °C are depicted in Figure 3. 24. IR spectra collected after the layer was treated at higher temperature were very similar to the one reported. The majority of signals concerns vibrational modes related to nitrogen containing moieties. According to a study by Nurakhmedov et al. regarding the thermal analysis of thiourea, around 200 °C the isomerization of thiourea into ammonium thiocyanate occurs simultaneously with the decomposition into cyanamide and hydrogen sulfide [78]:



And the reaction between the isomer and cyanamide gives guanidium thiocyanate



an organic salt that decomposes in liquid state giving solid cyclic compounds such as substituted melamine in the range 220-300 °C [87,88]. These compounds have a high boiling point and might remain embedded in the film preventing the crystalline CZTS to form below 450 °C.

Therefore the vibrational modes observed in the IR spectrum might be related to these type of compounds.

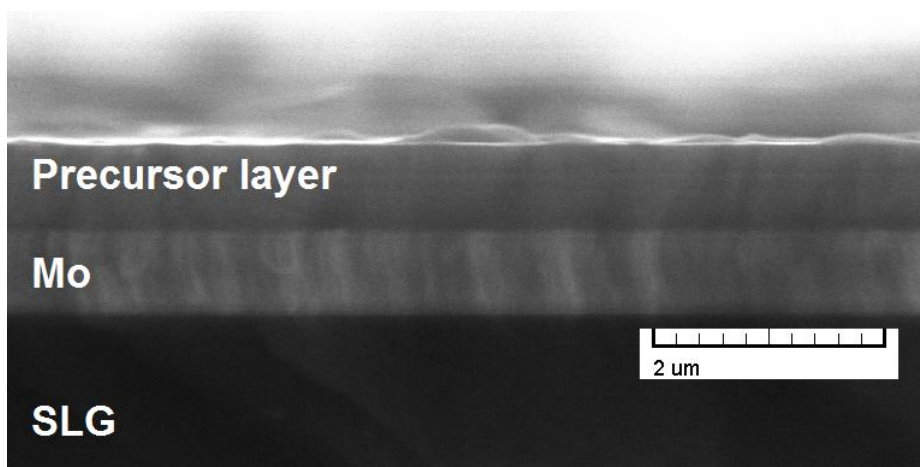


Figure 3. 23 SEM Cross-sectional view of the precursor layer deposited via thiourea metal complexes.

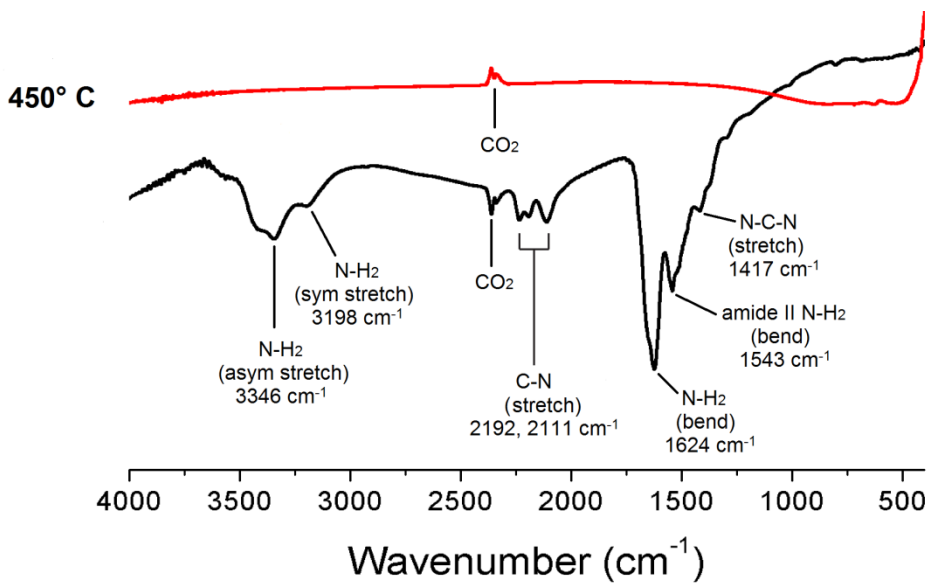


Figure 3. 24 FTIR spectra of CZTS film before and after thermal annealing. After thermal annealing, all organic traces in the films had been removed.

The layer crystallized after the thermal treatment at 450 °C appears as composed of crystallites much smaller than the ones grown with the method described in section 3.1 (see Figures 3. 25 and 3. 26), probably because of the lower temperature employed.

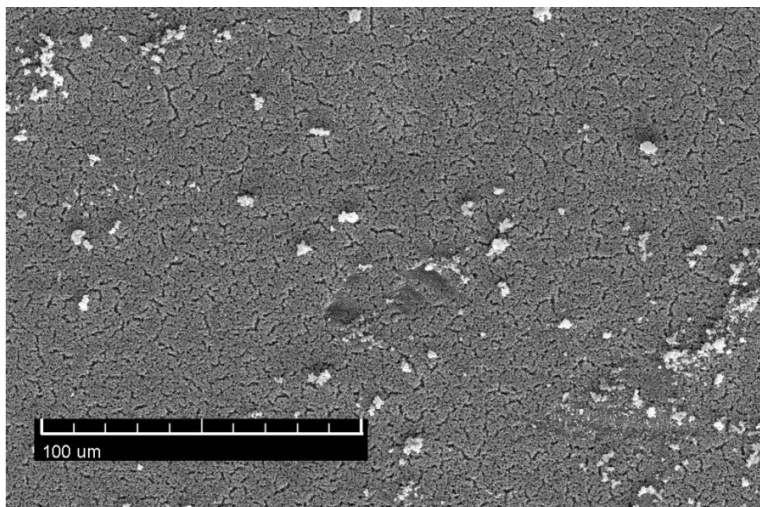


Figure 3. 25 Top view SEM (low magnification) micrograph of a sample of CZTS grown at 450 °C by means of the optimized recipe and annealings.

The material doesn't feature any crack visible at the optical microscope, but still the microstructure is not suitable for the fabrication of functioning solar cells as it shows an overall open structure.

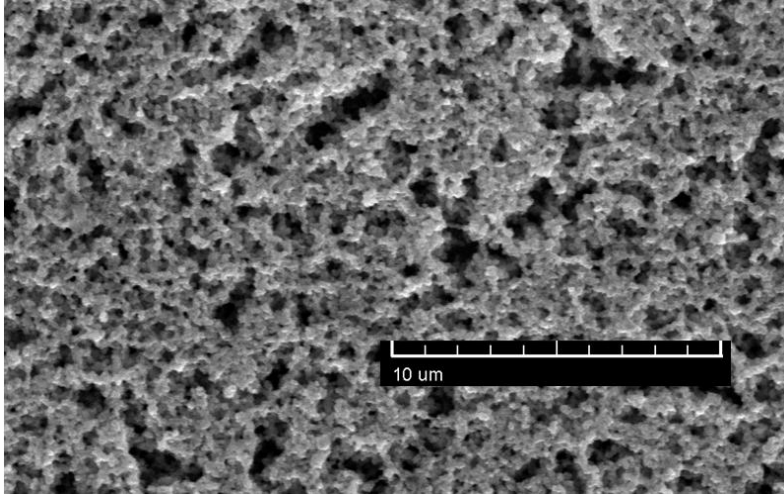


Figure 3. 26 Top view SEM micrograph of a sample of CZTS grown at 450 °C by means of the optimized recipe and annealings.

3. 2. 5 Effect of stoichiometric concentration of thiourea in the suspension

According to a study carried out by Seo and Lim [89], denser layers of CZTS can be produced by diminishing the quantity of thiourea in a sol-gel formulation, from a big excess to almost the stoichiometric amount. The reasons why high thiourea concentrations are usually employed for the fabrication of metal sulfides are more than one. First of all thiourea is an effective complexing agent for heavy metals that helps their solubilisation. Secondly, it decomposes into hydrogen sulfide, a gas that might escape from the precursor film that is forming before reacting with the metals, at least in the annealing setup available for this work. Eventually, an excess of sulfide anions in the reaction environment should prevent the oxidation of metals which is a favoured reaction at the temperatures employed in air.

However, we decided to reproduce the same experiment by depositing a suspension that contained 0.11 mol/l of thiourea instead of 0.25 mol/l, which was the concentration adopted so far. The molar ratios

Cu:Zn:Sn:S tested is much closer to 2:1:1:4, whereas with the previous recipe used in this work the ratios were 2:1:1:10.

What we could observe was a not fully grown CZTS layer, as the one depicted in Figure 3. 27 and in many regions of the film the crystalline CZTS phase was not even formed, as shown in the inset Raman spectrum. Therefore, for the next experiments regarding the addition of an organic binder in order to improve the microstructure of the film, we adopted the sulfurization setup already used to produce CZTS layers in section 3.1.1. In this manner we assure that enough sulfur reacts with the film to produce CZTS without relying on the decomposition of thiourea.

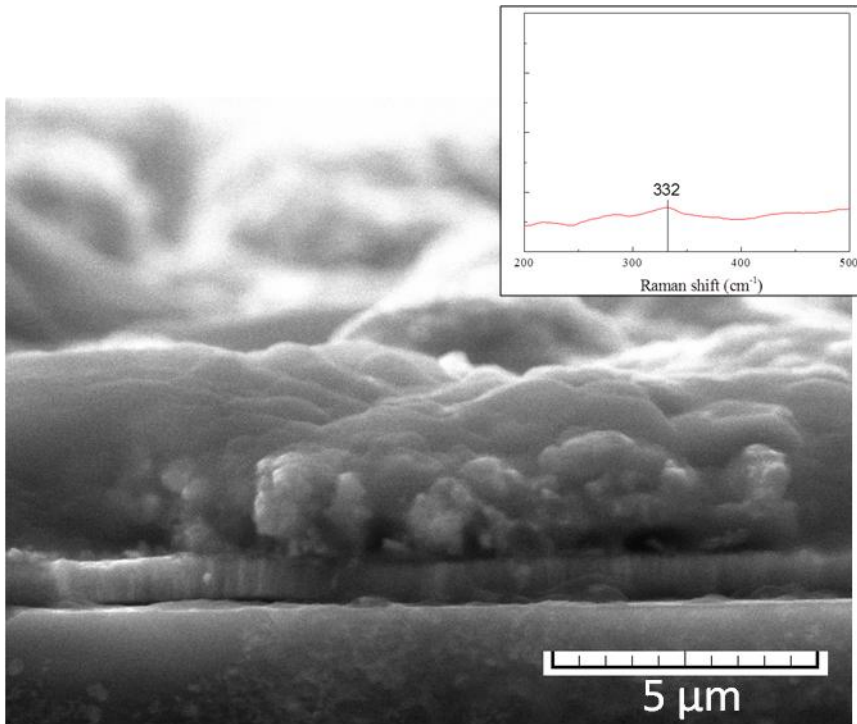



Figure 3. 27 SEM cross-section view of a layer grown with a stoichiometric amount of thiourea in the suspension. Inset: Raman spectrum of a random area of the same layer showing no CZTS was formed.

3. 2. 6 Effects of polyvinyl alcohol on films grown via thiourea complexes plus sulfurization. A preliminary study.

Commercially available polyvinyl alcohol (PVA, sometimes referred to as PVOH) has been used in diverse chemistries to improve filming of different materials. This preliminary study aims at evaluate the use of PVA as an additive to the liquid formulation that produced the most compact CZTS to improve film formation. Different amounts of an aqueous solution of PVA (3% wt% obtained by dissolving Mowiol® in bidistilled water) were added to the suspension and CZTS layers produced after the annealing at 450 °C in sulfur vapors were inspected by SEM. Additionally, the Raman spectra of the layers were collected in order to understand whether the addition of the organic binder could interfere with the formation of the desired crystalline phase. The concentration of PVA in the liquid formulations are reported in Table 3. 4.



| | PVA concentration (wt%) |
|----------|-------------------------|
| Sample A | 0.60% |
| Sample B | 0.80% |
| Sample C | 1.00% |
| Sample D | 1.10% |

Table 3. 4 Concentration of PVA (wt%) in samples grown from liquid formulations.

The addition of PVA led to a better film in terms of compactness. As an example, a low magnification top view of sample A, the one with the lowest concentration of the organic binder, is shown in Figure 3. 28. No open structure is observed in any of the other sample.

SEM micrographs collected for samples grown with a slightly different concentration of PVA showed completely different morphologies one from another, as can be seen from Figure 3. 29. None of them resembles either the angular shaped morphologies already observed for previous samples, except for sample B and all of them featured some kind of precipitate on the surface, either copper or tin rich.

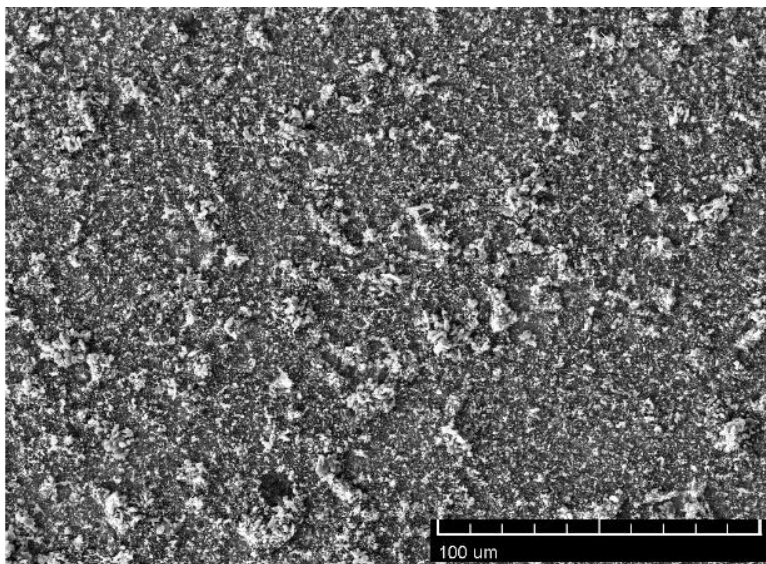


Figure 3. 28 Top view SEM micrograph of a CZTS sample A, grown starting from a suspension containing 0.60% PVA.

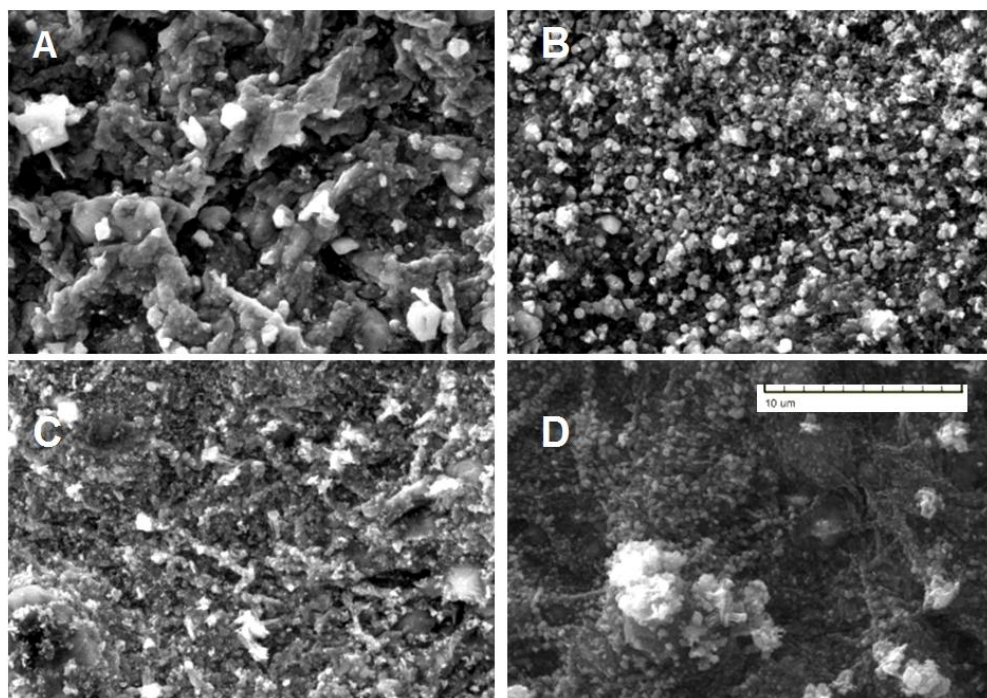


Figure 3. 29 SEM top view of CZTS samples with different amounts of PVA in the liquid formulation. (A) 0.60 wt%, (B) 0.80% wt%, (C) 1.00 wt%, (D) 1.10 wt%. Marker = 10 μm

Raman spectra collected, as shown in Figure 3. 30, confirmed the formation of the desired phase, but the amount of PVA was found to heavily influence the composition of the surface of the CZTS layer (the estimated penetration depth of the 632 nm laser is around a few hundred nanometers). As a matter of fact, in every sample an unassigned peak at 324 cm^{-1} was found, and in some spots protruding from the surface, the main vibrational modes of Cu_2S and SnS_2 can be recognized [90,91] for samples that were grown with the minimum and maximum amount of PVA, respectively.

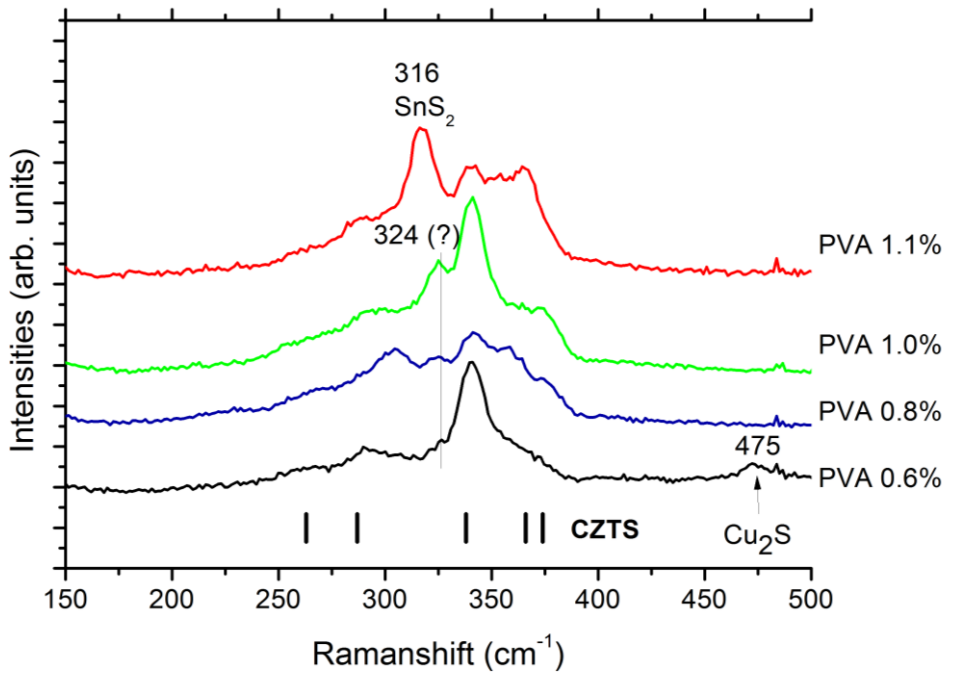


Figure 3. 30 Raman spectra of samples grown with a different amount of PVA in the thiourea containing suspension.

A more detailed investigation of the superficial and bulk compositions of each sample has to be carried out, but from this preliminary study it is apparent that the amount of PVA probably needs to be further reduced, in order to improve the film compactness without favouring the formation (or segregation) of the secondary phases detected by this brief study.

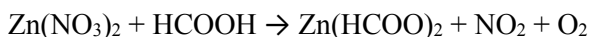
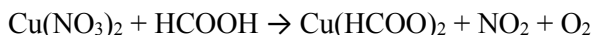
Chapter 4

CZTSe thin film fabrication: concentrated ink containing formate ions

The formation of metallic particles by means of the thermal decomposition of the respective formates has been already proven for heavy metals such as cobalt, nickel and copper [92]. With a proper deposition method one can take advantage of this feature to produce metallic films as well. In this regard, a paper has recently described [93] the chemical pathway from copper, indium and gallium formates, to carbon-free CIGS absorbing layers with a satisfying efficiencies (around 11%) once embedded in a device, and the aim of the work herein described points at evaluating a similar route for CZTSe thin film fabrication.

4.1 Formulation and deposition of the ink

Pure copper and zinc formates were obtained by making the respective (hydrated) nitrates react with an excess of formic acid in air. Since the reaction is quite exothermic and a dense brown gas is released after the dissolution of the aforementioned salts, the hypothetical chemical equations are the following:



The two powders are then kept at 140 °C for one hour to get rid of crystallization water and excess HCOOH (b.p. = 100 °C). Some attempts of obtaining tin formate starting from different Sn(II) and Sn(IV) compounds (chlorides, methoxide, oxalate) were made but their dissolution in formic acid is not as straightforward as for Cu²⁺ and Zn²⁺, thus anhydrous methoxide, Sn(OCH₃)₂, was chosen as the tin source. Every step from now on is conducted in a nitrogen filled glovebox. The “standard” formulation of the ink proceeds as follows: 122 mg of Cu(OOCH)₂ and 80 mg of Sn(OCH₃)₂ are mixed in a 3 ml vial and dissolved under vigorous stirring in 370 mg of 1,1,3,3-tetramethylguanidine (TMG). When the salts are dissolved the ink is dark green. 470 mg of CH₃OH and 80 mg of Zn(OOCH)₂ are added to the ink. The vial is kept on a hot plate set at 105 °C under stirring for some minutes. The solution is then filtered through PTFE syringe filters (with pore size 0.2 μm) and its appearance at this stage is shown in Figure 4. 1. After the deposition via blade coating, the layers are immediately sealed under vacuum or put directly in the selenization process (see section 2.2 - CZTSe).

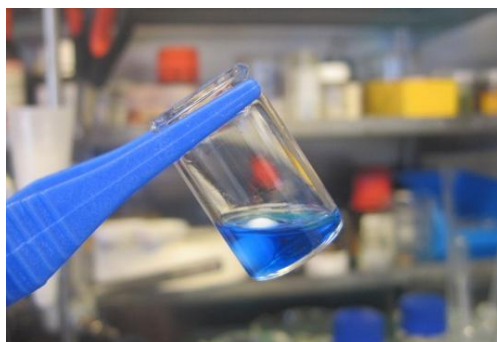


Figure 4. 1 Vial containing the ink used to deposit the three metals.

In order to produce some sodium doped samples, another ink was formulated using some drops of an alcoholic NaCl solution (1.27 wt%) in place of pure CH₃OH. The resulting ink is called Na10. Within this batch, an ink with a bigger amount of Zn formate was produced, and it will be referred to as Na10ZnE. The amount of reagents and the chemical composition of each formulation are reported in Table 4. 1 and Table 4. 2 respectively.

| | std ink | Na10 | Na10ZnE |
|------------------------------------|------------------|------|---------|
| | Composition (mg) | | |
| Cu(HCOO) ₂ | 52.8 | 122 | 89.5 |
| Zn(HCOO) ₂ | 35.7 | 83 | 61.8 |
| Sn(OCH ₃) ₂ | 34.6 | 80 | 55.5 |
| TMG | 155 | 373 | 279 |
| CH ₃ OH | 179.5 | 403 | 280.7 |
| NaCl 1.27% solution | - | 372 | 268 |

Table 4. 1 Composition of the inks used to deposit the precursor layers.

| | std ink | Na10 | Na10ZnE |
|----------------------------|-------------|------|---------|
| | composition | | |
| $\frac{Cu}{Sn}$ | 1.80 | 1.79 | 1.90 |
| $\frac{Zn}{Sn}$ | 1.20 | 1.21 | 1.29 |
| $\frac{Cu}{Zn + Sn}$ | 0.82 | 0.81 | 0.83 |
| $\frac{TMG}{Cu + Zn + Sn}$ | 1.76 | 1.83 | 1.88 |
| $\frac{Na}{Cu}$ | 0.00 | 0.10 | 0.10 |

Table 4. 2 Composition of the inks used expressed as molar ratios (calculated from values shown in Table 4. 1)

4.2 Characterization of the precursor layer

At the SEM, after drying at 200 °C, the precursor layers look very similar, independently of the composition of the ink. Basically the layers look composed of aggregates of sub-micrometer particles embedded in an organic matrix as depicted in Figure 4. 2. On top of them, some rounded particles with a diameter of around 2 μm are present.

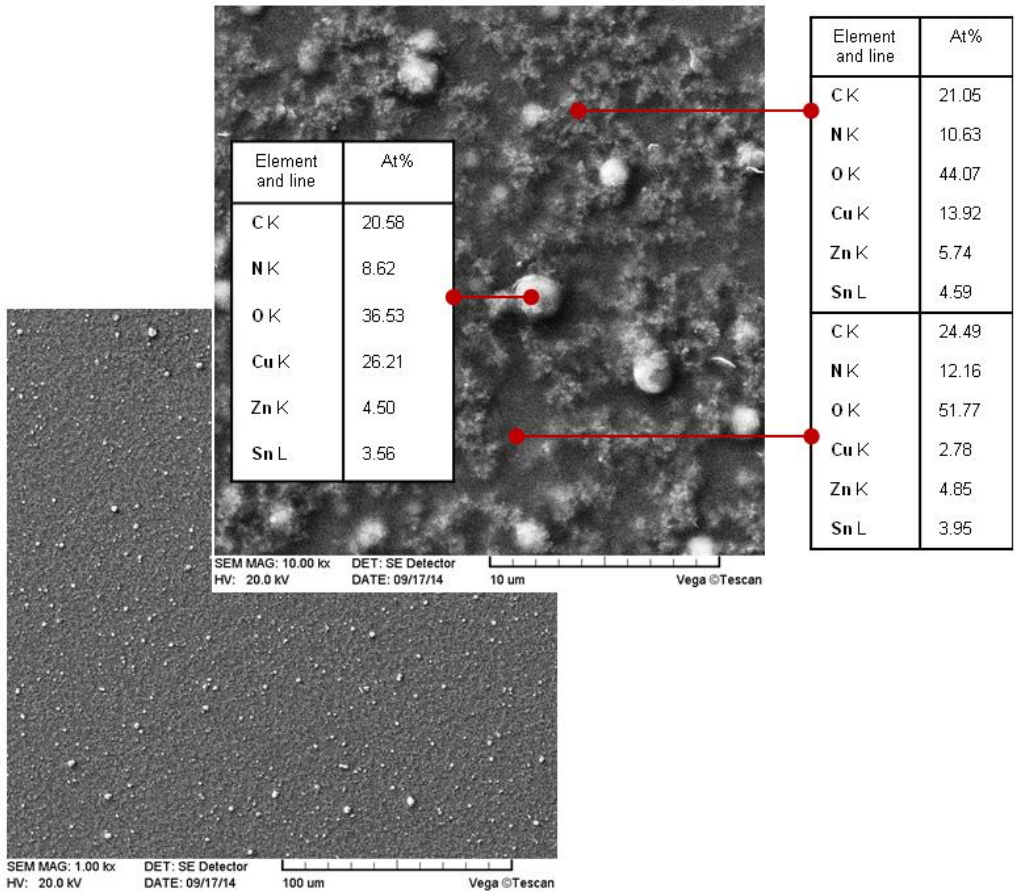


Figure 4. 2 Low and high magnification SEM top-view micrographs and composition of the three regions identified in a precursor layer. At% = normalized atomic percentages detected by EDX punctual analyses.

The elemental compositions measured by EDX were found to depend on the region investigated: the aggregates revealed the presence of the three metals, as well as a big percentage of carbon and oxygen atoms, while the shiny rounded particles were composed of mainly copper, carbon

and oxygen. It is quite apparent that copper is in excess both in those superficial rounded particles and in the aggregates, while the dark grey areas are characterized by a copper-deficient composition. The average Zn/Sn value in the sampled regions is 1.25 ± 0.04 , in agreement with the ink composition. According to these measurements, it is apparent that every region of the samples at this stage is still full of undesired atoms coming either from the solvents TMG (C and N), methanol (O) or the formate/methoxide (C,O) groups. A cross sectional view of the precursor layer is shown in Figure 4. 3. The thickness measured at the profilometer is around 700 nm, in agreement with what observed with SEM.

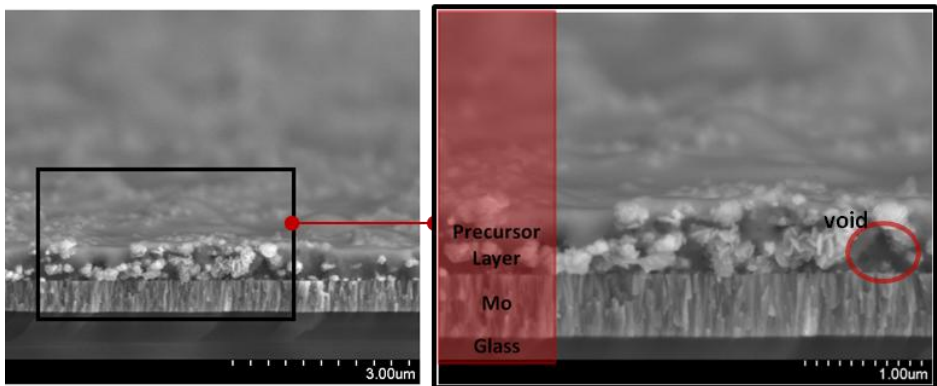


Figure 4. 3 Cross-sectional SEM micrographs of a precursor layer deposited on Mo coated SLG.

Alloying of the precursor layers by RTP

The XRD pattern of a precursor layer produced by depositing the “standard ink” on soda-lime glass was collected immediately after the treatment at 200 °C. The same sample was cut into four 1x1 inches samples that were treated at 300 °C, 350 °C, 400 °C and 450 °C for 10 minutes in a rapid thermal annealing system conditioned with 10 mbar of forming gas. Each of these samples was analyzed by means of XRD in order to investigate on the speciation of Cu, Sn and Zn at the temperatures considered.

As can be seen from the XRD pattern of Figure 4. 4, at 200 °C, metallic copper (Cu JCPDS: 00-004-0836) seems to be the main crystalline phase in the film, even though the presence of metallic zinc (Zn JCPDS: 04-

003-5661) cannot be excluded, since it shares with copper the main reflection located at around 43.3° . At 300°C two alloys of copper with zinc ($\text{Cu}_{0.7}\text{Zn}_{0.3}$ JCPDS: 03-065-9062 and $\text{Cu}_{0.75}\text{Zn}_{0.25}$ JCPDS: 04-004-6749) and one with tin ($\text{Cu}_{6.75}\text{Sn}_{2.25}$, JCPDS: 04-007-9969) are starting to form. The intensity of reflections pertaining the alloys get stronger up to 400°C , indicating an enhanced inter-diffusion between copper and the other two metals, while the reflection at around 43.3° , assigned to single Cu (or Zn), drops from 300°C to 350°C and grows again at 400°C , along with the formation of another Cu-Sn alloy ($\text{Cu}_{10}\text{Sn}_3$ JCPDS: 04-007-2013) and the disappearing of the signals assigned to the Cu-Zn alloys which formed at lower temperatures.

This overall trend suggests that the stronger reflection in the diffractogram collected after the treatment at 450°C might belong to another Cu-Zn alloy that couldn't be identified with the database used.

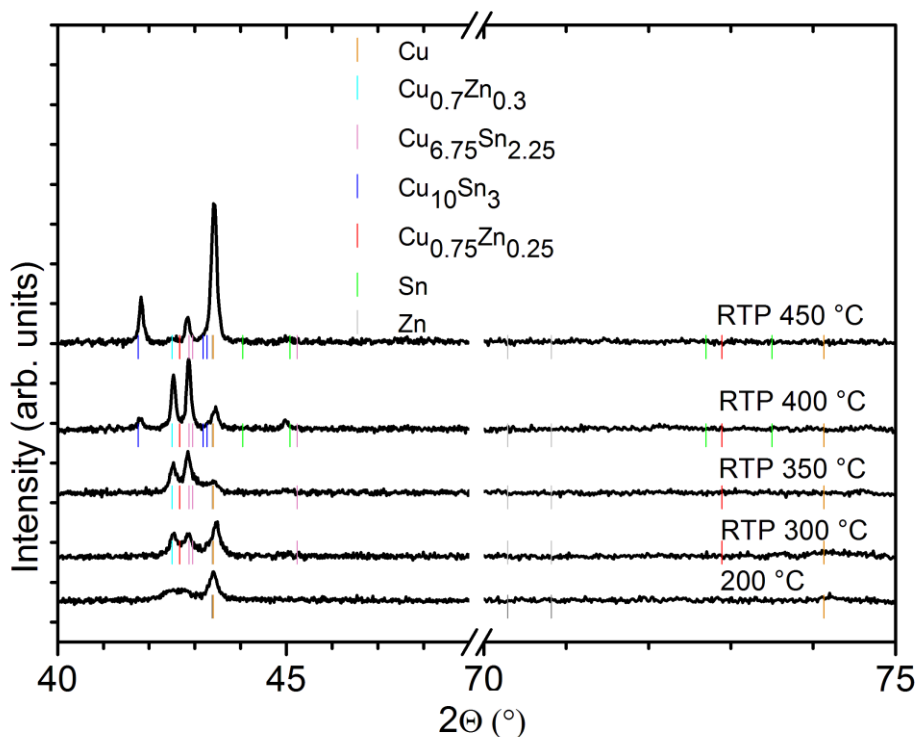


Figure 4. 4 XRD patterns of the precursor layer as-deposited (200°C) and treated at 4 temperatures in RTP. The colored bars indicate main peaks of the possible metallic crystalline phases matching with the experimental data. References JCPDS cards were

taken from the ICDD database: Cu 00-004-0836, Zn 04-003-5661, Sn 01-075-9188, $\text{Cu}_{0.7}\text{Zn}_{0.3}$ 03-065-9062, $\text{Cu}_{0.75}\text{Zn}_{0.25}$ 04-004-6749, $\text{Cu}_{6.75}\text{Sn}_{2.25}$ 04-007-9969, $\text{Cu}_{10}\text{Sn}_3$ 04-007-2013.

No further study of these samples was carried out, but a possible following could be the identification of the alloy combination (and thus pre-annealing temperature) that develops the best CZTSe microstructure.

4.3 Characterization of sodium free absorber layers and solar cells

Since the best CZTS solar cells in the literature have been produced with Cu-poor and Zn-rich absorber layers [94], we formulated the standard ink accordingly. As a result, different EDX point measurements at 7 kV on the brighter areas (as highlighted inside the oval in Figure 4. 5 on the left) showed a composition poor in Cu and Zn-rich, with ZnSe being the most probable undesired phase on the surface portion analyzed.

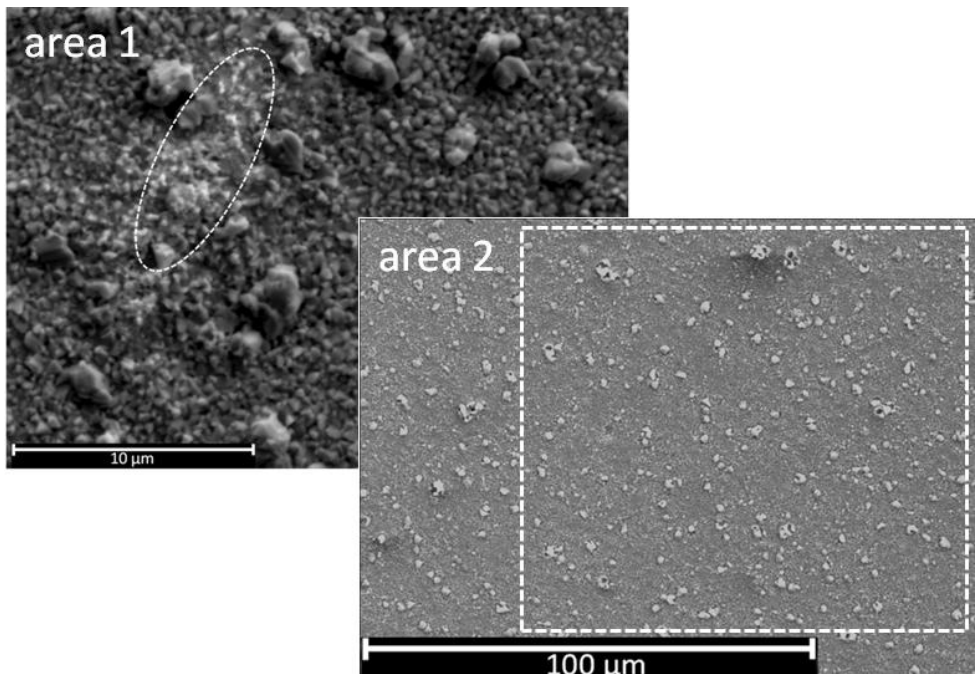


Figure 4. 5 SEM micrographs of a zinc-rich area (oval, picture on the left) and a generic wider area (square in picture on the right) analysed by EDX to determine the overall elemental composition of a sodium free absorber layer.

Beside these ZnSe “islands”, EDX measurements collected on different areas of the selenized films like the one highlighted by the square in Figure 4. 5 on the right, reveal a composition very close to Cu₂ZnSnSe₄ stoichiometry, which indicate a loss of zinc content compared to the amount introduced in the ink. The compositions of the two different areas analysed are listed in Table 4. 3.

| | Elemental composition expressed as ratios of atomic percentages | | |
|---|---|---|--|
| | Ink | Selenized film (from EDX – 20 keV) area 1 | Selenized film (from EDX – 7 keV) area 2 |
| $\frac{\text{Cu}}{\text{Zn} + \text{Sn}}$ | 0.82 ± 0.02 | 0.60 ± 0.07 | 0.86 ± 0.07 |
| $\frac{\text{Zn}}{\text{Sn}}$ | 1.20 ± 0.04 | 2.98 ± 0.04 | 0.96 ± 0.04 |

Table 4. 3 Elemental composition of the ink and of the sodium free absorber layer in the two areas highlighted in Figure 4. 2.

From high magnification top view SEM micrographs (Figure 4. 6), the CZTSe film appears composed of angular-shaped crystals with dimensions in the order of a few hundred nanometers and some bigger grains, resulting in an overall compact microstructure with some pinholes.

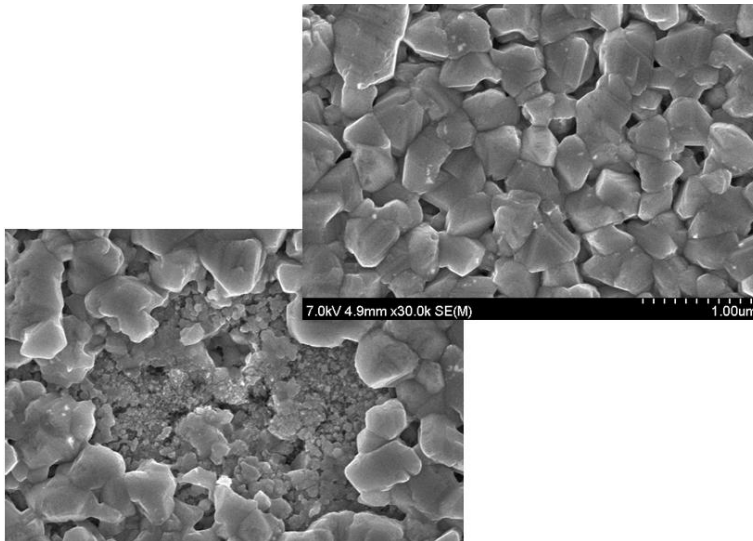


Figure 4. 6 Same magnification top-view SEM micrographs of the CZTSe layer.

The SEM cross section reported in Figure 4. 7 shows a double-layered film with a layer of small grains attached to the molybdenum selenide. Other groups reported a similar layer sandwiched between MoSe₂ and the absorber and attributed it to a carbon rich material [95, 96].

The mechanical removal of the bilayer was not feasible because it was solidly attached to the MoSe₂ which was itself very strongly bound to the metallic molybdenum, thus there was no chance to analyse the layer underneath the CZTSe by Raman spectroscopy or SEM. The overall film thickness measured with the profilometer was 1.1 μm .

The elemental analysis of the powder obtained by scratching the film deposited on a microscope slide revealed very low carbon and nitrogen contents (0.18 ± 0.05 and 0.54 ± 0.1 wt%), compared with their mass percentage in the ink (35.59% and 12.39% respectively), meaning that the decomposition of solvents and reagents occurred without leaving any significant contamination in the film.

According to this compositional analysis, we can estimate that there is one carbon atom for each five CZTSe unit cells. The same analysis was carried out previously on CIGS grown in reference [93], where C and N amounts were 0.07% and 0.15 wt%, values significantly lower than in these CZTSe samples, probably because of a more accurate design of the drying step after deposition.

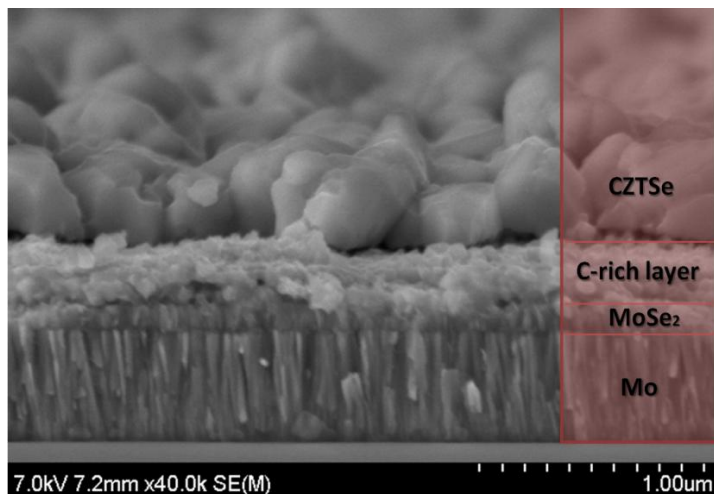


Figure 4. 7 SEM cross-section view of the CZTSe sample.

Raman spectra were collected at several locations of the film and they all resemble that reported in Figure 4. 8, implying a good degree of chemical homogeneity. Peaks at 198 cm^{-1} , 177 cm^{-1} and 236 cm^{-1} indicate that CZTSe is the main crystalline phase in the samples, but the presence of the ternary phase CTS cannot be excluded, as well as MoSe_2 , whose vibrational mode at around 245 (here 250 cm^{-1}) has been already observed for selenization times longer than 20 min [97].

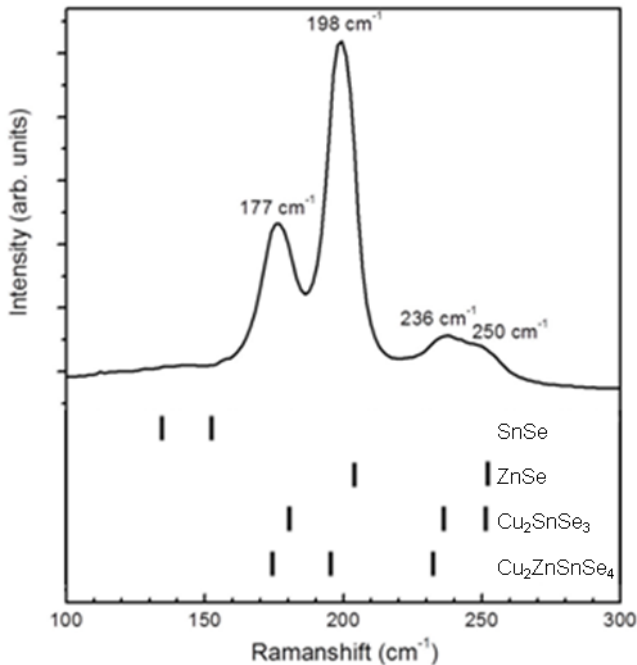


Figure 4. 8 Raman spectrum of a CZTSe layer. The estimated penetration depth is 350 nm.

Surface ZnSe was observed in the the SEM image of the absorber but cannot be seen in the Raman spectra since the 632.8 nm laser does not allow the detection of this secondary phase. To investigate on the presence of superficial ZnSe by Raman scattering, near-resonant conditions are required [98].

In Figure 4. 9 the XRD patterns of the absorber layer featuring the as-collected (a) and logarithmic intensities (b) are presented. The majority of signals belong to the $\text{Cu}_2\text{ZnSnSe}_4$ kesterite structure (PDF - 04-003-8817) (ICDD database). The diffraction peak corresponding to the (112) plane

located at 27.14° was fitted with a Gaussian, and its full-width at half-maximum (FWHM) is 0.30° (inset of Figure 4. 9a). This diffraction peak was used in the Scherrer equation to determine the mean crystallite size of the CZTSe phase, which was found to be 279 ± 4 nm. The value is consistent with sizes observed in the SEM micrographs.

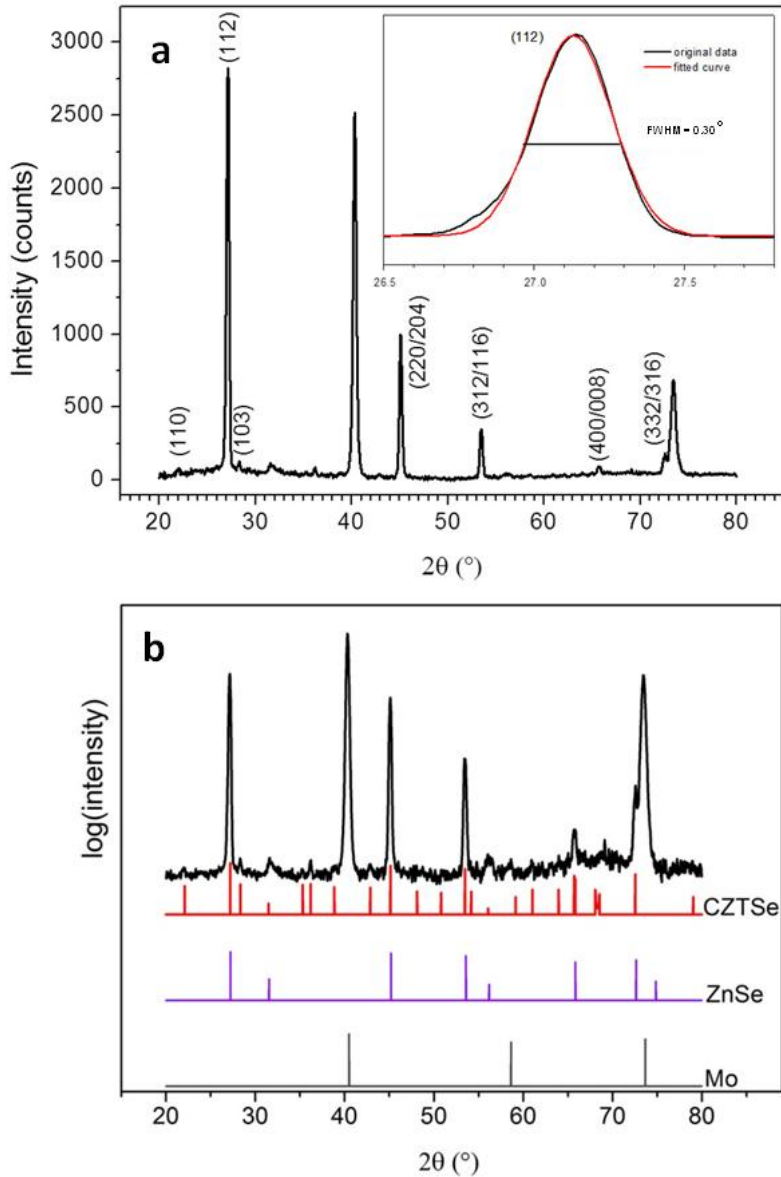


Figure 4. 9 XRD patterns of $\text{Cu}_2\text{ZnSnSe}_4$ thin films grown on molybdenum. (a) Diffracted intensities as collected and (Inset) Gaussian fitting of the (112) peak used in the Scherrer

equation to determine grain size, (b) Plot of the logarithm of intensities of the experimental data (black) and simulated patterns (colored) taken from the ICDD database [99].

From these measurements the presence of cubic ZnSe cannot be excluded, and signals coming from metallic molybdenum under the absorber layer are well visible. After the “LEM finalization” (see section 2.3) the solar cells were characterized by electrical measurements.

The highest efficiency achieved for a solar cell produced with the absorber layer described here is 2.39% (average is 1.96%) . Its current density-voltage characteristics is shown in Figure 4. 10a and the external quantum efficiency (EQE) is depicted in Figure 4. 10b. The low Fill Factor (FF) and open-circuit voltage (V_{oc}) are typical features of a highly defective material. It is difficult to ascertain whether the recombination centres are located at the interface of the material with the small-grain layer, or at the boundaries of CZTSe grains or in the bulk of the grains. Furthermore the best device exhibits only a small shunt resistance and a large series resistance. The J_{sc} was extracted from the J-V curve under illumination and from the integration of the EQE curve, giving respectively values of 31.2 mAcm^{-2} and 32.7 mAcm^{-2} , which match quite well with some much more efficient CZTSe cells reported in the literature [100, 101].

From the linear fit of the low energy part of the plot $[h\nu \cdot \ln(1-EQE)]^2$ against photon energy, the bandgap of CZTSe was extrapolated and found to be around 1.04 eV (Inset of Figure 4. 10b) which is indicative of an ordered kesterite structure, consistent with the slow cooling the samples underwent after the selenization step [102].

Recently, Colombara et al. showed that the shape and magnitude of the EQE is related to the number and size of ZnSe islands on the surface of the CZTSe absorber layer [103]. In this respect, the reasonably high overall quantum efficiency, especially in the region of ZnSe optical absorption, points to a low concentration of ZnSe on the surface, with presumably smaller size compared to the effective diffusion length of the minority carriers.

The low concentration of ZnSe is in line with the almost stoichiometric elemental composition measured by EDX.

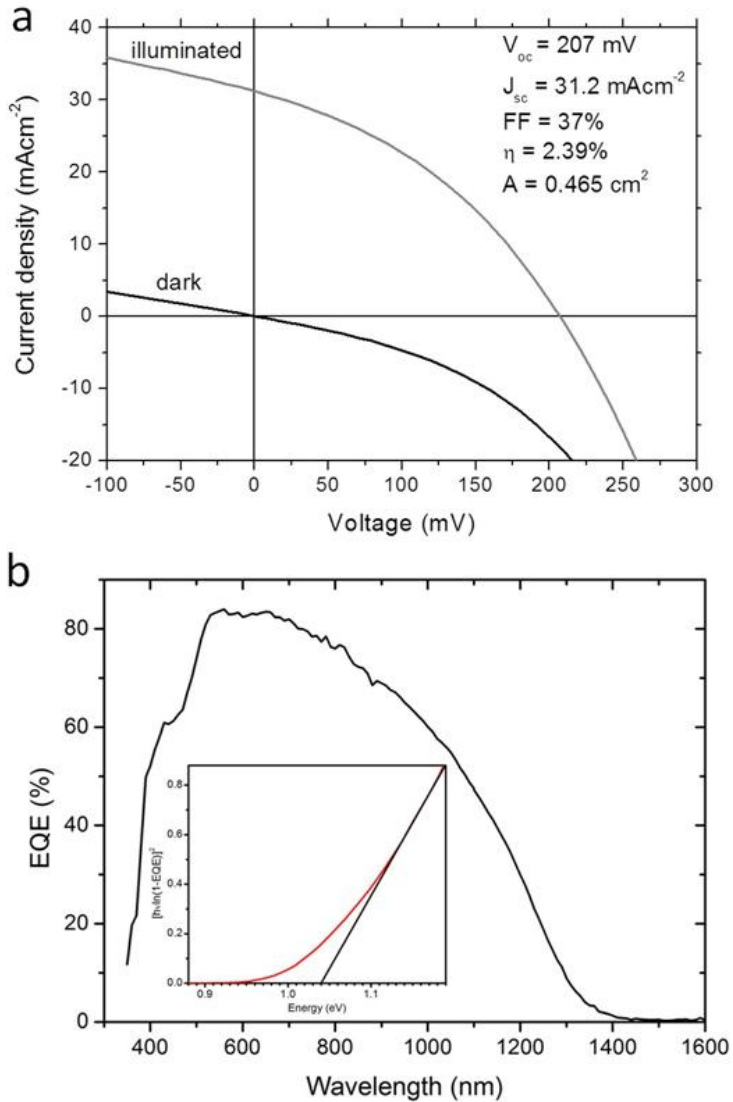


Figure 4. 10 (a) J-V curve and (b) corresponding EQE of the best solar cell. Inset shows the plot of $[\text{hv} \ln(1-\text{EQE})]^2$ against the photon energy, which gave an estimation of the optical bandgap (1.04 eV).

4. 4 Absorber layers grown by RTP

A precursor layer grown by depositing on glass the ink named “Na10ZnE” was divided into three pieces. After the treatment at 200 °C, each of them was put inside the chamber of a RTP and heated at three different temperatures together with 15 mg of SnSe and 100 mg of Se with 10 mbar of H₂/N₂ (10%). The diffractograms of the samples annealed in the RTP at 350 °C, 400 °C and 450 °C and the XRD pattern of a sample deposited on molybdenum and selenized through the standard annealing routine are stacked in Figure 4. 11.

At 350 °C the CZTSe is already forming, and all the signals belonging to this crystalline phase get more intense and sharper with temperature. Note that CZTSe shares the more intense reflections with the ternary phase Cu₂SnSe₃ (JCPDF 04-012-4693), thus at this stage it is very difficult to recognize one from another. Only when the crystals are fully grown one can notice substantial differences in the powder patterns by searching for minor reflections.

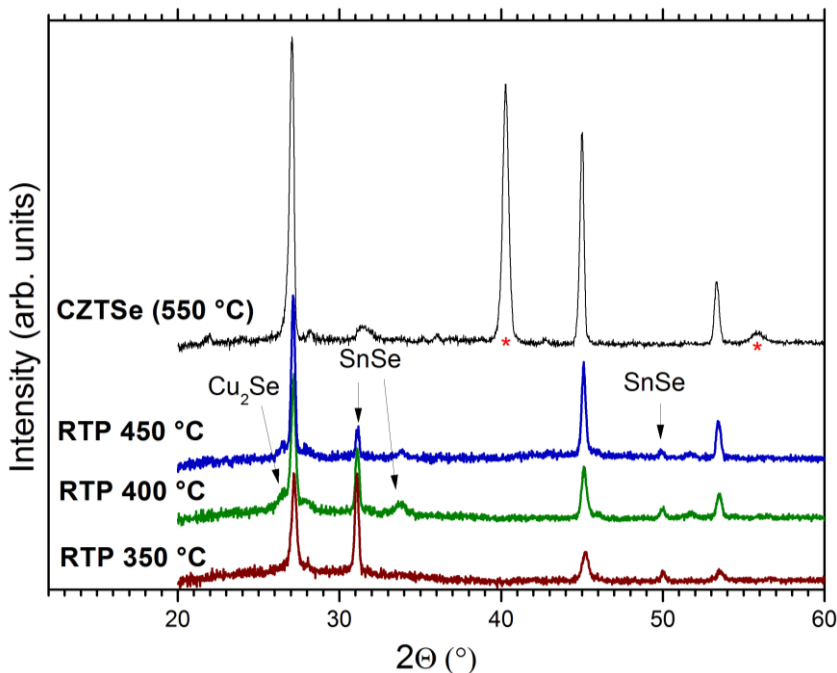


Figure 4. 11 (Colored) XRD patterns of the precursor layers Na10 grown on glass after treatment in the RTP at 350 °C, 400 °C and 450 °C in presence of SnSe and elemental Se. powders. (Black line) XRD pattern of CZTSe Na10 grown on Mo in a standard annealing setup. Asterisks indicate signals belonging to Mo.

Three reflections located at 31.05° , 33.75° and 49.90° are strong at 350°C and become weaker with temperature. They were found to belong to SnSe (JCPDS 04-009-2257), whose unreacted vapours might have condensed on the top of the samples during the rapid cooling of the sample. In fact, cooling in the RTP is much faster than the one usually occurring in an oven used for typical annealing. At around 26.4° , aside the main (112) reflection of CZTSe, a shoulder whose intensity is maximised at 400°C could be assigned to the Cu_2Se phase (JCPDS 00-47-1148). The signals highlighted with asterisks belong to the Mo layer underneath the absorber.

From the top SEM images of samples collected for samples treated at different temperatures in the RTP, one can recognize three different morphologies, corresponding to a compact “dark” bottom layer, some submicron sized crystals rising from its surface and some other big angular shaped grains set or lying on the surface (Figure 4. 12a, b and c).

EDX measurements of $50 \times 50 \mu\text{m}$ areas of the sample treated at 400°C in the RTP as the one depicted in Figure 4. 12d show that the elemental composition of the film traces out the one of the ink used, meaning that there is no depletion of any of the metal used, and the selenium amount reacted with the precursors is stoichiometric. The punctual EDX measurements focused on the three different regions for the sample annealed at 400°C showed that the bottom layer is copper-poor, as the crystals rising from it, while the big crystals are composed of copper and selenium only (see EDX spectrum in Figure 4. 12b)

These data, joined with the XRD results, suggest that by rapid thermal processing the temperature of 450°C is not high enough to promote the solid state reaction between copper selenide and the rest of the film. It was not possible to identify any other area, for instance rich in tin or zinc, by searching for differences in the microstructures, at least at the magnifications allowed by the EDX conditions.

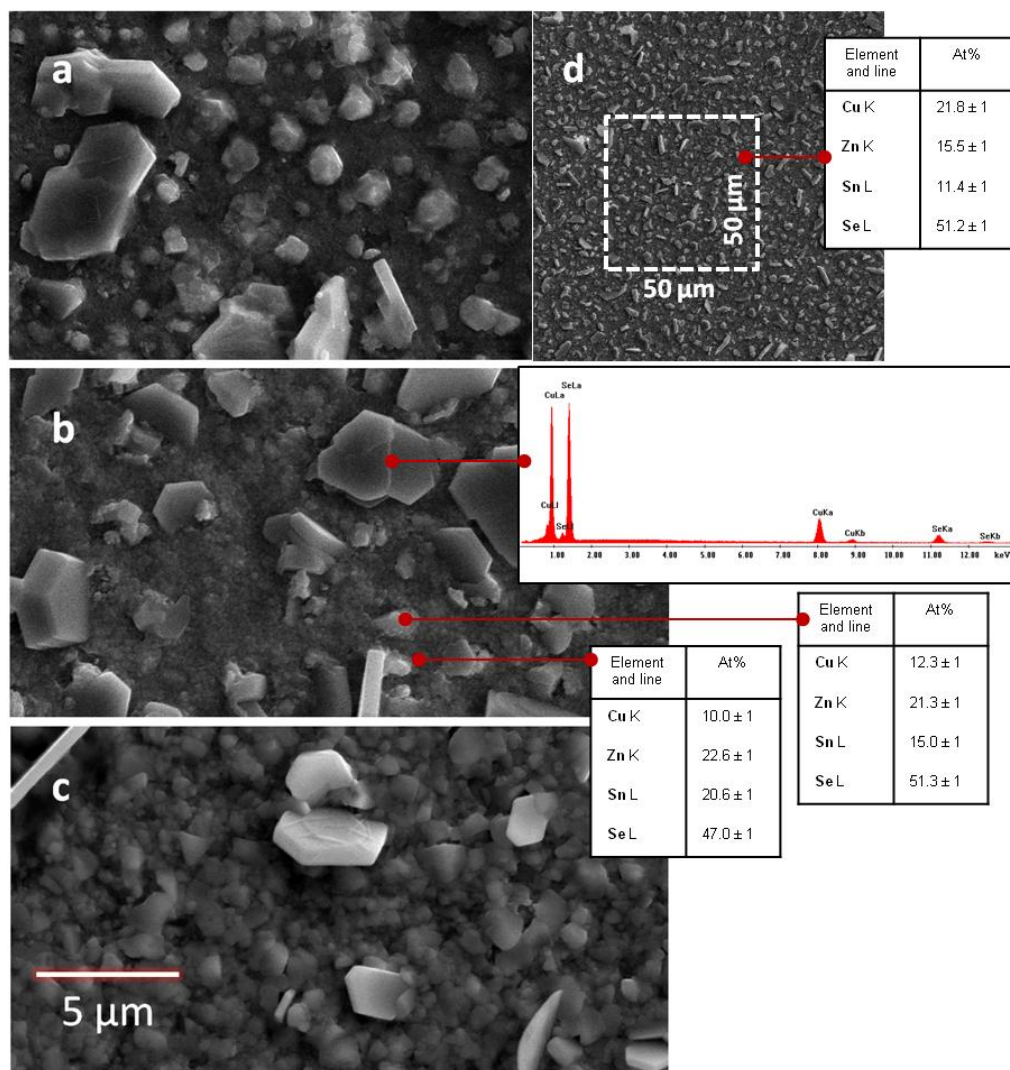


Figure 4. 12 SEM top-view micrographs of the precursor layers treated in the RTP at (a) 350 °C, (b) 400 °C and (c) 450 °C. (d) Lower magnification SEM top-view of the layer treated at 400 °C. The dotted square represent a sampled area analysed by EDX. Different point measurements were carried out on the areas highlighted with red dots and their composition as atomic percentages are listed beside the pictures.

4. 5 Characterization of sodium doped absorber layers and solar cells

From the SEM top view images (Figure 4. 13) it can be noticed that the layers produced with the addition of a sodium source are more compact: the samples CZTSe Na10 and Na10ZnE show a reduced number of voids if compared to the sodium free sample (CZTSe std) .

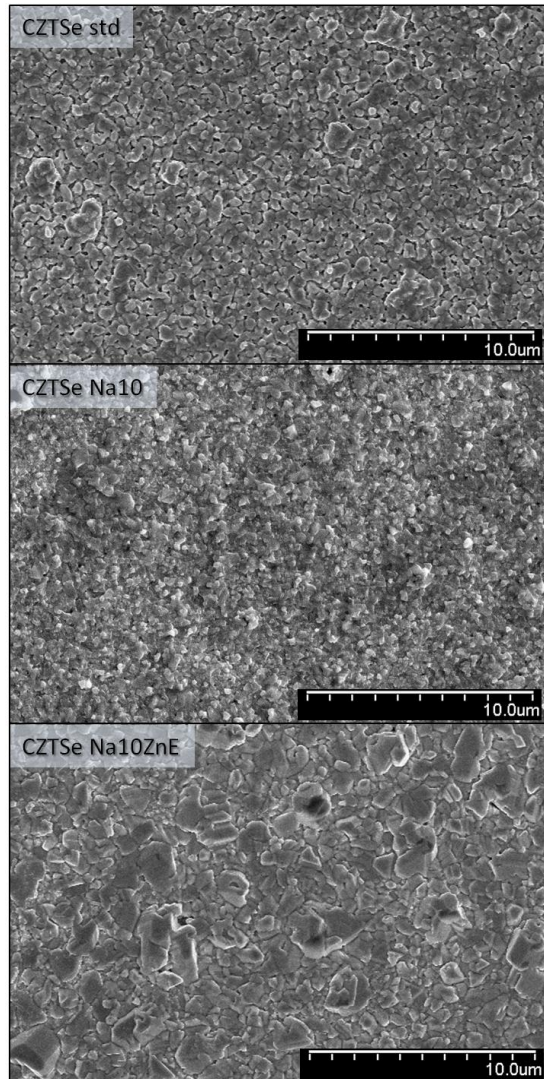


Figure 4. 13 Top-view SEM micrographs of CZTSe layers grown by using the inks: (top) Na-free, (middle) containing NaCl and (bottom) containing the same amount of NaCl and an excess of zinc source.

Almost the same compositions are detected by EDX measurements (see Table 4. 4). Once again, in sample CZTSe Na10, two areas are identified (Figure 4. 14): one zinc-rich and one zinc-poor, but the overall composition of a window with an area of 50x50 μm (square in Figure 4. 14) comprising the two of them results stoichiometric.

| | Elemental composition expressed as ratios of atomic percentages (from EDX on 50x50 μm – 20 keV) | |
|---|--|-----------------|
| | CZTSe Na10 | CZTSe Na10ZnE |
| $\frac{\text{Cu}}{\text{Zn} + \text{Sn}}$ | 0.82 ± 0.07 | 0.80 ± 0.07 |
| $\frac{\text{Zn}}{\text{Sn}}$ | 1.00 ± 0.04 | 0.98 ± 0.04 |

Table 4. 4 Average elemental compositions of CZTSe layers measured by EDX.

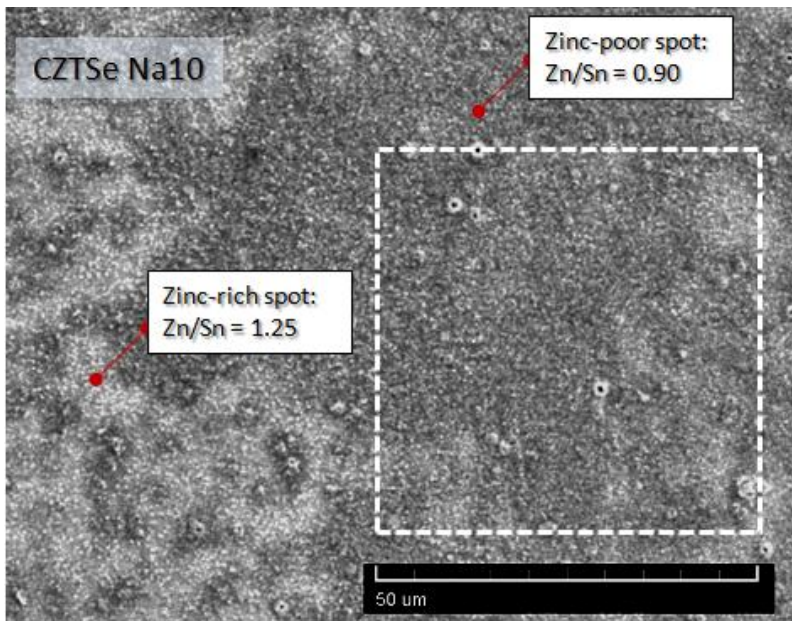


Figure 4. 14 Low magnification top-view SEM micrograph of the sample CZTSe Na10. Point EDX measurements on the dark spots revealed a zinc-poor composition, while the brighter spots were found to be copper-rich. EDX measurements on 50x50 μm areas like the one in the white frame have the average composition reported in Table 4. 4.

The microstructure of the samples CZTSe Na10ZnE is characterized by very big grains compared to the Na10, at least from what can be seen from the top-views. Moreover, in the samples CZTSe Na10ZnE the presence of zinc-rich “islands” is not detected at low magnifications, but ZnSe crystals are distributed on the surface of the absorber and can be identified very easily by looking at the cross-section (Figure 4. 15) of the films. Even though the ink Na10ZnE contained a higher amount of Zn formate, this excess was not detected by EDX measurement of the sampled areas of the selenized film. From the as-collected XRD patterns shown in Figure 4. 16, it can be noticed that the CZTSe Na10ZnE has the most intense reflections belonging to CZTSe (plus ZnSe) if compared with the respective Mo signals. This is probably because it is the thickest among the three.

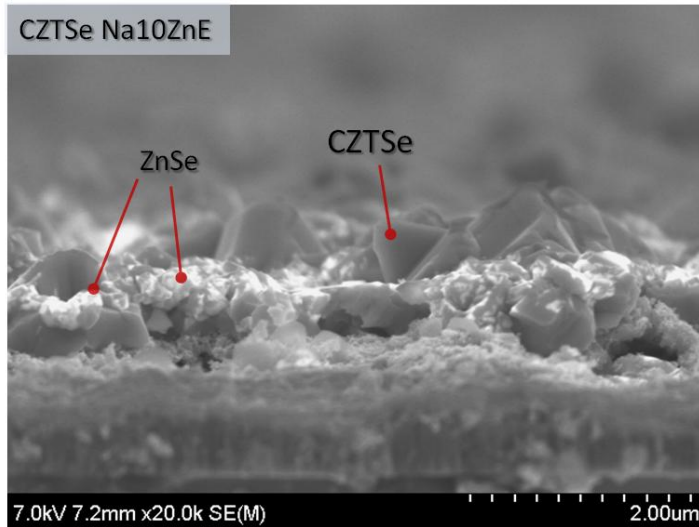


Figure 4. 15 Cross sectional view of the CZTSe Na10ZnE.

On the reverse, the signals belonging to CZTSe for the sample CZTSe Na10 are the weakest if compared with the respective Mo signals, therefore it must be the thinnest among the three. The presence of other layers between Mo and CZTSe prevents an accurate determination of the thickness of CZTSe layers (a prior normalization of as-collected XRD intensities by their thicknesses is required), thus it was not possible to make a proper comparison of the respective FWHM. Actually, as seen in SEM top view micrographs, the sample with more sodium doesn't look composed of bigger grains, but the material is more compact than the sodium free sample.

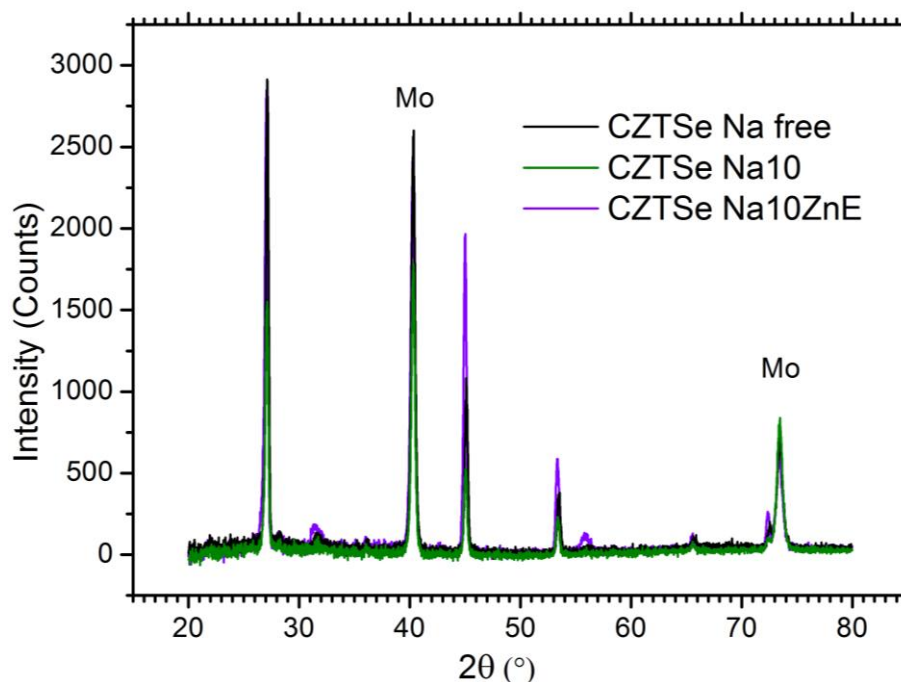


Figure 4. 16 As collected XRD patterns of the three CZTSe layers. All the signals not indicated as “Mo” can be assigned to CZTSe (JCPDS 04-003-8817) or ZnSe (00-037-1463).

The cross-sectional SEM micrographs of the CZTSe produced with the standard ink (Na free) and the sample produced by depositing the ink Na10ZnE, which contained both a sodium source and around 8% zinc formate more, show the same stack of layers, but with different morphologies and thicknesses, as reported in Figure 4. 17. For instance, the thickness of MoSe₂ is nearly double the thickness of MoSe₂ within the sample made with the standard ink.

Between the absorber and the MoSe₂, a carbon-rich layer is also present and its overall thickness is comparable with the carbon layer described in section 4. 2 but, at least from the spots analysed at the SEM, it looks less compact than the one observed previously on sodium free samples. The CZTSe Na10ZnE is also slightly thicker and more compact.

The higher thickness of the absorber may be due to a higher ratio of salts over the liquid components in the inks or the ratio of TMG over MeOH amount (see Table 4. 1): the ink Na10ZnE is more concentrated and viscous than the standard one. The reasons why the molybdenum underneath the

absorber CZTSe Na₁₀ZnE has undergone a deeper selenization is not clear since the annealing conditions were identical.

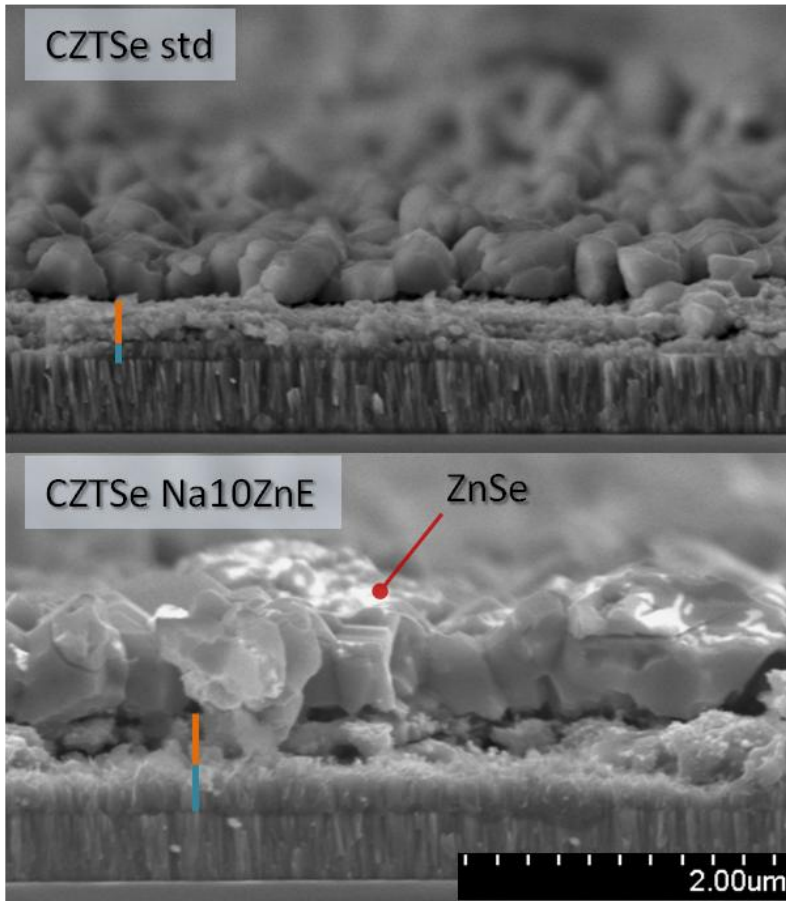


Figure 4. 17 SEM cross-section view of the samples CZTSe (sodium free) and CZTSe Na₁₀ZnE. The light blue and orange bars indicate MoSe₂ and carbon rich layer thicknesses, respectively.

Raman spectra of samples CZTSe Na₁₀ZnE show the same vibrational modes as for the sodium free sample, all belonging to CZTSe, but the signal at 250 cm⁻¹ this time is as intense as the peak at 237 cm⁻¹ and it doesn't appear as a shoulder (signals pointed by arrows in Figure 4. 18). We hypothesized previously for the sodium free sample that CTS might be present in the film since the peak at 250 cm⁻¹ could be assigned to one of its

vibrational modes, but the cross-sectional images suggest that this peak does not belong to CTS, but to MoSe_2 under the absorber.

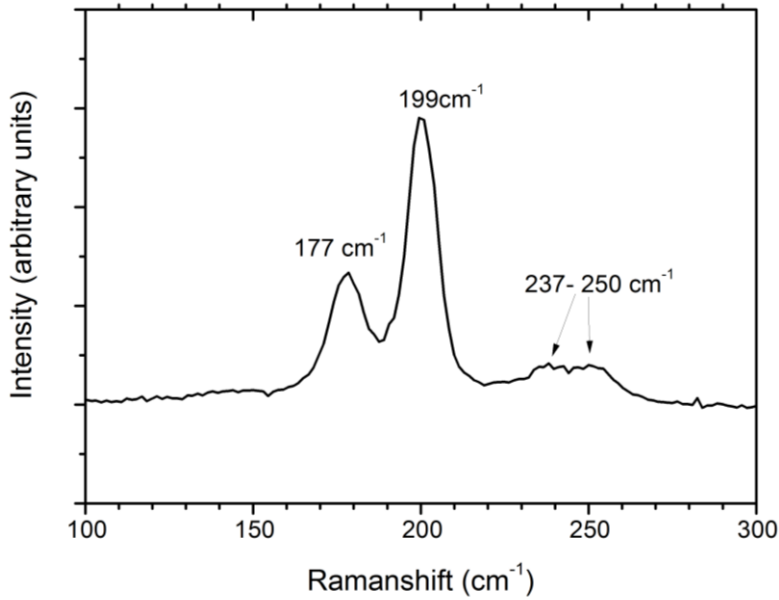


Figure 4. 18 Raman spectrum of a CZTSe Na10ZnE layer.

Unfortunately it was not possible to collect cross section SEM images of the same resolution for the sample CZTSe Na10. The picture in Figure 4. 19 shows that the layer is composed of grains as large and compact as sample CZTSe Na10ZnE, which is in accordance with the quantity of Na added to the ink, but it is not possible to identify layers underneath the absorber. However, the thickness of the layer deposited is evidently lower than the other two. The average thickness measured with the profilometer was around 650 nm.

Cells produced using the absorber grown with the addition of sodium with no further zinc supply showed an improved power conversion efficiency compared to the sodium free samples. The best within this batch is 3.17% efficient (average is 2.55%) . The J-V and EQE of this cell with an active area of 0.46 cm² are depicted in Figure 4. 20.

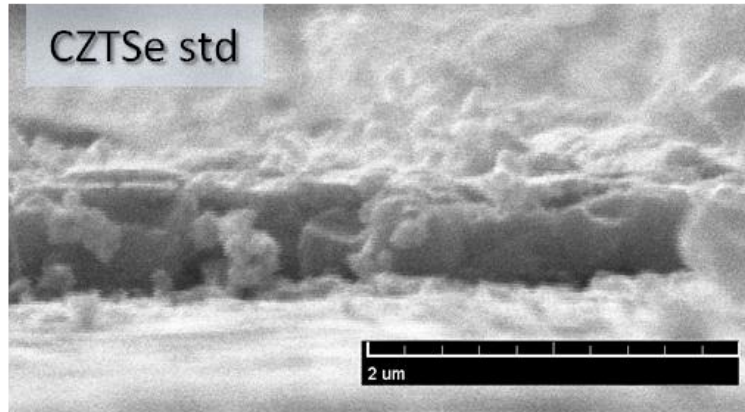


Figure 4. 19 SEM cross-section view of the samples CZTSe Na10.

The FF and the V_{oc} are respectively 3% and 53 mV higher than in the sodium free cells and the J_{sc} is 1.4 mAcm^{-2} lower, which is in accordance with a lower absorber thickness. Here the optical bandgap is again 1.04 eV. Therefore, an actual enhanced grain growth along with improved solar cells performance were observed for Na-doped CZTSe samples .

The cells produced with sample CZTSe Na10ZnE had efficiencies ranging from 0.20% to 0.93%. The J-V curve of the best cell is shown in Figure 4. 21. The presence of ZnSe, which has a demonstrated current-blocking effect because of its wide bandgap (2.7 eV), prevents the formation of a good ohmic contact with the CdS buffer layer and sensibly lowers the J_{sc} , the V_{oc} and FF. From the shape of the illuminated curve (black) one can predict that the series resistance is very high and the shunt resistance is lower than the ones in the two types of solar cells already shown. Direct evidence of J_{sc} reduction was already reported [104] as well as large degradation of V_{oc} and FF [105] owing to the presence of a ZnSe phase at the front of the absorber for CZTSe solar cells.

Also for the other two batches the Zn content in the liquid formulation was aimed to a Zn-rich composition ($Zn/Sn \approx 1.2$ in both inks), and some Zn-rich regions were clearly found too, but the resulting secondary phases were not as harmful as for this samples ($Zn/Sn \approx 1.2$ in the ink), where ZnSe grains are big enough to heavily affect the functioning of solar cells.

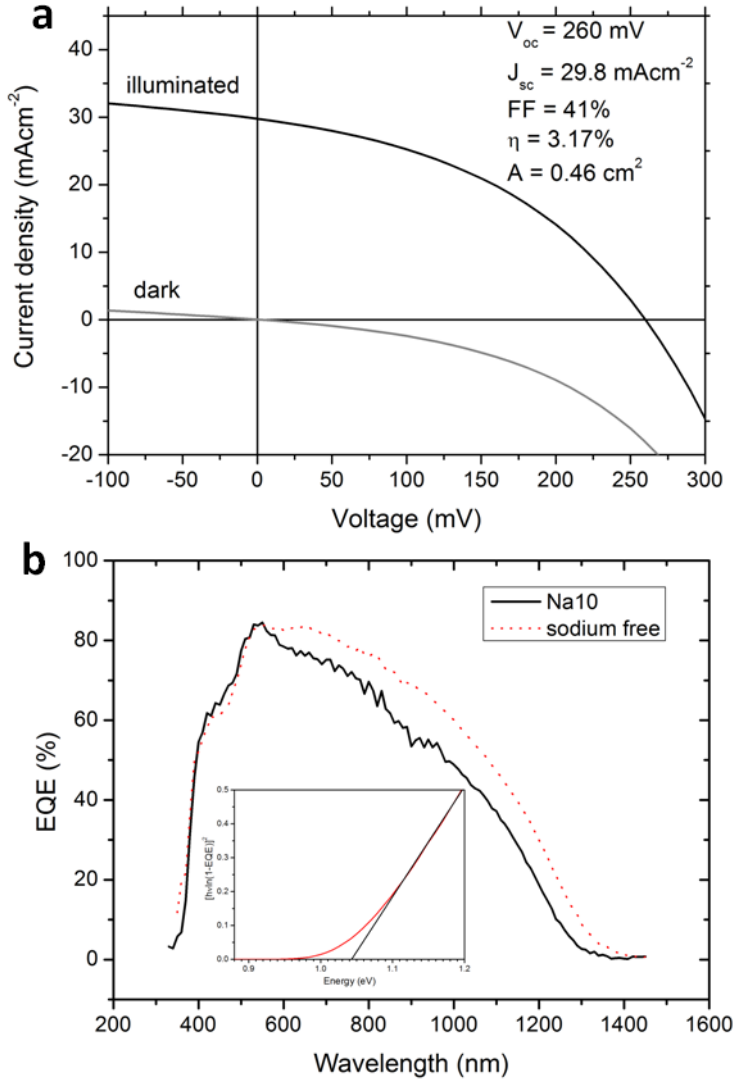


Figure 4. 20 (a) J-V curve and (b) corresponding EQE of the best solar cell in the batch of samples CZTSe Na10. The dotted red curve is the EQE of the Na free best CZTSe cell shown in section 4. 2. Inset shows the plot of $[\text{hv} \cdot \ln(1-\text{EQE})]^2$ against the photon energy, in order to have an estimation of the optical bandgap.

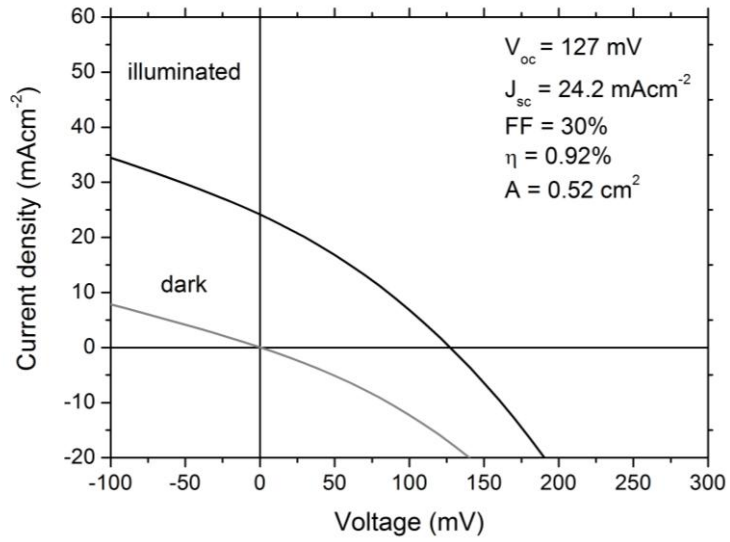


Figure 4. 21 J-V characteristics of the sample Na10ZnE.

Chapter 5

Conclusions and recommendations for further studies

In this thesis three new non-vacuum techniques to grow CZTS(e) via liquid formulations have been studied:

- 1) spin-coating of a viscous sol-gel followed by sulfurization;
- 2) drop-casting of a suspension composed of thiourea-metal complexes plus annealing at low temperature;
- 3) blade-coating of a viscous ink containing metal formates and TMG followed by selenization.

All three methods showed to be effective in the fabrication of polycrystalline CZTS(e) thin films on a laboratory scale. Raman measurements confirmed that the phase formation was accomplished with no detected spurious phases.

The first method allowed us to identify the main challenges that wet methods urge to overcome: the CZTS thin films featured a fragmented microstructure as reported in SEM micrographs. EDX analyses revealed that cracks occur in correspondence with the presence of chlorine atoms and a more detailed Raman investigation revealed intense broad signals assigned to amorphous carbon. Those features could prevent the use of layer for the fabrication of an efficient device. As a matter of fact, the best cell efficiency achieved based on the absorber produced by this method was 0.17%.

The motivation for the second method was manifold: design a fabrication technique that involved annealing steps at relatively low temperatures only, and develop a single liquid formulation that contained all the elemental sources. Both are desirable features that ease the scaling up of a new method. It was shown that CZTS can form at 450 °C, temperature that flexible substrates such as some polyimides (Kapton) can bear. Once again, cracks in the film were the main issue to deal with. We succeed in minimizing the dimension of those fractures by combining a new liquid formulation that included ethylene glycol and the design of an optimized annealing routine. Moreover, a preliminary study of the effects of polyvinyl alcohol on the film microstructure and composition was shown.

For what concerns these first two methods, contaminations often represented an open issue. Reagents other than Sn (II or IV) chloride have to be tested since chlorine has shown to have deleterious effects on the material compactness. Moreover, those processes were partially conducted in air. During both, the precursor layer formation and sulfurization process, the absorbers may have been contaminated with oxygen, thus it is highly recommended to investigate the influence of the oxygen presence in the films and possibly reproduce the fabrication technique in inert atmosphere.

Finally, the growth of polycrystalline CZTSe by means of the third method showed us an almost phase-pure film, characterized by good crystallinity and good reproducibility. A carbon-rich layer sandwiched between the absorber and the back contact didn't hamper the functioning of the solar cells. For the first time a quantification of carbon over CZTSe unit cells is presented. Solar cells with efficiencies of up to 2.39 % with V_{oc} of 207 mV, a J_{sc} of 31.2 mA/cm² and a fill factor of 37.1% were achieved for these copper-poor CZTSe absorbers.

The introduction of sodium to the absorber was accomplished by adding a NaCl solution into the liquid formulation. Na doped absorber

layers showed a much more compact structure compared to sodium free samples, and solar cells achieved an improved efficiency of 3.1 % and an increased V_{oc} of 207 mV.

The quality of the absorber and the solar cells performances obtained by this low cost method are promising and make the latter the best among the three processes studied in this thesis. Nonetheless, there is much room for improvement. For example, the selenization process can be optimized in order to minimize the thickness of $MoSe_x$ between the absorber and the Mo back contact. For what concerns C contamination, some pre-annealings could be carried out in order to vary the amount of carbon that remains trapped between the absorber and the back-contact and evaluate with more accuracy the carbon-rich layer effects on solar cells performance.

Moreover, the mechanism of incorporation of Zn inside the absorber deserves a deeper investigation if we aim at Zn-rich absorber layers.

Finally, the optimum quantity of Na inside the absorber still needs to be found.

By accomplishing these objectives, we believe that this wet process can really stand as a valuable alternative to vacuum-based methods for the wide production of kesterites-based solar cells.

Bibliography

- [1] Green, M. The path to 25% silicon solar cell efficiency: History of silicon cell evolution. *Progress in Photovoltaics: Research and Applications*, **17**, 183–189 (2009).
- [2] Cruz-Campa, J. L. *et al.* Microsystems enabled photovoltaics: 14.9% efficient 14 μ m thick crystalline silicon solar cell. *Solar Energy Materials and Solar Cells* **95**, 551–558 (2011).
- [3] Jeong, S., McGehee, M. D. & Cui, Y. All-back-contact ultra-thin silicon nanocone solar cells with 13.7% power conversion efficiency. *Nature Communications* **4**, 1-7 (2013).
- [4] Luque, A. & Hegedus, S. *Handbook of photovoltaic science and engineering* (Wiley, 2003).
- [5] Ferekides, C.S. High efficiency CSS CdTe solar cells. *Thin Solid Films* **361-362**, 520-526 (2000).
- [6] Green, M. A., Emery, K., Hishikawa, Y., Warta, W. & Dunlop, E. D. Solar cell efficiency tables (version 44): Solar cell efficiency tables. *Progress in Photovoltaics: Research and Applications* **22**, 701–710 (2014).
- [8] Jackson, P. *et al.* New world record efficiency for Cu(In,Ga)Se₂ thin-film solar cells beyond 20%. *Progress in Photovoltaics: Research and Applications* **19**, 894–897 (2011).
- [7] www.firstsolar.com
- [9] Niki, S. *et al.* CIGS absorbers and processes. *Progress in Photovoltaics: Research and Applications* **18**, 453–466 (2010).

- [10] Shafarman, W. N., Zhu, J. Effect of substrate temperature and deposition profile on evaporated Cu(InGa)Se₂ films and devices. *Thin Solid Films* **361-362**, 473-477, (2000).
- [11] <http://www.solar-frontier.com>
- [12] <http://www.thesolarclothcompany.com>
- [13] <http://www.globalsolar.com/>
- [14] Kaelin, M. *et al.* Low-cost CIGS solar cells by paste coating and selenization. *Thin Solid Films* **480-481**, 486–490 (2005).
- [15] Panthani, M. G. *et al.* Synthesis of CuInS₂, CuInSe₂, and CuIn_xGa(1-x)Se₂ (CIGS) Nanocrystal ‘Inks’ for Printable Photovoltaics. *Journal of the American Chemical Society* **130**, 16770–16777 (2008).
- [16] Singh, M., Jiu, J., Sugahara, T. & Sugauma, K. Thin-Film Copper Indium Gallium Selenide Solar Cell Based on Low-Temperature All-Printing Process. *ACS Applied Materials & Interfaces* **6**, 16297–16303 (2014).
- [17] Repins, I. *et al.* Kesterites and chalcopyrites: a comparison of close cousins. in *MRS Proceedings* **1324**, mrs11–1324 (Cambridge Univ Press, 2011).
- [18] Element abundances from <http://periodictable.com/Properties/A/CrustAbundance.html>.
- [19] For all elements except sulfur the price was calculated by averaging prices published in <http://www.metal-pages.com/> and <http://www.metalprices.com/> update to the 31st of January 2015 . Sulfur average price in January 2015 published by Sunsirs <http://www.sunsirs.com/uk/prodetail-427.html>.
- [20] Chen, S. *et al.* Intrinsic point defects and complexes in the quaternary kesterite semiconductor Cu₂ZnSnS₄. In: *Phys. Rev.* **B 81**, 24, 245204 (2010).

- [21] Friedlmeier, T. M. et al Proceedings of the 14th European Photovoltaic Specialists Conference, Barcelona, 30 June–4 July, 1242 (1997).
- [22] Seol, J.S. et al. Electrical and optical properties of $\text{Cu}_2\text{ZnSnS}_4$ thin films prepared by rf magnetron sputtering process *Sol. Energy Mater.Sol. Cells* **75**, 155-162 (2003).
- [23] Rey, G. et al. The band gap of $\text{Cu}_2\text{ZnSnS}_4$: Effect of order-disorder. *Applied Physics Letters* **105**, 112106 (2014).
- [24] Malerba, C. et al. CZTS stoichiometry effects on the band gap energy. *Journal of Alloys and Compounds* **582**, 528–534 (2014).
- [25] Sarswat, P. K. & Free, M. L. A study of energy band gap versus temperature for $\text{Cu}_2\text{ZnSnS}_4$ thin films. *Physica B: Condensed Matter* **407**, 108–111 (2012).
- [26] Haight, R. et al. Band alignment at the $\text{Cu}_2\text{ZnSn}(\text{S}_x\text{Se}_{1-x})_4/\text{CdS}$ interface. *Applied Physics Letters* **98**, 253502 (2011).
- [27] Ahn, S. et al. Determination of band gap energy (E_g) of $\text{Cu}_2\text{ZnSnSe}_4$ thin films: On the discrepancies of reported band gap values. *Applied Physics Letters* **97**, 021905 (2010).
- [28] Schorr, S. The crystal structure of kesterite type compounds: A neutron and X-ray diffraction study. *Solar Energy Materials and Solar Cells* **95**, 1482–1488 (2011).
- [29] Paier, J., Asahi, R., Nagoya, A. & Kresse, G. $\text{Cu}_2\text{ZnSnS}_4$ as a potential photovoltaic material: A hybrid Hartree-Fock density functional theory study. *Physical Review B* **79**, (2009).
- [30] Persson, C. Electronic and optical properties of $\text{Cu}_2\text{ZnSnS}_4$ and $\text{Cu}_2\text{ZnSnSe}_4$. *Journal of Applied Physics* **107**, 053710 (2010).
- [31] Hall, S. R. Et al. Kesterite $\text{Cu}_2(\text{Zn,Fe})\text{SnS}_4$ and stannite $\text{Cu}_2(\text{Fe, Zn})\text{SnS}_4$ structurally similar but distinct minerals. *Canadian Mineralogist*, **16**, 131-137 (1978).

- [32] Matsushita, H., Maeda, T., Katsui, A. & Takizawa, T. Thermal analysis and synthesis from the melts of Cu-based quaternary compounds Cu–III–IV–VI₄ and Cu₂–II–IV–VI₄ (II= Zn, Cd; III= Ga, In; IV= Ge, Sn; VI= Se). *Journal of Crystal Growth* **208**, 416–422 (2000).
- [33] Dale, P. J., Peter, L. M., Loken, A. & Scragg, J. Towards Sustainable Photovoltaic Solar Energy Conversion: Studies Of New Absorber Materials. *ECS Transactions*, **19** (3), 179-187 (2009).
- [34] Olekseyuk, I. D., Dudchak, I. V. & Piskach, L. V. Phase equilibria in the Cu₂S–ZnS–SnS₂ system. *Journal of Alloys and Compounds* **368**, 135–143 (2004).
- [35] Scragg, J. J.: *Studies of Cu₂ZnSnS₄ films prepared by sulphurisation of electrodeposited precursors*, University of Bath, Dissertation (2010).
- [36] Washio, T. *et al.* 6% Efficiency Cu₂ZnSnS₄-based thin film solar cells using oxide precursors by open atmosphere type CVD. *Journal of Materials Chemistry* **22**, 4021 (2012).
- [37] Wagner, R. ; Wiemhöfer, H. D.: Hall effect and conductivity in thin films of low temperature chalcocite Cu₂S at 20 °C as a function of stoichiometry. *Journal of Physics and Chemistry of Solids* **44**, 801–805 (1983).
- [38] Nozaki, H. ; Shibata, K. ; Ohhashi, N. Metallic hole conduction in CuS. *Journal of Solid State Chemistry* **91**, 306–311 (1991).
- [39] Berg, D. Kesterite equilibrium reaction and the discrimination of secondary phases from Cu₂ZnSnS₄, University of Luxembourg, Dissertation (2012).
- [40] Vora, N. *et al.* Phase identification and control of thin films deposited by co-evaporation of elemental Cu, Zn, Sn, and Se. *Journal of Vacuum Science & Technology A* **30**, 051201 (2012).
- [41] W. Ahmed M.Y. Nadeem, Optical properties of ZnS thin films, *Turkish Journal of Physics* **24**, 651-659 (2000).

- [42] Marchionna, S. *et al.* Cu₂ZnSnS₄ solar cells grown by sulphurisation of sputtered metal precursors. *Thin Solid Films* **542**, 114–118 (2013).
- [43] López-Marino, S. *et al.* ZnSe Etching of Zn-Rich Cu₂ZnSnSe₄: An Oxidation Route for Improved Solar-Cell Efficiency. *Chemistry - A European Journal* **19**, 14814–14822 (2013).
- [44] Fairbrother, A. *et al.* ZnS grain size effects on near-resonant Raman scattering: optical non-destructive grain size estimation. *CrystEngComm* **16**, 4120 (2014).
- [45] Redinger, A. *et al.* Detection of a ZnSe secondary phase in coevaporated Cu₂ZnSnSe₄ thin films. *Applied Physics Letters* **98**, 101907 (2011).
- [46] Wu, Z. *et al.*, Hexagonal Cu₂SnS₃ with metallic character: Another category of conducting sulfides, *Applied Physics Letters* **91**, 143104 (2007).
- [47] Fischereder, A. *et al.* Investigation of Cu₂ZnSnS₄ Formation from Metal Salts and Thioacetamide. *Chemistry of Materials* **22**, 3399–3406 (2010).
- [48] Kumar, Y. B. K., Babu, G. S., Bhaskar, P. U. & Raja, V. S. Effect of starting-solution pH on the growth of Cu₂ZnSnS₄ thin films deposited by spray pyrolysis. *physica status solidi (a)* **206**, 1525–1530 (2009).
- [49] Tanaka, T. *et al.* Influence of composition ratio on properties of Cu₂ZnSnS₄ thin films fabricated by co-evaporation. *Thin Solid Films* **518**, S29–S33 (2010).
- [50] Scragg, J. J., Berg, D. M. & Dale, P. J. A 3.2% efficient Kesterite device from electrodeposited stacked elemental layers. *Journal of Electroanalytical Chemistry* **646**, 52–59 (2010).
- [51] Katagiri, H., *et al.* Preparation and evaluation of Cu₂ZnSnS₄ thin films by sulfurization of E-B evaporated precursors. *Solar Energy Materials and Solar Cells* **49**, 407–414 (1997).

- [52] Zoppi, G. *et al.* Cu₂ZnSnSe₄ thin film solar cells produced by selenisation of magnetron sputtered precursors. *Progress in Photovoltaics: Research and Applications* **17**, 315–319 (2009).
- [53] Moholkar, A.V. Development of CZTS thin films solar cells by pulsed laser deposition: Influence of pulse repetition rate. *Solar Energy* **85**, 1354-1363 (2011).
- [54] Chen, G. *et al.* Low cost preparation of Cu₂ZnSnS₄ and Cu₂ZnSn(S_xSe_{1-x})₄ from binary sulfide nanoparticles for solar cell application. *Journal of Power Sources* **262**, 201–206 (2014).
- [55] Shin, B. *et al.* Thin film solar cell with 8.4% power conversion efficiency using an earth-abundant Cu₂ZnSnS₄ absorber: Cu₂ZnSnS₄ solar cell with 8.4% efficiency. *Progress in Photovoltaics: Research and Applications* **21**, 72–76 (2013).
- [56] Brammertz, G. *et al.* Characterization of defects in 9.7% efficient Cu₂ZnSnSe₄-CdS-ZnO solar cells. *Applied Physics Letters* **103**, 163904 (2013).
- [57] Repins, I. *et al.* Co-evaporated Cu₂ZnSnSe₄ films and devices. *Solar Energy Materials and Solar Cells* **101**, 154–159 (2012).
- [58] Wang, W. *et al.* Device Characteristics of CZTSSe Thin-Film Solar Cells with 12.6% Efficiency. *Advanced Energy Materials* **4**, 1301465 (2014).
- [59] Kim, J. *et al.* High Efficiency Cu₂ZnSn(S,Se)₄ Solar Cells by applying a Double In₂S₃/CdS Emitter. *Advanced Materials* **26**, 7427–7431(2014).
- [60] Yuan, M. & Mitzi, D. B. Solvent properties of hydrazine in the preparation of metal chalcogenide bulk materials and films. *Dalton Transactions* **31**, 6065-6263 (2009).
- [61] Nakada, T. *et al.* Effects of Sodium on Cu(In,Ga)Se₂-Based Thin Films and Solar Cells. *Jpn. J. Appl. Phys.*, **36**, 732-737 (1997).

- [62] Gershon, T. *et al.* The Role of Sodium as a Surfactant and Suppressor of Non-Radiative Recombination at Internal Surfaces in $\text{Cu}_2\text{ZnSnS}_4$. *Advanced Energy Materials* **5**, 1400849 (2015).
- [63] Jackson, P., Hariskos, D., Wuerz, R., Wischmann, W. & Powalla, M. Compositional investigation of potassium doped $\text{Cu}(\text{In,Ga})\text{Se}_2$ solar cells with efficiencies up to 20.8% *physica status solidi (RRL) - Rapid Research Letters* **8**, 219–222 (2014).
- [64] Tong, Z. *et al.* Effects of potassium doping on solution processed kesterite $\text{Cu}_2\text{ZnSnS}_4$ thin film solar cells. *Applied Physics Letters* **105**, 223903 (2014).
- [65] Prabhakar, T. & Jampana, N. Effect of sodium diffusion on the structural and electrical properties of $\text{Cu}_2\text{ZnSnS}_4$ thin films. *Solar Energy Materials and Solar Cells* **95**, 1001–1004 (2011).
- [66] Schaltegger, S. & Synnestvedt, T. The link between ‘green’ and economic success: environmental management as the crucial trigger between environmental and economic performance. *Journal of environmental management* **65**, 339–346 (2002).
- [67] Sutter-Fella, C. M. *et al.* Sodium Assisted Sintering of Chalcogenides and Its Application to Solution Processed $\text{Cu}_2\text{ZnSn}(\text{S,Se})_4$ Thin Film Solar Cells. *Chemistry of Materials* **26**, 1420–1425 (2014).
- [68] Li, J. V., Kuciauskas, D., Young, M. R. & Repins, I. L. Effects of sodium incorporation in Co-evaporated $\text{Cu}_2\text{ZnSnSe}_4$ thin-film solar cells. *Applied Physics Letters* **102**, 163905 (2013);
- Li, J. V., Kuciauskas, D., Young, M. R. & Repins, I. L. Erratum: ‘Effects of sodium incorporation in Co-evaporated $\text{Cu}_2\text{ZnSnSe}_4$ thin-film solar cells’ [Appl. Phys. Lett. 102, 163905 (2013)]. *Applied Physics Letters* **103**, 029901 (2013).
- [69] Hlaing Oo, W. M. *et al.* Grain Size and Texture of $\text{Cu}_2\text{ZnSnS}_4$ Thin Films Synthesized by Cosputtering Binary Sulfides and Annealing: Effects of Processing Conditions and Sodium. *Journal of Electronic Materials* **40**, 2214–2221 (2011).

- [70] Werner, M., Sutter-Fella, C. M., Hagedorfer, H., Romanyuk, Y. E. & Tiwari, A. N. $\text{Cu}_2\text{ZnSn}(\text{S},\text{Se})_4$ solar cell absorbers processed from Na-containing solutions in DMSO: $\text{Cu}_2\text{ZnSn}(\text{S},\text{Se})_4$ solar cell absorbers. *physica status solidi (a)* **212**, 116–120 (2015).
- [71] Bornside, D. E., Macosko, C. W. & Scriven, L. E. Spin coating: One-dimensional model. *Journal of Applied Physics* **66**, 5185 (1989).
- [72] Grosso, D. How to exploit the full potential of the dip-coating process to better control film formation. *Journal of Materials Chemistry* **21**, 17033 (2011).
- [73] Maeda, K., Tanaka, K., Nakano, Y. & Uchiki, H. Annealing Temperature Dependence of Properties of $\text{Cu}_2\text{ZnSnS}_4$ Thin Films Prepared by Sol–Gel Sulfurization Method. *Japanese Journal of Applied Physics* **50**, 05FB08 (2011).
- [74] Cheng, A.-J. *et al.* Imaging and phase identification of $\text{Cu}_2\text{ZnSnS}_4$ thin films using confocal Raman spectroscopy. *Journal of Vacuum Science & Technology A* **29**, 051203 (2011).
- [75] Zou, Y. *et al.* Carbon-free $\text{Cu}_2\text{ZnSn}(\text{S},\text{Se})_4$ film prepared via a non-hydrazine route. *Science China Chemistry* 1–7 (2014).
- [76] Lee, H. J. *et al.* Inductively Coupled Plasma Etching of Chemical-Vapor-Deposited Amorphous Carbon in $\text{N}_2/\text{O}_2/\text{Ar}$ Chemistries. *Jpn. J. Appl. Phys.* **48**, 08HD05 (2009).
- [77] Doona, C. J. & Stanbury, D. M. Equilibrium and Redox Kinetics of Copper(II)–Thiourea Complexes. *Inorg. Chem.* **35**, 3210–3216 (1996).
- [78] Timchenko, V. P., Novozhilov, A. L. & Slepysheva, O. A. Kinetics of thermal decomposition of thiourea. *Russian journal of general chemistry* **74**, 1046–1050 (2004).
- [79] Schurr, R. *et al.* The crystallisation of $\text{Cu}_2\text{ZnSnS}_4$ thin film solar cell absorbers from co-electroplated Cu–Zn–Sn precursors. *Thin Solid Films* **517**, 2465–2468 (2009).

- [80] Chaudhuri, T. K. & Tiwari, D. Earth-abundant non-toxic $\text{Cu}_2\text{ZnSnS}_4$ thin films by direct liquid coating from metal–thiourea precursor solution. *Solar Energy Materials and Solar Cells* **101**, 46–50 (2012).
- [81] Chernomordik, B. D. *et al.* Rapid facile synthesis of $\text{Cu}_2\text{ZnSnS}_4$ nanocrystals. *Journal of Materials Chemistry A* **2**, 10389 (2014).
- [82] Sun, Y. *et al.* Ethylene glycol-based dip coating route for the synthesis of $\text{Cu}_2\text{ZnSnS}_4$ thin film. *Materials Letters* **92**, 195–197 (2013).
- [83] Fernandes, P. A., Salomé, P. M. P. & da Cunha, A. F. $\text{Cu}_x\text{SnS}_{(x+1)}$ ($x = 2, 3$) thin films grown by sulfurization of metallic precursors deposited by dc magnetron sputtering. *physica status solidi C* **7**, 901–904 (2010).
- [84] Dimitrievska, M. *et al.* Multiwavelength excitation Raman scattering study of polycrystalline kesterite $\text{Cu}_2\text{ZnSnS}_4$ thin films. *Applied Physics Letters* **104**, 021901 (2014).
- [85] Khare, A., Himmetoglu, B., Cococcioni, M. & Aydil, E. S. First principles calculation of the electronic properties and lattice dynamics of $\text{Cu}_2\text{ZnSn}(\text{S}_{1-x}\text{Se}_x)_4$. *Journal of Applied Physics* **111**, 123704 (2012).
- [86] Lin, Z., Han, D. & Li, S. Study on thermal decomposition of copper (II) acetate monohydrate in air. *J Therm Anal Calorim* **107**, 471–475 (2011).
- [87] Bann, B. & Miller, S. A. Melamine And Derivatives Of Melamine. *Chem. Rev.* **58**, 131–172 (1958).
- [88] Hosmane, R. S., Rossman, M. A. & Leonard, N. J. Synthesis and structure of tri-s-triazine. *J. Am. Chem. Soc.* **104**, 5497–5499 (1982).
- [89] Seo, D. & Lim, S. Effect of sulfur and copper amounts in sol–gel precursor solution on the growth, crystal properties, and optical

properties of $\text{Cu}_2\text{ZnSnS}_4$ films. *Journal of Materials Science: Materials in Electronics* **24**, 3756–3763 (2013).

[90] Yeryukov, N. A. *et al.* Synthesis and Characterization of Cu_xS ($x = 1-2$) Nanocrystals Formed by the Langmuir–Blodgett Technique. *The Journal of Physical Chemistry C* **118**, 23409–23414 (2014).

[91] Utyuzh, A. N., Timofeev, Y. A. & Stepanov, G. N. Effect of pressure on Raman spectra of SnS_2 single crystals. *Physics of the Solid State* **52**, 352–356 (2010).

[92] Brauer, G. *Handbook of Preparative Inorganic Chemistry*, II Edition, Elsevier, 2012.

[93] Berner, U. & Widenmeyer, M. Solution-based processing of $\text{Cu}(\text{In,Ga})\text{Se}_2$ absorber layers for 11% efficiency solar cells via a metallic intermediate: Solution-based processing of CIGS absorber layers. *Progress in Photovoltaics: Research and Applications* (2014). doi:10.1002/pip.2546

[94] Tanaka, K., Fukui, Y., Moritake, N. & Uchiki, H. Chemical composition dependence of morphological and optical properties of $\text{Cu}_2\text{ZnSnS}_4$ thin films deposited by sol–gel sulfurization and $\text{Cu}_2\text{ZnSnS}_4$ thin film solar cell efficiency. *Solar Energy Materials and Solar Cells* **95**, 838–842 (2011).

[95] Cao, Y. *et al.* High-Efficiency Solution-Processed $\text{Cu}_2\text{ZnSn}(\text{S,Se})_4$ Thin-Film Solar Cells Prepared from Binary and Ternary Nanoparticles. *Journal of the American Chemical Society* **134**, 15644–15647 (2012).

[96] Ilari, G. M. *et al.* solar cell absorbers spin-coated from amine-containing ether solutions. *Solar Energy Materials and Solar Cells* **104**, 125–130 (2012).

[97] He, J. *et al.* Effect of selenization time on the growth of $\text{Cu}_2\text{ZnSnS}_4$ thin films obtained from rapid thermal processing of stacked metallic layers. *Materials Letters* **126**, 1–4 (2014).

[98] Djemour, R. *et al.* Detecting ZnSe secondary phase in $\text{Cu}_2\text{ZnSnSe}_4$ by room temperature photoluminescence. *Applied*

Physics Letters **102**, 222108 (2013).

[99] JCPDF cards from the International Centre for Diffraction Data (ICDD): Cu₂ZnSnSe₄ 04-003-8817, ZnSe 00-037-1463, MoSe₂ 04-003-6623, Mo 00-042-1120

[100] Repins, I. *et al.* Co-evaporated Cu₂ZnSnSe₄ films and devices. *Solar Energy Materials and Solar Cells* **101**, 154–159 (2012).

[101] Shin, B., Zhu, Y., Bojarczuk, N. A., Jay Chey, S. & Guha, S. Control of an interfacial MoSe₂ layer in Cu₂ZnSnSe₄ thin film solar cells: 8.9% power conversion efficiency with a TiN diffusion barrier. *Applied Physics Letters* **101**, 053903 (2012).

[102] Rey, G. *et al.* The band gap of Cu₂ZnSnSe₄: Effect of order-disorder. *Applied Physics Letters* **105**, 112106 (2014).

[103] Colombara, D. *et al.* Quantification of surface ZnSe in Cu₂ZnSnSe₄-based solar cells by analysis of the spectral response. *Solar Energy Materials and Solar Cells* **123**, 220–227 (2014).

[104] Timo Wätjen, J., Engman, J., Edoff, M. & Platzer-Björkman, C. Direct evidence of current blocking by ZnSe in Cu₂ZnSnSe₄ solar cells. *Applied Physics Letters* **100**, 173510 (2012).

[105] Hsu, W.-C. *et al.* The effect of Zn excess on kesterite solar cells. *Solar Energy Materials and Solar Cells* **113**, 160–164 (2013).

Publications & presentations

S. Marchionna, P. Garattini, A. Le Donne, M. Acciarri, S. Tombolato, S. Binetti, “Cu₂ZnSnS₄ solar cells grown by sulphurisation of sputtered metal precursors”, *Thin Solid Films* **542**, 114 (2013).

A. Le Donne, A. Scaccabarozzi, S. Tombolato, S. Binetti, M. Acciarri, A. Abbotto, “Solar Photovoltaics: A Review”, *Reviews in Advanced Sciences and Engineering* **2**, 1(2013) .

A. Le Donne, A. Scaccabarozzi, S. Tombolato, S. Marchionna, P. Garattini, B. Vodopivec, M. Acciarri, and S. Binetti, “State of the Art and Perspectives of Inorganic Photovoltaics” *ISRN Renewable Energy Volume 2013*, Article ID 830731.

S. Tombolato, A. Colombo, M. Acciarri, M. Boshta, S. Binetti “Cu₂ZnSnS₄ Thin Film Solar Cells Produced by Thiourea Complexes Suspension” *Proceedings of 29th European Photovoltaic Solar Energy Conference and Exhibition EUPVSEC 2014* pag.1829-1931 ISBN 3-936338-34-5.

S. Tombolato, U. Berner, D. Colombara, S. Binetti, and P. J. Dale “Cu₂ZnSnSe₄ device obtained by a new wet process for metallic precursor layer fabrication “ *Solar Energy* (under review).

18th to 28th July 2012 - 56th Course of the International School of Solid State Physics “Materials for Renewable Energy” at the "Ettore Majorana Foundation and Centre for Scientific Culture“ – POSTER PRESENTATION

22-24th May 2013 - Photovoltaic Technical Conference in Aix En Provence France – FLASH TALK and POSTER PRESENTATION
